



HAL
open science

Opening-gap plasmonic antennas : a surface plasmon polariton source

Cam Nhung Vu

► **To cite this version:**

Cam Nhung Vu. Opening-gap plasmonic antennas : a surface plasmon polariton source. Physics [physics]. Université Claude Bernard - Lyon I, 2022. English. NNT : 2022LYO10089 . tel-04165692

HAL Id: tel-04165692

<https://theses.hal.science/tel-04165692>

Submitted on 19 Jul 2023

HAL is a multi-disciplinary open access archive for the deposit and dissemination of scientific research documents, whether they are published or not. The documents may come from teaching and research institutions in France or abroad, or from public or private research centers.

L'archive ouverte pluridisciplinaire **HAL**, est destinée au dépôt et à la diffusion de documents scientifiques de niveau recherche, publiés ou non, émanant des établissements d'enseignement et de recherche français ou étrangers, des laboratoires publics ou privés.



THÈSE de DOCTORAT DE L'UNIVERSITÉ CLAUDE BERNARD LYON 1

Ecole Doctorale ED52
Physique et Astrophysique

Discipline : Physique

Soutenue publiquement le 04/11/2022, par :
Nhung-Cam VU

Opening-gap Plasmonic Antennas: A Surface Plasmon Polariton Source

Devant le jury composé de :

DEL FATTI Natalia, Pr., Université Claude Bernard Lyon 1	Présidente
BOUHELIER Alexandre, Dr., Directeur de Recherche CNRS	Rapporteur
BRAMATI Alberto, Pr., Sorbonne Université	Rapporteur
DELEPORTE Emmanuelle, Pr., ENS Paris-Saclay	Examinatrice
LAVERDANT Julien, MCF, Université Claude Bernard Lyon 1	Directeur de thèse

UNIVERSITE CLAUDE BERNARD - LYON 1

Président de l'Université

M. le Professeur Frédéric FLEURY

Président du Conseil Académique

M. le Professeur Hamda BEN HADID

Vice-président du Conseil d'Administration

M. le Professeur Didier REVEL

Vice-président du Conseil Formation et Vie Universitaire

M. le Professeur Philippe CHEVALIER

Vice-président de la Commission Recherche

M. Fabrice VALLÉE

Directeur Général des Services

M. Alain HELLEU

COMPOSANTES SANTE

Faculté de Médecine Lyon Est – Claude Bernard

Directeur : M. le Professeur J. ETIENNE

Faculté de Médecine et de Maïeutique Lyon Sud – Charles Mérieux

Directeur : Mme la Professeure C. BURILLON

Faculté d'Odontologie

Directeur : M. le Professeur D. BOURGEOIS

Institut des Sciences Pharmaceutiques et Biologiques

Directeur : Mme la Professeure C. VINCIGUERRA

Institut des Sciences et Techniques de la Réadaptation

Directeur : M. X. PERROT

Département de formation et Centre de Recherche en Biologie Humaine

Directeur : Mme la Professeure A-M. SCHOTT

COMPOSANTES ET DEPARTEMENTS DE SCIENCES ET TECHNOLOGIE

Faculté des Sciences et Technologies

Directeur : M. F. DE MARCHI

Département Biologie

Directeur : M. le Professeur F. THEVENARD

Département Chimie Biochimie

Directeur : Mme C. FELIX

Département GEP

Directeur : M. Hassan HAMMOURI

Département Informatique

Directeur : M. le Professeur S. AKKOUCHE

Département Mathématiques

Directeur : M. le Professeur G. TOMANOV

Département Mécanique

Directeur : M. le Professeur H. BEN HADID

Département Physique

Directeur : M. le Professeur J-C PLENET

UFR Sciences et Techniques des Activités Physiques et Sportives

Directeur : M. Y.VANPOULLE

Observatoire des Sciences de l'Univers de Lyon

Directeur : M. B. GUIDERDONI

Polytech Lyon

Directeur : M. le Professeur E.PERRIN

Ecole Supérieure de Chimie Physique Electronique

Directeur : M. G. PIGNAULT

Institut Universitaire de Technologie de Lyon 1

Directeur : M. le Professeur C. VITON

Ecole Supérieure du Professorat et de l'Education

Directeur : M. le Professeur A. MOUGNIOTTE

Institut de Science Financière et d'Assurances

Directeur : M. N. LEBOISNE

Abstract

Nanopatch antennas based on metallic nanoparticles-on-mirror configuration offer great advantages as a potential source for launching surface plasmon polaritons (SPPs). In this work, we propose a plasmonic platform consisting of gold bipyramid nanoparticles (AuBPs) deposited over a gold thin film. A sub-10nm TiO₂ gap is introduced between the two metallic structures to prevent conductive contact. The synthesized AuBPs have the ability to support a strong localized surface plasmon resonance along its longitudinal axis which behaves like a radiating dipole. When the nanoparticles are brought to interact with the gold mirror, each AuBP resembles a nanoscale nanopatch antenna with an “opening-mouth”, which allows for effectively launching SPPs over the metallic surface around the bipyramid. In the terms of the experiment, we employ a leakage radiation microscope working in the dark-field configuration to study the scattering of the antenna and also excite and collect the SPPs. Here, we highlight the importance of the orientation effect in the optical response of the AuBPs. A rich mode structure ranging from the visible to the near-infrared regime is opened by tilting AuBP with one tip touching the substrate, whereas other orientations only display a single dipolar longitudinal mode. The plasmon modes exhibit both radiative nature and are confined within the gap. The COMSOL calculation confirmed that the plasmon gap mode behaves similarly to the Fabry-Pérot resonances. Finally, the bipyramid nanopatch is employed to optically excite SPPs, showing that the efficiency of launching SPPs is resonantly enhanced at the plasmon resonance wavelength of the mode. Especially, in the comparison to the plasmon generated by scattering from a dielectric bead nanoparticle of silica on the same gold substrate, the bipyramid nanopatch induces a greater SPPs efficiency by around 1 order of magnitude. These characteristics of the AuBP nanopatch can pave the way for electrically driven plasmon antennas, for which many applications such as energy harvesting or quantum information, are beneficial.

Résumé

Les antennes nanopatch basées sur une configuration de nanoparticules métalliques sur miroir offrent de grands avantages en tant que source potentielle pour lancer des polaritons de plasmon de surface (SPP). Dans ce travail, nous proposons une plateforme plasmonique constituée de nanoparticules en forme de bipyramide d'or (AuBP) déposées sur un film mince d'or. Une couche de TiO₂ inférieure à 10 nm est introduite entre les deux structures métalliques pour empêcher le contact conducteur. Les AuBPs synthétisées ont la capacité de supporter une forte résonance plasmonique de surface localisée le long de son axe longitudinal qui se comporte comme un dipôle rayonnant. Lorsque les nanoparticules sont amenées à interagir avec le miroir d'or, chaque AuBP ressemble à une antenne nanopatch à l'échelle nanométrique avec une "ouverture", qui permet de lancer efficacement des SPP sur la surface métallique autour de la bipyramide. Dans nos expériences, nous utilisons un microscope à franges radiatives fonctionnant dans la configuration de fond noir pour étudier la diffusion de l'antenne et également exciter et collecter les SPP. Ici, nous soulignons l'importance de l'effet d'orientation dans la réponse optique des AuBPs. Une structure de mode riche allant du régime visible au proche infrarouge apparaît en inclinant l'AuBP quand la pointe touche le substrat, tandis que d'autres orientations n'affichent qu'un seul mode longitudinal dipolaire. Les modes de plasmon présentent à la fois une nature radiative et sont confinés dans l'espace. Le calcul COMSOL a confirmé que le mode gap plasmon se comporte de manière similaire aux résonances de Fabry-Pérot. Enfin, le nanopatch bipyramide est utilisé pour exciter optiquement les SPP, montrant que l'efficacité du lancement des SPP est améliorée à la longueur d'onde de résonance du mode. En particulier, en comparaison avec le plasmon généré par diffusion à partir d'une nanoparticule de billes diélectriques de silice sur le même substrat d'or, le nanopatch bipyramide induit une plus grande efficacité des SPP d'environ 1 ordre de grandeur. Ces caractéristiques du nanopatch AuBP peuvent ouvrir la voie à des antennes à plasmon à commande électrique, pour lesquelles de nombreuses applications telles que la récupération d'énergie ou l'information quantique, sont bénéfiques.

Acknowledgements

First and foremost, I would like to express my gratitude to my thesis director Julien Laverdant for his tremendous guidance and open discussion. Thanks for giving me the freedom to be right and to be wrong, plenty of opportunities to strengthen my abilities, and sincere advice on any topic.

I would also like to thank members of my thesis committee: Alexandre Bouhelier, Bramati Alberto, Natalia Del Fatti, and Emmanuelle Deleporte, who have accepted to participate in my jury. Thank you also for all your remarks and corrections after the defence, particularly to Alexandre and Bramati for taking time to review my work with many insights of the work.

I am also grateful to the members and Ph.D students of the Agrégats et Nanostructures (AgNano) team: Emmanuel Cottatin, Christophe Bonnet, Jean Lermé, Michel Pellarin, Marie-Ange Lebeault, Michel Broyer, Mathias Hillenkamp, Sylvain Hermelin, Elise Camus, and Floriane Perrier. I really enjoy the time to be a part of the team for the past three years.

This Thesis would have been completed without the fruits of the collaboration with Frédéric Lerouge from ENS Lyon; Michel Pellarin, Remy Fulcrand, and Emmanuel Cottatin from iLM; Laurent Coolen, Agnès Maitre, and Zakarya Ouzit from INSP (Paris); Stephanie Buil and Bruno Bérini from GEMaC (UVSQ). I deeply thank all of you for your always generous support.

Thanks to my sisters, Ngà and Hanh, who have shared with me both joy and sadness from the early dates of our Ph.D. in France. Thanks to my friend, Hong, for her endless positive energy and lovely distractions from writing.

Big thanks to my friends and family in Vietnam, always love me and support me unconditionally. They are my motivation to be better every passing day.

Lastly, sincerely thanks to myself of the last 5 year.

Introduction

Plasmonic antennas are analogs of radio antennas that transfer electromagnetic energy from free space to localized fields, and vice versa. The attractiveness of plasmonic nanostructures is the ability to concentrate light into deep sub-wavelength volumes and offer relative broad optical resonances while plasmons can propagate over micrometer distances. Plasmonic nanoantennas are pervasive in various domains of modern technologies, ranging from sub-nanometer resolution optical imaging, quantum information processing, energy harvesting, and conversion, to biological sensing [1]. For instance, recent advances in nanofabrication allow to couple a single emitter into metallic nanostructures, thus increasing the spontaneous emission rate of the emitter, making it becomes a reliable ultrafast photon source [2]. A promising route towards using advantageously plasmonics to construct optically thick but physically very thin photovoltaic absorbers for solar energy harvesting [1]. To bring plasmonic antennas into the practical realm, it is critical to optimize the energy transfer between a localized source and the free-space radiation. Several challenging requirements must be met, including large local density of optical states (LDOS) enhancement, good photon-radiation efficiency, and the ability to control the emission direction.

A single metallic nanoparticle with sharp corners can strongly confine light to volume with dimensions in the range of 10-100nm [3]. Even more tightly confined fields – on the scale of sub-10nm – can be achieved by coupling nanoparticle plasmons together in a dimer configuration. However, a major challenge is to separate individual nanostructures precisely and reproducibly in the subnanometer scale. An alternative promising route toward controlling plasmonic gaps is provided by nanopatch antennas in a nanoparticle-on-mirror (NPoM) configuration, where a metallic nanoparticle is separated from a metallic film by a thin dielectric layer, which behaves similarly to a dimer of nanoparticles [4]. The attractiveness

of the plasmonic nanopatch or NPoM is that large numbers of plasmonic nanogaps can be fabricated in a controllable and reproducible manner, and thus extend their uses in various practical applications.

Generally, the optical response of the nanopatch based on nanoparticle-on-mirror geometry is strongly modified by the exact geometry of the overlying particle, especially by the bottom facet that contacts the underlying metallic film. Nanospheres and nanocubes are the most extensively used and studied to produce the gap plasmon for the patch antenna, thanks to their symmetrical geometry. However, when it moves to less symmetrical particles, more degrees of freedom are required to be controlled. In the framework of this Thesis, we aim to study a new kind of nanopatch antenna made from gold bipyramid nanoparticles (AuBPs) placed separately above a thin gold film, focusing on investigating one of the most crucial degrees of freedom induced by the elongated shape of particle: its 3D orientation. The optical responses of a single AuBP have been well studied in the team previously [5], showing that that particle has the ability to support strongly localized surface plasmon resonances along its longitudinal axis and allow to tightly confine field around its sharp tip ends. In our work, we harvest these distinctive characteristics of the individual AuBPs and couple them to the metallic film, from which a rich optical response hybridized between confined gap plasmon and radiating localized plasmon is opened. This structure is then employed to optically excite surface plasmon polaritons propagating on the gold film.

In Chapter 1, we set out the basic concepts of surface plasmon polaritons. We begin this chapter with fundamental discussions of the interaction of light and metals, where their ability to confine light below the diffraction limit is highlighted. Subsequently, both propagating and localized surface plasmon at the planar and confined metallic structures is presented, which provides a profound understanding of the plasmon hybridization in the following chapter.

In Chapter 2, we investigate numerically the surface plasmon hybridization in alternative multilayers of dielectric/metal by using a dipole as a probe. We start by showing how we can use the classical approach to study the spontaneous emission of the dipole. The optical modes supported by the multilayer metallic structures are then identified from the spatial spectrum of the dissipated power of the dipole. In this Chapter, we mainly focus on a practical long-range surface plasmon device and alternative N-stacks of metallic and insulator thin film.

Excitation and collection of surface plasmon can be done in the far field. In Chapter 3, we present the experimental methods that are employed to investigate the optical responses of the nanopatch. In which, a dark-field microscope equipped with Fourier-plane filtering to measure scattering spectra of the nanoparticles. Besides, the leakage radiation microscope is applied to efficiently collect the SPPs.

Owing to the elongated geometry, the random deposition of bipyramid nanoparticles on a flat substrate can induce many orientations of the particle, which as will be shown later results in significantly different optical responses. Chapter 4 is therefore dedicated to presenting the measurement of the 3D orientation of the bipyramids on the glass substrate. The orientation is measured by polarization analysis of the longitudinal localized surface plasmon resonance of the bipyramid, which behaves like a linear dipole. We demonstrate that the bipyramids display two main orientations: lying horizontal to the surface or tilting with a tip touching the surface.

In Chapter 5, we introduce the opening-gap nanopatch antenna which consists of bipyramids deposited separately on the gold film by a dielectric spacer. We prove explicitly that tilting bipyramids on the surface can enhance the interaction strength of the particles and the underlying substrate, from which various optical modes are opened with interesting behaviors: radiative and confined inside the gap like Fabry-Pérot resonances. The nature of these plasmon modes is identified with the support of the COMSOL simulation.

The SPPs can offer great potential for various photonic applications thanks to their ability to concentrate light in space in time. In Chapter 6, we therefore employ scattering from the bipyramid nanopatch antenna to optically launch SPPs. Besides fundamental properties of the SPPs such as propagation length or dispersion are well characterized, we also measure the SPP emission efficiency of the antenna and seek to comparison to a dielectric nanobead. The physical mechanisms involved in generating SPPs also will be discussed.

The results in this Thesis demonstrate the potential of the opening-gap plasmon antennas based on gold bipyramids to confine light to the nanoscale and convert it into desired output channel of SPPs. Such properties may be utilized as a flexible platform for surface energy transfers over a long distance and in a very short time, which can be applied in perspective to various practical fields such as sensing, photovoltaics, and optoelectronic devices.

Résumé substantiel en français

Les antennes plasmoniques sont analogues aux antennes radio qui transfèrent l'énergie électromagnétique de l'espace libre vers des champs localisés, et vice versa. L'attrait des nanostructures plasmoniques est la capacité de concentrer la lumière dans des volumes profonds de dimensions sub-longueur d'onde et d'offrir des résonances optiques relativement larges tandis que les plasmons peuvent se propager sur des distances micrométriques. Les nanoantennes plasmoniques sont omniprésentes dans divers domaines des technologies modernes, allant de l'imagerie optique à résolution inférieure au nanomètre, du traitement de l'information quantique, de la récupération et de la conversion d'énergie, à la détection biologique [1]. Par exemple, les progrès récents en nanofabrication permettent de coupler un seul émetteur dans des nanostructures métalliques, augmentant ainsi le taux d'émission spontanée de l'émetteur, ce qui en fait une source de photons ultra-rapide fiable [2]. Une voie prometteuse est l'utilisation avantageuse de la plasmonique pour construire des absorbeurs photovoltaïques optiquement épais mais physiquement très fins pour la récupération de l'énergie solaire [1]. Pour amener les antennes plasmoniques dans le domaine pratique, il est essentiel d'optimiser le transfert d'énergie entre une source localisée et le rayonnement en espace libre. Plusieurs exigences difficiles doivent être satisfaites, notamment une amélioration de la grande densité locale d'états optiques (LDOS), une bonne efficacité du rayonnement photonique et la capacité de contrôler la direction d'émission.

Une seule nanoparticule métallique aux angles vifs peut fortement confiner la lumière dans un volume dont les dimensions sont comprises entre 10 et 100 nm [3]. Des champs encore plus étroitement confinés - à l'échelle inférieure à 10 nm - peuvent être obtenus en couplant des plasmons de nanoparticules ensemble dans une configuration dimère. Cependant, un défi majeur consiste à séparer les nanostructures individuelles de manière précise

et reproductible dans le régime subnanométrique. Une voie alternative prometteuse vers le contrôle des lacunes plasmoniques est fournie par les antennes nanopatch dans une configuration de type nanoparticules sur miroir (NPoM), où une nanoparticule métallique est séparée d'un film métallique par une fine couche diélectrique, qui se comporte de manière similaire à un dimère de nanoparticules [4]. L'attrait du nanopatch plasmonique ou NPoM est qu'un grand nombre de nanogaps plasmoniques peuvent être fabriqués de manière contrôlable et reproductible, et ainsi étendre leurs utilisations dans diverses applications pratiques.

Généralement, la réponse optique du nanopatch basée sur la géométrie des nanoparticules sur miroir est fortement modifiée par la géométrie exacte de la base géométrique de la nanoparticule, en particulier par la facette inférieure qui entre en interaction avec le film métallique sous-jacent. Les nanosphères et les nanocubes sont les plus largement utilisés et étudiés pour produire le plasmon gap pour l'antenne patch, grâce à leur géométrie symétrique. Cependant, lorsqu'il se déplace vers des particules moins symétriques, plus de degrés de liberté doivent être contrôlés. Dans le cadre de cette thèse, nous visons à étudier un nouveau type d'antenne nanopatch fabriquée à partir de nano-bipyramides d'or (AuBP) placées séparément au-dessus d'un mince film d'or, en nous concentrant sur l'étude de l'un des degrés de liberté les plus cruciaux induits par la forme allongée de particule : son orientation 3D. Les réponses optiques d'une seule AuBP ont été bien étudiées dans l'équipe précédemment [5], montrant que cette particule a la capacité de supporter des résonances de plasmon de surface fortement localisées le long de son axe longitudinal et de permettre de confiner le champ autour de ses extrémités pointues. Dans notre travail, nous utilisons ces caractéristiques distinctives des AuBP individuels en les couplant au film métallique, à partir duquel une réponse optique riche hybride entre le plasmon à espace confiné et le plasmon localisé rayonnant est attendue. Cette structure est ensuite utilisée pour exciter optiquement des plasmons polaritons de surface se propageant sur le film d'or.

Dans le chapitre 1, nous exposons les concepts de base des polaritons des plasmons de surface. Nous commençons ce chapitre par des discussions fondamentales sur l'interaction de la lumière et des métaux, où leur capacité à confiner la lumière en dessous de la limite de diffraction est mise en évidence. Par la suite, le plasmon de surface se propageant et localisé au niveau des structures métalliques planes et confinées est présenté, ce qui nous permet de

fournir une compréhension approfondie de l'hybridation du plasmon dans le chapitre suivant.

Dans le chapitre 2, nous étudions numériquement l'hybridation des plasmons de surface dans des multicouches alternatives de diélectrique/métal en utilisant un dipôle comme sonde. Nous commençons par montrer comment nous pouvons utiliser l'approche classique pour étudier l'émission spontanée du dipôle. Les modes optiques supportés par les structures métalliques multicouches sont alors identifiés à partir du spectre spatial de la puissance dissipée du dipôle. Dans ce chapitre, nous nous concentrons principalement sur un dispositif pratique à plasmons de surface à longue portée et sur des piles N alternatives de couches minces métalliques et isolantes.

L'excitation et la collection des plasmons de surface peuvent se faire en champ lointain. Dans le chapitre 3, nous présentons les méthodes expérimentales utilisées pour étudier les réponses optiques du nanopatch. Un microscope à champ noir utilisant la manipulation du plan de Fourier a été mis en place pour mesurer les spectres de diffusion des nanoparticules. En outre, le microscope à fuite radiative nous permet pour collecter efficacement les SPP.

En raison de leur géométrie, le dépôt aléatoire des bipyramides sur un substrat plat peut induire de nombreuses orientations des particules, ce qui, comme on le verra plus loin, se traduit par des réponses optiques significativement différentes. Le chapitre 4 est donc consacré à la présentation de la mesure de l'orientation 3D des bipyramides à l'échelle individuelle sur substrat de verre. L'orientation est mesurée par une analyse fine de la polarisation diffusée par la résonance plasmon longitudinale de la bipyramide. Cette réponse peut être modélisée comme un dipôle linéaire. Nous démontrons que les bipyramides affichent deux orientations principales : couché horizontalement à la surface ou inclinée avec une pointe touchant la surface.

Dans le chapitre 5, nous introduisons l'antenne nanopatch à ouverture de gap formée par des bipyramides déposées séparément d'un film d'or par une fine couche diélectrique. Nous prouvons explicitement que l'inclinaison des bipyramides sur la surface peut améliorer la force d'interaction des particules avec le substrat sous-jacent, à partir de laquelle différents modes optiques sont créés avec des comportements intéressants : radiatifs et confinés à l'intérieur de l'entrefer comme les résonances de Fabry-Pérot. La nature de ces modes plasmons est identifiée à l'aide de la simulation COMSOL.

Les SPP peuvent offrir un grand potentiel pour diverses applications photoniques grâce à leur capacité à concentrer la lumière dans l'espace et dans le temps. Dans le chapitre 6, nous utilisons donc la diffusion de l'antenne nanopatch bipyramide pour lancer optiquement les SPPs. Outre les propriétés fondamentales des SPP telles que la longueur de propagation ou la dispersion sont bien caractérisées, nous mesurons également l'efficacité d'émission SPP de l'antenne et cherchons à la comparer à une nanobille diélectrique de silice. Les mécanismes physiques impliqués dans la génération des SPP seront également discutés.

Les résultats de cette thèse démontrent le potentiel des antennes à plasmon à ouverture de gap basées sur des bipyramides d'or pour confiner la lumière à l'échelle nanométrique et la convertir en canal de sortie souhaité de plasmon de surface. De telles propriétés peuvent être utilisées comme plate-forme flexible pour les transferts d'énergie de surface sur une longue distance et en très peu de temps, qui peuvent être appliquées en perspective à divers domaines pratiques tels que la spectroscopie, la détection, le photovoltaïque et les dispositifs optoélectroniques.

Contents

1	Surface Plasmon Polaritons	15
1.1	Metals and Light: Material perspective	16
1.1.1	Dielectric function of bulk metals	16
1.1.2	Light confinement in metals	19
1.1.3	The loss in metal	22
1.2	Surface plasmon polaritons at a single interface	24
1.3	Plasmon hybridization in planar structures	30
1.4	Localized surface plasmon of metallic nanoparticles	33
1.4.1	Scattering, absorption and extinction	34
1.4.2	Quasi-static approximation	38
1.4.3	Mie theory	41
2	Coupling a dipole to multilayer surface plasmon devices	45
2.1	Spontaneous emission of an emitter	46
2.2	Spontaneous emission of a dipole near planar interfaces	51
2.3	Coupling a dipole to fundamental planar plasmonic structures	53
2.4	Coupling a single dipole to a long-range surface plasmon device	59
2.5	Surface plasmon hybridized dressed states	64
3	Experimental methods for Surface Plasmons	70
3.1	Investigation of the optical response of metallic nanoparticles	71
3.2	Dark-field scattering polarimetry	73
3.2.1	Dark-field imaging by Fourier-plane filtering	73
3.2.2	Single metallic nanoparticle spectroscopy	77
3.2.3	Scattering polarimetry	79
3.3	Exciting and imaging propagating surface plasmon	80
3.4	Launching SPPs by leakage radiation microscopy	84
3.5	Launching SPPs by scattering from a point source	87
4	Measuring the 3D Orientation of Single Gold Bipyramid Nanoparticle	89
4.1	Properties of Gold Bipyramid nanoparticles	90
4.2	Scattering polarimetry for orientation measurement	93
4.3	Orientation of the AuBPs on the glass substrate	97
4.4	Role of collection numerical aperture	99
4.5	Conclusion	104

5	Opening-gap nanopatch antennas	105
5.1	Introduction to opening-gap nanopatch antennas	106
5.2	Characterization methods	113
5.3	Gold bipyramids on a high refractive index substrate	116
5.4	Gold bipyramids on the gold film	122
	5.4.1 Scattering spectra	122
	5.4.2 Physical formation of the modes	126
5.5	The complexity of the AuBP nanopatch antenna	129
5.6	Conclusion	131
6	Optically launching of Surface Plasmon Polaritons by Bipyramid Nanopatch Antennas	133
6.1	SPP emission spectrum	134
6.2	Spatial and angular emission of SPPs	136
6.3	SPP emission efficiency	139
6.4	Role of nanopatch antenna in SPP emission	144
6.5	Conclusion	148
	Conclusion and Perspectives	149

Chapter 1

Surface Plasmon Polaritons

As the ultimate goal of this work is to investigate the optical response of a plasmonic structure that hybrids between the nanoparticle and metallic film, it is necessary to begin with the properties of the individuals. This Chapter thus aims to provide the underlying theory of light-metal interaction. It begins with a basic description of the optical response of bulk metal, discussing both pros and cons of using metallic material for light confinement. From there, the propagating surface plasmon polaritons (SPPs) at a single dielectric/metal interface and their hybridization in the three-multilayer structures will be considered. On the other hand, the confinement of the surface plasmon in the nanoparticles of the finite dimensions yields distinctive optical spectra through the phenomenon of localized surface plasmon resonance (LSPR). The quasi-static approximation and Mie theory will be discussed to introduce the basic theory of localized surface plasmon resonance.

Contents

1.1	Metals and Light: Material perspective	16
1.1.1	Dielectric function of bulk metals	16
1.1.2	Light confinement in metals	19
1.1.3	The loss in metal	22
1.2	Surface plasmon polaritons at a single interface	24
1.3	Plasmon hybridization in planar structures	30
1.4	Localized surface plasmon of metallic nanoparticles	33
1.4.1	Scattering, absorption and extinction	34
1.4.2	Quasi-static approximation	38
1.4.3	Mie theory	41

1.1 Metals and Light: Material perspective

1.1.1 Dielectric function of bulk metals

The optical response of the metal can be described by its dielectric functions, which reflect its electronic structure. We follow Drude [6] in making a simple model studying the collective response of metal in interaction with light. Classically, the metal is constructed from a lattice of stationary periodic ions with conduction electrons freely moving around. The free electrons of density N_e (number of electrons per unit volume in the undisturbed state, $N_e \sim 10^{23} \text{ cm}^{-3}$ [7]) are treated as classical particles, which have a given mass m_e , elementary charge e , and moving with velocity v . The Drude model solves the motion of the free electrons induced by the applied electromagnetic (EM) field with harmonic time dependence $\vec{E}(t) = \vec{E}_0 e^{-i\omega t}$

using Newton's equation. The model approximates that the electrons are not subjected to magnetic forces and electric fields from other electrons (i.e., no restoring force or potential energy is zero). During the movement of the electrons under the EM field, they are damped via collisions with other particles (electrons, ions, defects) at an average rate of γ_0 . The equation of motion for one electron can be expressed as:

$$m_e \frac{d^2 \vec{x}}{dt^2} = -e \vec{E}(t) - m_e \gamma_0 \frac{d\vec{x}}{dt} \quad (1.1)$$

As the driving field is the harmonic oscillation and without restoring force, the electron also oscillates at the same frequency ω as the incident field; its position is defined as $\vec{x}(t) = \vec{x}_0 e^{-i\omega t}$. Replacing the exponential expression of the $\vec{x}(t)$ and $\vec{E}(t)$ into the equation 1.1, we found the position of the electron displaced by the incident field as:

$$\vec{x}(t) = \frac{e}{m_e(\omega^2 + i\omega\gamma_0)} \vec{E}(t) \quad (1.2)$$

For one electron, its charge displacement induces a dipole with a moment $\vec{p} = -e\vec{x}$. In the case of many electrons with the number density N_e , all of them will contribute to the macroscopic polarization \vec{P} of the metal and are given by

$$\vec{P} = N_e \vec{p} = -\frac{N_e e^2}{m_e(\omega^2 + i\omega\gamma_0)} \vec{E}(t) \quad (1.3)$$

To find the dielectric function of the material, we recall the basic definitions of the macroscopic polarization \vec{P} and electric displacement \vec{D} of a linear, isotropic, and nonmagnetic medium: $\vec{P} = \varepsilon_0 \chi \vec{E}$ and $\vec{D} = \varepsilon_0 \vec{E} + \vec{P} = \varepsilon_0 \varepsilon(\omega) \vec{E}$, with $\varepsilon(\omega) = \chi + 1$ is the relative dielectric function of the metal and χ is the dielectric susceptibility, ε_0 is the electric permittivity ¹ of vacuum. We identify the Drude dielectric function of the bulk metal as

$$\varepsilon^D(\omega) = 1 - \frac{\omega_p^2}{\omega^2 + i\omega\gamma_0} \quad (1.4)$$

where $\omega_p^2 = \frac{N_e e^2}{\varepsilon_0 m_e}$ is the plasma frequency – a natural frequency of a local charge density

¹ $\varepsilon_0 \approx 8.854 \times 10^{-12} \text{ F/m}$

(plasma electrons) that oscillates collectively in response to a fluctuation [8], which is as shown depending on the electron density. From the complex expression of the dielectric function $\varepsilon_r(\omega)$, we derive its real and imaginary part in the condition of small damping $\gamma_0 \ll \omega$ as

$$\begin{aligned} \text{Re}[\varepsilon^D(\omega)] &= 1 - \frac{\omega_p^2}{\omega^2 + \gamma_0^2} \approx 1 - \frac{\omega_p^2}{\omega^2} \\ \text{Im}[\varepsilon^D(\omega)] &= \frac{\gamma_0 \omega_p^2}{\omega(\omega^2 + \gamma_0^2)} \approx \frac{\omega_p^2}{\omega^3} \gamma_0 \end{aligned} \quad (1.5)$$

Behavior of the Drude dielectric function

Roughly, in the case of simple metals, Drude model can successfully interpret the optical properties of metals such as

- For $\omega < \omega_p$ and is very close to ω_p : the real part of $\varepsilon^D(\omega)$ is predominant and negative, resulting in a complex wavevector of light in metal $k = \pm i\sqrt{|\varepsilon^D|}\omega/c$. This means that the light is evanescent inside metal and cannot go through that is strongly reflected at the interface. This also explains why gold and silver are good optical reflectors in the visible to mid-infrared regions since their plasma wavelength is $\lambda_p = 2\pi c/\omega_p \approx 200\text{nm}$.
- For $\omega = \omega_p$: the real part of $\varepsilon^D(\omega)$ is equal zero. This means that all the electrons oscillate in phase throughout the metal propagation length. This oscillation is known as plasma oscillation.
- For $\omega > \omega_p$: the $\varepsilon^D(\omega)$ is almost real and positive. Therefore, the light can propagate through the metal, making it being transparent.

Dielectric function of noble metals

The description of the optical response of metals by Drude model is only valid for photon energies below interband transition of metal, which will be discuss in more detail later. Intuitively, Drude model is not adequate at the large frequency ($\omega \gg \omega_p$) because electrons are not completely free anymore, i.e. their energy band structure is not perfectly a parabolic [10]. Figure 1.1 displays a comparison between the dielectric function of gold and silver calculated by the Drude model and those measured by Johnson and Christy [11]. As can be seen in the imaginary part of $\varepsilon^D(\omega)$, the validity of the Drude model curve breaks down at the occurrence of interband transitions: E_{IB} (gold) $\sim 2\text{eV}$ (650nm) and E_{IB} (silver) $\sim 4\text{eV}$

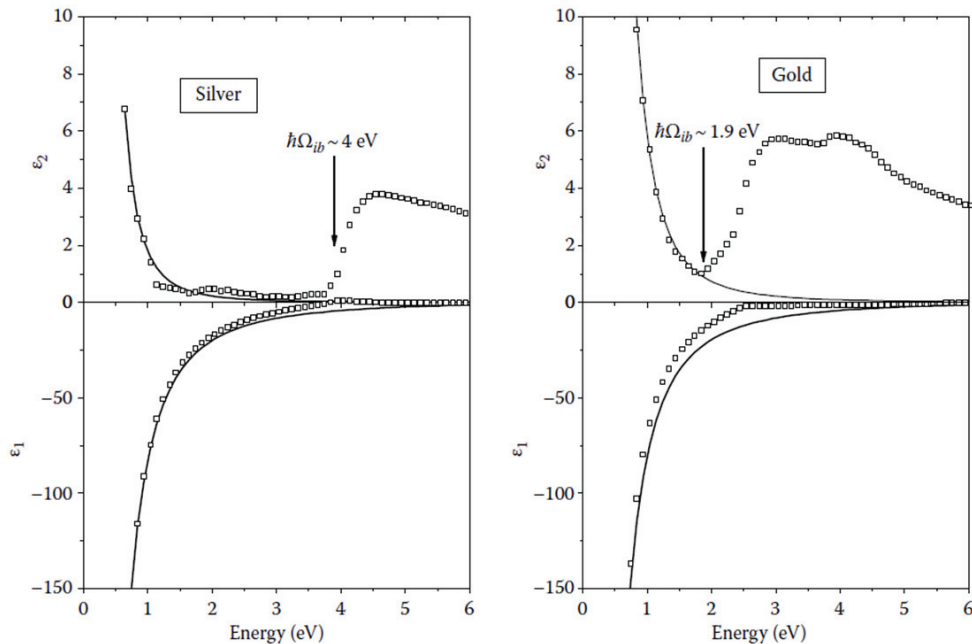


Figure 1.1: **Real (ϵ_1) and imaginary (ϵ_2) parts of dielectric function of gold and silver.** Solid lines are the Drude model and squares are experimental measurement of Johnson and Christy. $\hbar\omega_{IB}$ is the interband transition threshold. Source: E.Cottantin et al. [9]

(330nm). Therefore, to calculate the dielectric function of the noble metals at energy above E_{IB} , we need to take the interband transition into account. The dielectric function then has an additional term ϵ^{IB} [6, 9]:

$$\epsilon = \epsilon^D + \epsilon^{IB} - 1 \quad (1.6)$$

Here, ϵ^{IB} is related to interband transition, which mostly accounted of the contribution of the d-core electrons [6].

1.1.2 Light confinement in metals

Light emission plays an instrumental role in ant areas where advanced technological applications are desired. In general, the interaction of light with single emitters, such as molecules or nanocrystals, is inefficient because of the dimension mismatch between the point-like character of such emitters and the limit-diffraction light beam. Light confinement at the nanoscale is thus the fundamental role of nanophotonics.

From a material perspective, there are two strategies for the light localization using: (i) high-index dielectrics or (ii) negative-permittivity materials such as metals or doped semiconductors. Using the high-index dielectric materials allows for reducing the wavelength to λ/n , with $n \sim 3$ (Si, Ge, GaP,..) [12, 13], which is usually prevented by the limit of diffraction (this might be broken down by the nanoscale dielectric discontinuities [14, 13]). On the other hand, metals allow light concentration beyond the diffraction limit by coupling electromagnetic fields to the large momentum of the conduction electrons. This diffraction limit beating also can be interpreted from an energy conversation point-of-view based on the work of J.Khurgin [15], as illustrated in Figure 1.2.

Here, the light oscillates inside the finite dimension materials which is considered as an optical resonator. For dielectrics with refractive index n (Figure 1.2 a and b), depending on the resonator' size a , the electric or magnetic fields might have different harmonic spatial dependence

$$\begin{aligned} \vec{E} &= \vec{E}_0 e^{-i\omega t} e^{i\frac{2\pi}{\lambda}z}, & \vec{H} &= \vec{H}_0 e^{-i\omega t} e^{i\frac{2\pi}{\lambda}z} & (a > \frac{\lambda}{2n}) \\ \vec{E} &= \vec{E}_0 e^{-i\omega t} e^{i\frac{\pi}{a}z}, & \vec{H} &= \vec{H}_0 e^{-i\omega t} e^{i\frac{\pi}{a}z} & (a < \frac{\lambda}{2n}) \end{aligned} \quad (1.7)$$

For the resonator size beyond the limit of diffraction ($a > \frac{\lambda}{2n}$), from the two first Maxwell's equations $\nabla \vec{H} = \varepsilon \partial \vec{E} / \partial t$ and $\nabla \times \vec{E} = -\mu \partial \vec{H} / \partial t$, we can find a similar relation between the magnetic and electric fields as $H = \sqrt{\varepsilon/\mu} E$, resulting in an equal average electric field and magnetic energies: $u_E = \frac{\varepsilon E^2}{2} = u_H = \frac{\mu H^2}{2}$. This means that the energy inside the resonator converts between the electric energy u_E and magnetic energy u_H , which is analogous to the energy transformation between the kinetic energy and potential energy in a mechanical harmonic oscillator for "self-sustaining oscillation".

For the dielectric resonator with sub-wavelength size, resolving the first Maxwell's equation gives $H = \frac{a}{\lambda/2n} \sqrt{\varepsilon/\mu} E$, which is much smaller than E due to $a \ll \lambda$. Subsequently, the magnetic energy is also much smaller than electric energy $u_H \ll u_E$, the self-oscillation cannot be maintained, hence the energy is dissipated outside the resonator as expected from the diffraction limit. Besides, since the magnetic field is so small, the second Maxwell's equation requires that the electric field must be irrotational, resembling an electrostatic field at a sub-wavelength regime.

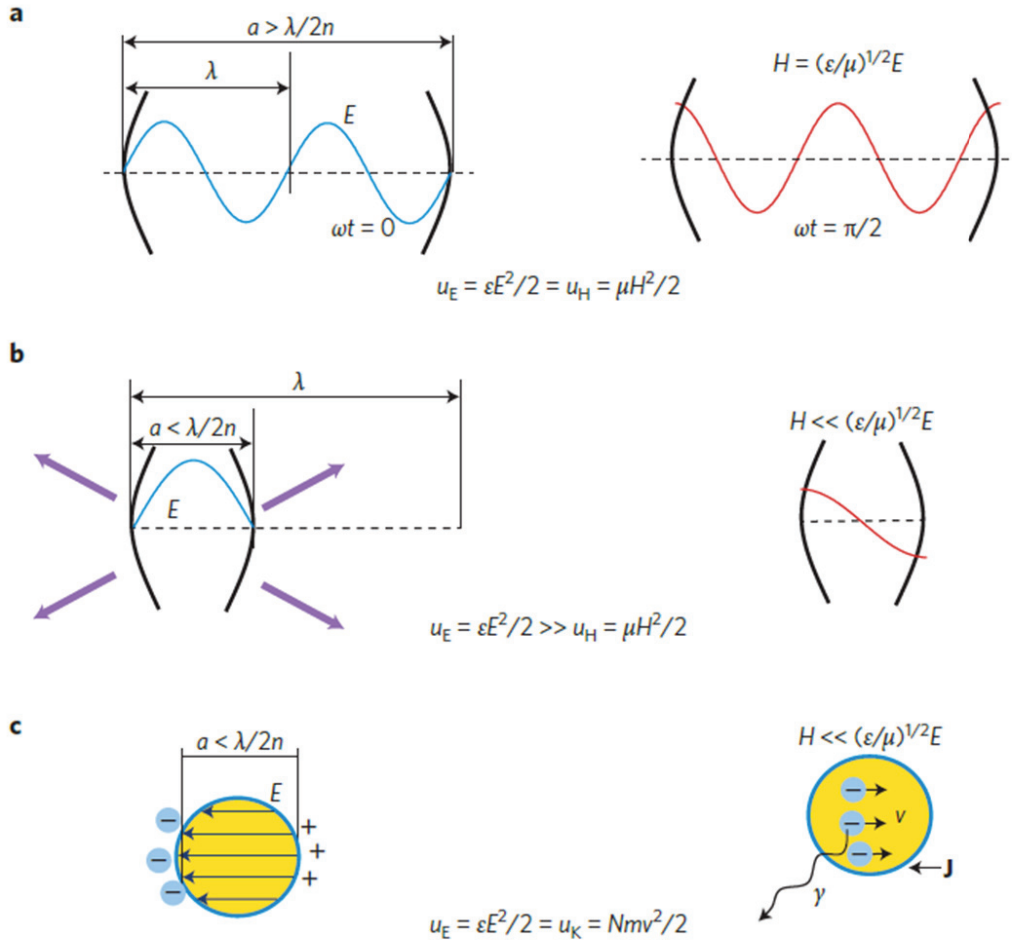


Figure 1.2: **Energy balance in photonic and plasmonic structures.**(a) Optical resonator size $a > \lambda/2n$, energy converts between electric u_E and magnetic energy u_H in order to self sustain oscillation. Below the limit of diffraction:(b) magnetic energy of dielectric resonator is too small, the energy is dissipated outside the resonator; (c) metallic resonator of sub-wavelength dimension can beat the diffraction limit by storing energy in the kinetic energy of free carriers. Source: J. Khurgin [15].

In contrast, the metallic resonator can store the dissipated energy below the diffraction limit in the form of the kinetic energy of the free electrons, which can be quantified by the Drude model (Figure 1.2c). In response to the applied EM field, the movement of electrons introduces an internal current density $\vec{j} = -N_e e \vec{v}$ which delivers a power $P_j = 1/2 \text{Re}(\vec{j} \vec{E}^*)$. This power is associated with the rate change of the kinetic energy of the free electrons². Assuming the damping is small $\gamma_0 \ll \omega$ we can find the average kinetic energy $u_K =$

²the potential energy is zero

$1/2mv^2 \approx \frac{1}{2}\epsilon_0\frac{\omega_p^2}{\omega^2}E^2$. Therefore, at a certain frequency ω , the u_K can compensate for the small magnetic energy and make a balanced exchange with the electric energy u_E . In other words, in metals, the energy coherently oscillates between the electric and kinetic energy of free electrons, and thus allow the light to be stored its electric energy at below limit of diffraction.

For example, Figure 1.3 shows state-of-art optical cavities made from dielectric or metallic of different structures used to boost light-matter interaction (accelerating the spontaneous emission rate of emitters for example). Comparisons between cavities are based on two figure-of-merits: (i) the time of the photon is trapped inside the cavity characterized by the quality factor $Q = \omega/\Delta\omega$ ($\Delta\omega$ is the spectral width of the resonance) and (ii) the optical mode volume V_{eff} allows to confine the light. A combination of a large quality factor and a small volume mode is thus essential for enhancing light-matter interaction. The dielectric cavities can offer huge Q values ($10^3 - 10^8$) by trapping photons traveling back and forth in between Bragg mirrors of the Fabry-Pérot cavity [16, 17], or moving circularly inside the whispering gallery resonator (spheres or toroids) [18, 19], or making its slowdown in the dielectric band gap of photonic crystals [20]. In turn, the reduction of mode volume is prevented by the diffraction limits. As a counterpart, the metallic cavities allow localized the field into deep-subwavelength volume near the tips of elongated nanoparticles [21] or inside the gap structures [22, 23]. However, this success comes at a price of a low-quality factor due to strong losses.

1.1.3 The loss in metal

As discussed above, free electrons in metals can drag photons below the diffraction limit by storing their electric field energy in the kinetic energy, which however can get lost via dissipative damping of electron motion. Consider a simplified energy band structure that results from the outer elections of metals in Figure 1.4, from which the hybrid $ns - p$ band is separated spatially from the $(n - 1)d$ band.

The $ns - p$ band is only partially filled (conduction band), all below the Fermi level of energy E_F – the highest energy that electrons can occupy at 0K. By absorbing photons, the electrons from the unoccupied states inside $ns - p$ band can be promoted into the unoc-

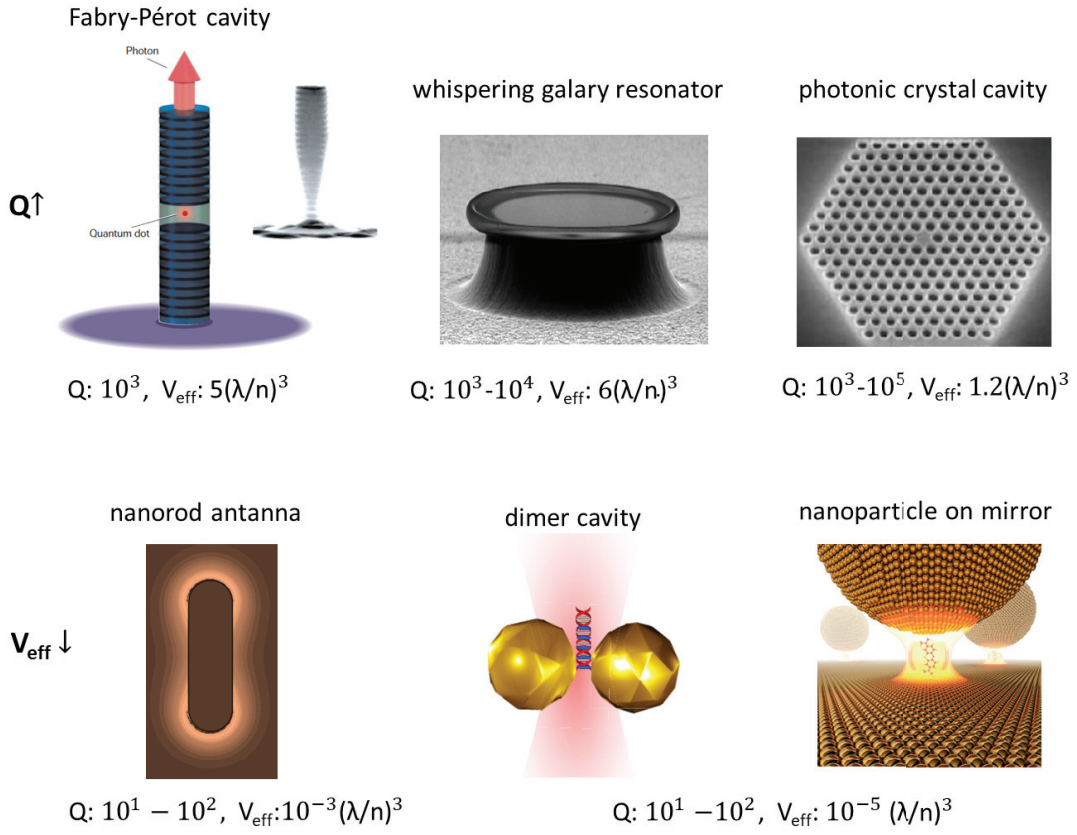


Figure 1.3: **Cavities for enhanced light-emitter interaction.** Upper row: dielectric microcavities provide high quality factor Q but usually, they can only focus light in the scale of wavelengths. Lower row: plasmonic resonators/cavities hold the modest value of Q but the light is confined to the deep sub-wavelength volume V_{eff} . Adapted from [24, 18, 20, 21, 23, 22]

occupied region above the Fermi level and move almost freely throughout the crystal. Such optical transitions are called intraband transitions and take place in the visible and near-IR range, which will be the most interesting in the works that follow. However, because electron momentum is much larger than that of photons, the absorption loss during the intraband transitions is thus unavoidable due to the momentum conservation. The absorption can be assisted by several processes such as (i) phonons accompanied by the generation of “hot” electrons and holes (i.e. charge carriers with significant additional energy before they thermalize via scattering [15]), (ii) electron-electron scattering that many carriers might involve in dissipating photon energy, and (iii) direct absorption induced by large momentum of tightly confined plasmon mode when the particle size $a \ll \lambda/2$ (Landau damping). In addition, if a sufficiently energetic photon is absorbed, electrons from the fully filled $(n - 1)d$ band

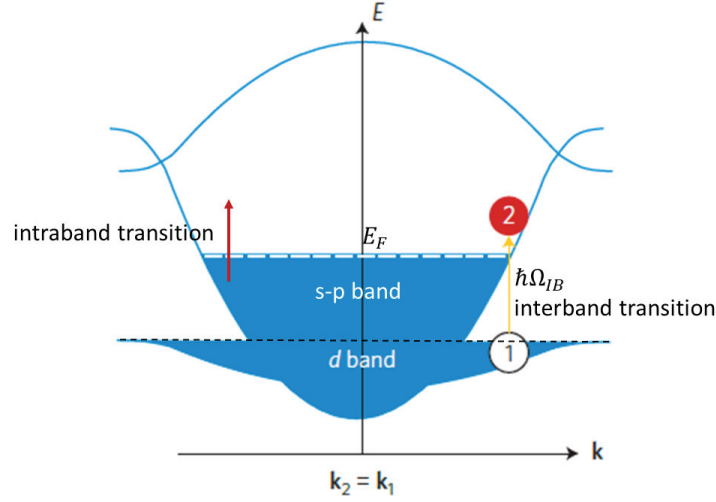


Figure 1.4: **Optical transitions of the noble metals with schematic dispersion relation of $(n-1)d$ band and $ns-p$ band.** Intraband transitions take place inside $ns-p$ band, whereas the interband transitions between the $(n-1)d$ band and conduction band requires an energy threshold $\hbar\Omega_{IB}$. Adapted from J. Khurgin [15].

(valence band) can be excited to the unoccupied levels of the $ns-p$ band. This band-to-band transition is a so-called interband transition that requires a photon's energy larger than the energy threshold $E_{IB} = \hbar\Omega_{IB}$. For example, the interband transition becomes significant around 650nm ($E_{IB} \sim 2\text{eV}$) for gold and 300nm ($E_{IB} \sim 4\text{eV}$) for silver [9].

In conclusion, loss in metals is an unavoidable process, that can affect the performance of metallic devices in applications that ask for high efficiency of emissions such as single-photon light sources, solar cells, or sensing. However, the generation of the hot carriers assisted absorption can be harvested for productive purposes such as acceleration of chemical reactions [25, 26].

1.2 Surface plasmon polaritons at a single interface

Above we have considered the optical response of bulk metals, noticing that the bulk plasmons (only exist at $\varepsilon(\omega_p)=0$) are naturally longitudinal waves that cannot be excited to the transverse field of light. However, when it comes to a dielectric/metallic interface, the light

waves can couple to the conductive electrons forming a hybrid surface mode. In this interaction, the free electrons near the surface oscillate collectively in resonance with the light wave, which are termed *surface plasmon polaritons* (SPPs) reflecting their hybrid nature. The SPPs are confined below the diffraction limit in the direction perpendicular to the interface while propagating in a long distance of micrometric scale along the surface). This fascinating characteristic of SPPs was first highlighted by Wood in 1902 [27].

The aim of this section is therefore to characterize the SPPs in terms of their dispersion relation (i.e., the frequency-dependent surface plasmon wavevector) and spatial profile, starting by identifying the conditions from which the surface plasmon modes can exist. These can be deduced by solving Maxwell's equations under the appropriate boundary conditions at the interface.



Figure 1.5: **Schematic representation of a surface plasmon propagating along the dielectric interface/metal.** ϵ_d and $\epsilon_m(\omega)$ are the relative dielectric function of the dielectric and metal, respectively.

We consider a simple geometry that can support SPPs: a flat dielectric/metal interface, as schematized in Figure 1.5. A dielectric of negligible with positive dielectric constant $\epsilon_d > 0$ is located in $z > 0$ and a metal with a complex dielectric function $\epsilon_m(\omega)$ is located in $z < 0$. The interface is set in a plane at $z = 0$. We simplify the problem to one-dimension surface wave, i.e., the waves propagate along the x-axis ($\partial/\partial x = ik_{\parallel}$), and no spatial variation in the y-axis ($\partial/\partial y = 0$). Here, $k_{\parallel} = \sqrt{k_x^2 + k_y^2}$ is the in-plane wavevector, which is necessarily conserved across the interface and therefore

$$k_{\parallel}^2 + k_{j,z}^2 = \epsilon_j k_0^2 \quad (1.8)$$

where $j = d, m$ denotes for the dielectric and metal media, k_j , z is normal component of the wavevector and k_0 is the wavevector of light in the vacuum.

Conditions to sustain SPPs at the interface

In order to find the condition that excitation can couple to SPPs, we seek the solutions of the Maxwell's equations for a homogeneous medium in the absence of the external charges and current density, yielding to the wave equation of the electric field [7]:

$$\nabla^2 \vec{E}_j + k_0^2 \varepsilon_j \vec{E}_j = 0 \quad (1.9)$$

Naturally, a similar equation exists for the magnetic field \vec{H}

we derive the fields in tow sets of polarization: transverse magnetic mode (p-polarization) and transverse electric mode (s-polarization), and then apply the boundary conditions at the interface.

- *s-polarization excitation*: only components H_x , H_z , and E_y are nonzero.

The electric and magnetic fields in each half-space medium can be expressed for s-polarization as

$$\vec{E}_j = e^{-i(\omega t - k_{\parallel} x)} e^{ik_{j,z} z} E_{j,y} \vec{e}_y, \quad \vec{H}_j = e^{-i(\omega t - k_{\parallel} x)} e^{ik_{j,z} z} (H_{j,x} \vec{e}_x + H_{j,z} \vec{e}_z) \quad (1.10)$$

The one-dimension propagating surface wave problem allows to simplify the Maxwell equation $\nabla \times \vec{E} = -\frac{\partial \vec{B}}{\partial t}$ into- the relation $\frac{\partial E_y}{\partial z} = -i\omega \mu_0 H_x$. On the other hand, the continuity at the interface of the in-plane components of the electric and magnetic fields requires:

$$E_{d,y}|_{z=0} = E_{m,y}|_{z=0}, \quad \frac{\partial E_{d,y}}{\partial z}|_{z=0} = \frac{\partial E_{m,y}}{\partial z}|_{z=0} \quad (1.11)$$

which are respectively equivalent to conditions

$$E_{d,y} = E_{m,y}, \quad k_{d,z} E_{d,y} = k_{m,z} E_{m,y} \quad (1.12)$$

These conditions are not fulfilled, excepted for $E_{d,y} = E_{m,y} = 0$. Therefore, the surface plasmon at the interface cannot be excited by the s-polarization

- *p-polarization excitation*: only components E_x , E_z , and H_y are nonzero. The electric and magnetic fields in each half-space medium can be expressed for the p-polarization as

$$\vec{E}_j = e^{-i(\omega t - k_{||}x)} e^{ik_{j,z}z} (E_{j,x}\vec{e}_x + E_{j,z}\vec{e}_z), \quad \vec{H}_j = e^{-i(\omega t - k_{||}x)} e^{ik_{j,z}z} H_{j,y}\vec{e}_y \quad (1.13)$$

In the absence of the external charges in each medium, we have $\nabla \cdot \vec{D} = 0$: $k_{||}E_{j,x} + k_{j,z}E_{j,z} = 0$. On the other hand, the continuity of the in-plane component of \vec{E} and normal component of \vec{D} imposes two boundary conditions at $z = 0$: $E_{d,x} = E_{m,x}$ and $\varepsilon_d E_{d,z} = \varepsilon_m E_{m,z}$. Combining these three equations, we obtain the final condition for the p-polarization excitation

$$\frac{k_{d,z}}{\varepsilon_d} = \frac{k_{m,z}}{\varepsilon_m} \quad (1.14)$$

This condition can be fulfilled by the two media have opposite signs of their relative permittivity such as dielectric/metal or dielectric/doped semiconductor. In terms of the excitation, we can conclude that the SPPs at the interface are essential to be excited by the p-polarization.

Dispersion relation of surface plasmon polaritons

By introducing the relation 1.14 into the equation $k_{||}^2 + k_{j,z}^2 = \varepsilon_j k_0^2$, we can obtain the dispersion relation of SPPs, which is expressed by a function

$$k_{SPP} = \frac{\omega}{c} \sqrt{\frac{\varepsilon_d \varepsilon_m}{\varepsilon_d + \varepsilon_m}} \quad (1.15)$$

For limit of low damping (implying $Im(\varepsilon_m) = 0$), we can plot the dispersion relation between angular frequency ω and the real part of $k_{||}$, as shown in Figure. We can see that for small $k_{||}$ corresponding to low frequencies (wavelength in mid-infrared and higher), the dispersion curve of SPPs is close to the respective light line of the dielectric $\omega = \frac{c}{\sqrt{\varepsilon_d}} k_0$. When $k_{||}$ increases, the SPPs dispersion is more separated from the light line and it asymptotes to a frequency $\omega_{SP} = \frac{\omega_p}{\sqrt{1+\varepsilon_d}}$ as $k_{||} \rightarrow \infty$. The ω_{SP} is called the *surface plasmon frequency*. Besides, the SPP dispersion is nearly flat for very large $k_{||}$, the group velocity is thus $v_g = \partial\omega/\partial k \rightarrow 0$, which means that the photons are dragged to be slowdown at the interface and the mode

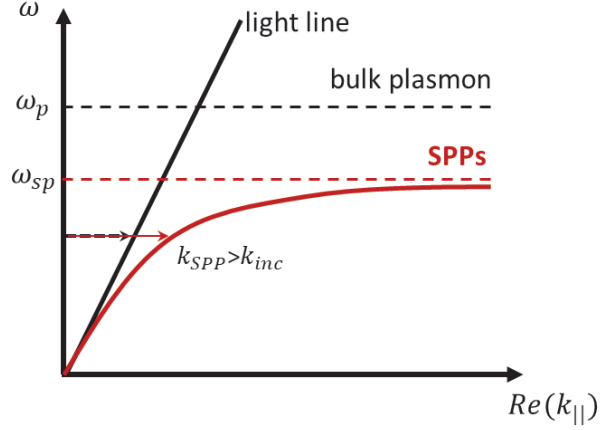


Figure 1.6: **SPP dispersion relation.** The dispersion of SPP (red curve) is below the light cone, i.e., the propagating regimes, of the light line (black line).

thus acquires electrostatic character [7].

The most important feature of the SP dispersion relation is that for a given frequency, the dispersion curve of SPPs is always under the respective light line of the dielectric. In other words, the momentum of the SPPs $\hbar k_{SPP}$ is always greater than that of a free-space photon at the same energy, $\hbar k_{inc}$ (k_{inc} is the free-space wavevector). This implies that the SPPs at the interface cannot be directly excited from free-space waves of the corresponding dielectric medium. Instead, special phase-matching techniques are required to provide additional momentum if the light is to be used to generate SPPs. There are three common optical techniques have been used to increase the momentum: (i) prism coupling [28, 29], (ii) grating coupling [30] (periodic configuration is patterned in the metal's surface), or (iii) near-field coupling induced by local scatters (i.e., particle or holes) [31, 32]. In this work, the techniques used for the excitation of SPPs will be discussed in more detail in Chapter 3.

Propagation length of SPPs

Owing to the losses arising from the absorption of the metals, the SPPs are gradually damped during propagating over the interface. The attenuation of the plasmon intensity along the x-axis is linked to imaginary part of k_{SPP} as

$$I_{SPP} = I_0 e^{-2\text{Im}(k_{SPP})x} \quad (1.16)$$

The propagation length is thus defined as the distance at which the plasmon intensity decayed

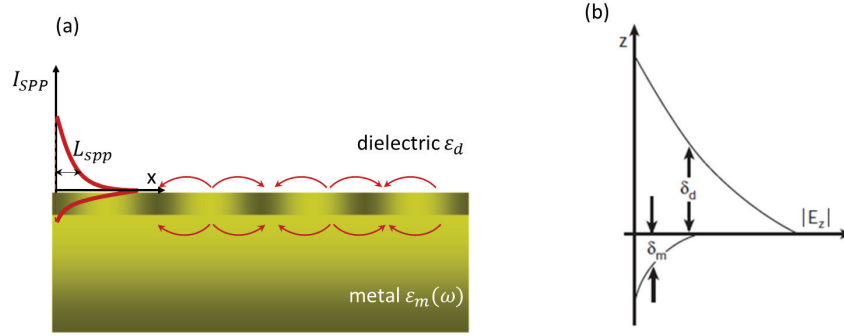


Figure 1.7: **Propagation of SPPs** (a) attenuation of plasmon intensity along the surface and (b) evanescence of field inside the media along the perpendicular z -direction.

to $1/e$ of its initial value (see Figure 1.7a) and can be given by

$$L_{SPP} = \frac{1}{2\text{Im}(k_{SPP})} \quad (1.17)$$

Here, the imaginary part of k_{SPP} can be calculated by introduce the complex $\varepsilon_m(\omega)$ of metals into equation 1.15. Therefore, the propagation length of SPPs is mainly dictated by the loss in metals which is responsible by the imaginary part of its permittivity. For example, in the visible regime, the smooth surface of silver can support long propagation lengths in the range of $10\text{-}100\mu\text{m}$ due to its low losses, which is 1 order of magnitude greater than relative absorbing metal such as aluminium [33].

In terms of time domain, we also can define the decay time of SPPs as $\tau_{SPP} = \frac{L_{SPP}}{v_g} = \frac{2\pi}{\omega_{SPP}}$, with ω_{SPP} is the imaginary part of the SPP frequency, which can be deduced from the complex k_{SPP} . The decay time of a dielectric/metal interface is usually in the order of $10\text{-}100\text{fs}$ [34, 35], which can propel their use in various applications.

Extension of field inside the media

The characteristic of the surface waves requires the electric field to be strongly confined near the surface and evanescent decay perpendicularly away from it, which is expressed by the term $e^{-|k_{j,z}||z|}$ in the field equation. The reciprocal values $\delta_j = 1/|k_{j,z}|$, which corresponds to the z -distance at which $|E_z|$ decayed by $1/E$ (see Figure 1.7b), can determine the spatial extension or the confinement of the fields perpendicular to the surface. This is so-called evanescent decay length.

From the conversion relation of the in-plane wavevector $k_{\parallel}^2 + k_{j,z}^2 = \varepsilon_j k_0^2$, we can deduce the decay lengths of SPPs inside the dielectric and respectively are:

$$\begin{aligned}\delta_d &= \frac{\lambda}{2\pi} \sqrt{\frac{|\varepsilon_d + \text{Re}(\varepsilon_m)|}{\varepsilon_d^2}} \\ \delta_m &= \frac{\lambda}{2\pi} \sqrt{\frac{|\varepsilon_d + \text{Re}(\varepsilon_m)|}{\varepsilon_m^2}}\end{aligned}\tag{1.18}$$

Because of $|\varepsilon_m| > |\varepsilon_d|$, the field penetrates more inside the dielectric half-space. Typically, the decay length δ_d into the dielectric is in the order of half wavelength, whereas the decay length into metal is associated with the skin depth at room temperature $\delta_m \sim 25nm$. [7].

1.3 Plasmon hybridization in planar structures

In the previous section, we have seen that a single dielectric/ metal interface can support surface plasmon which propagates along the interface while remains confined with a perpendicular component field near the surface. When the SPPs from two individual interfaces are brought near together (separated distance should be smaller than attenuation length of SPPs δ inside the overlapping medium), they can couple and results in hybrid plasmon modes. Typically, the planar structures that support the hybrid plasmon modes are based on two fundamental structures: (i) insulator-metal-insulator (IMI) layers or (ii) metal-insulator-metal (MIM) layers. The goal of this section is therefore to show how the SPPs of each single interface interact and to give the main characteristics of the new modes that arise from the SPPs coupling.

We consider three-layer structures consisting of a thin slab of thickness t sandwiched between two infinite cladding made from the same material, as shown in Figure 1.8. The relative dielectric functions of the cladding and slab respectively are ε_s and ε_c , which necessarily have opposite signs in order to support SPPs. Depending on the structure, the cladding is made from metal, and the slab is made from a dielectric (MIM structure) or vice versa (IMI structure).

The geometry of the three-layer system in Figure 1.8 is analog to a waveguide, which

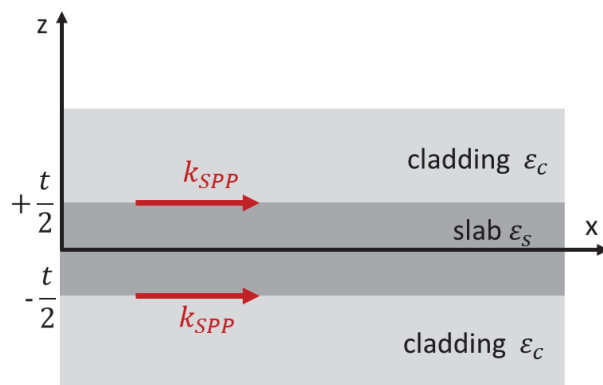


Figure 1.8: **Schematic of a three-layer system that supports hybridization of SPPs** A thin slab of dielectric function ε_s and thickness t is embedded between two similar cladding media of dielectric function ε_c .

might exhibit oscillatory modes for the sufficient thickness of the slab. Here we are only interested in the lowest-order bound modes. The electric and magnetic field components of the p-polarization that are non-oscillatory in the z -direction and propagate along the x -direction are written as

$$\begin{aligned} E_x &= E_x^0(z)e^{-i(\omega t - k_{||}x)}, & E_z &= E_z^0(z)e^{-i(\omega t - k_{||}x)} \\ H_y &= H_y^0(z)e^{-i(\omega t - k_{||}x)} \end{aligned} \quad (1.19)$$

Here, $k_{||}^2 = k_{j,z}^2 + \varepsilon_j k_0^2$ is the in-plane component of wavevector, k_z is the associated normal component; $j = s, c$ denotes for the slab and cladding media. From the boundary conditions that require H_y and E_x at upper and lower interfaces ($z = \pm \frac{t}{2}$) are continuous, two dispersion relations and associated field components can be given by solutions of

$$\tanh(k_{s,z} \frac{t}{2}) = -\frac{k_{c,z} \varepsilon_s}{k_{s,z} \varepsilon_c}, \quad E_z^0(z) = E_z^0(-z) \propto \frac{k_{||}}{\omega \varepsilon_s} \cosh(k_{s,z} z) \quad (1.20)$$

$$\tanh(k_{s,z} \frac{t}{2}) = -\frac{k_{s,z} \varepsilon_c}{k_{c,z} \varepsilon_s}, \quad E_z^0(z) = -E_z^0(-z) \propto \frac{k_{||}}{\omega \varepsilon_s} \sinh(k_{s,z} z) \quad (1.21)$$

For the solutions of equation 1.20, the field component $E_z(z)$ is an even function that exhibits a symmetry profile along the z -axis. On the contrary, for the solutions of equation 1.21, the $E_z(z)$ is an odd function and the field profile is anti-symmetric along the z -axis. Respectively, they are called symmetric mode and anti-symmetric mode. Now we can apply

these dispersion relations to describe the coupled SPP modes of IMI and MIM structures.

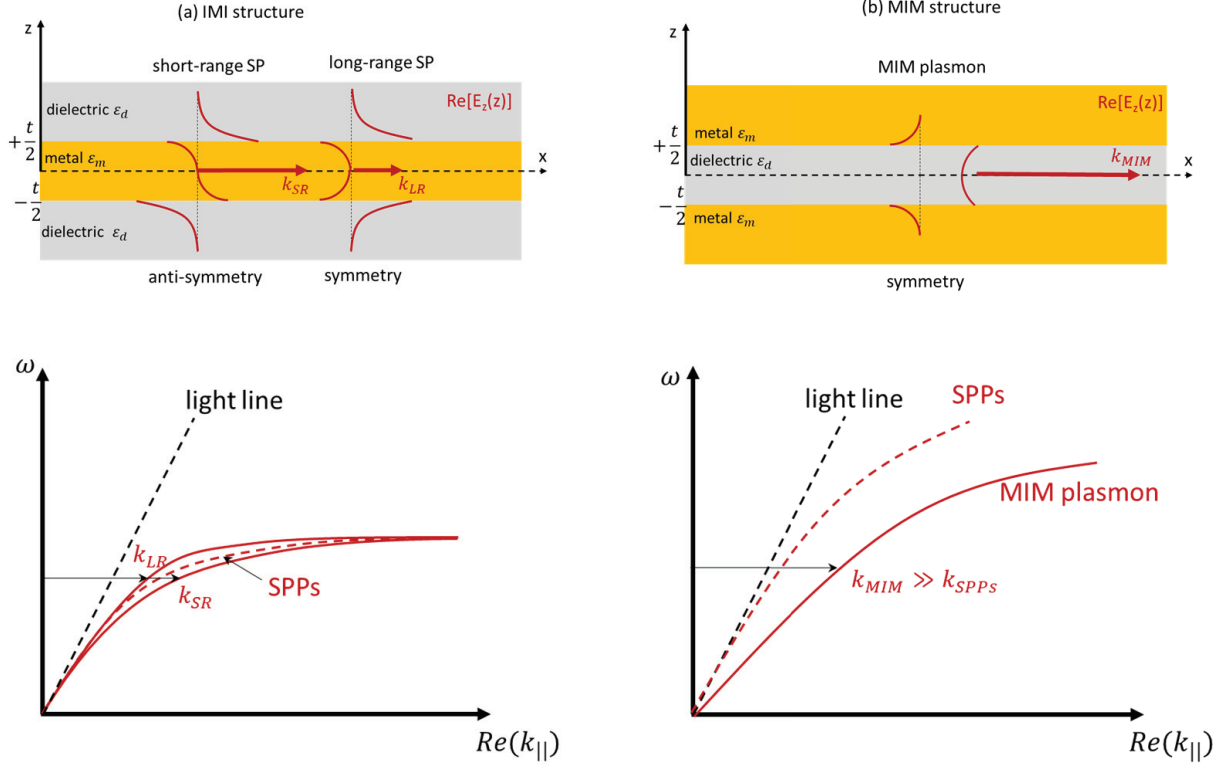


Figure 1.9: **Plasmon hybrid modes in the IMI and MIM structure.** Spatial profile of the field component $Re[E_z(z)]$ and dispersion relations of the coupled SPPs in (a) IMI structure and (b) MIM structure. Adapted from P.Berini 2006 [36]

In the IMI structure, SPPs on either side of the metal slab can hybridize, resulting in E_z -symmetric and anti-symmetric modes, Figure 1.9a illustrates the field profile and the associated dispersion relation of the hybrid mode of the IMI structure. Here, the spacing between two dispersion curves depends on the thickness of the metallic slab. For a large slab thickness, the surface plasmon of each interface barely interact and the dispersion of two hybrid modes can converge into the single SPP dispersion. The hybridization can take place when the individual SPPs overlap and become significant when the metal thickness is smaller than its skin depth ($t < 20\text{nm}$) [6]. At a given frequency, the in-plane wavevector $k_{||}$ of the anti-symmetric mode (k_{SR}) is always greater than that of the symmetric mode (k_{LR}). In the other words, the anti-symmetric mode has tighter confinement inside the slab than the symmetric one. This also can be seen by an examination of the component field. As the slab thickness vanishes, while the anti-symmetric mode increases its confinement due

to the field null inside the metal, the symmetric mode evolves into a plane wave supported by the surrounding homogeneous dielectric. Since the better confinement implies a lower propagation length, the anti-symmetric mode is called *short-range surface plasmon* (SRSP) and the symmetric mode is called *long-range surface plasmon* (LRSP). Depending on the wavelength or the materials considered, the propagation length of the LRSP can take place in the order of a few hundred micrometers [37]. Therefore, the LRSP in the IMI structure can be employed to assist the information or energy over a long distance.

For the MIM geometry, the SPPs on either side of the dielectric medium similarly hybridize inside the slab, as shown in Figure 1.9b. However, for the insulator thicknesses of interest, only the fundamental symmetric mode (or long-range plasmon) is supported that has no cut-off for vanishing slab thickness, unlike the anti-symmetric mode that is cut-off at roughly $\lambda/2$ [38]. We refer to the symmetric mode of this structure as the MIM plasmon gap mode. The most striking feature of the MIM plasmon gap is that it has a very large $k_{||}$, usually in the 1 order of magnitude as compared to the SPP at a single interface, which can be achieved even for excitation well below surface plasmon frequency. Therefore, the metallic nanostructures based on the MIM geometry are a platform for deep-subwavelength confinement of light with mode volumes smaller than $\sim 10^{-6}(\lambda/n)^3$ [38, 22].

To conclude, we have shown that the hybridization of SPPs in the planar system allows extending the properties of the individual SPPs in the terms of propagation length and light confinement. Further investigation of these two structures will be done by the analytical calculation in Chapters 2 and 5.

1.4 Localized surface plasmon of metallic nanoparticles

Previously, we have seen that the light can couple to electron plasma of metal at a planar dielectric/metal interface, yielding propagating surface plasmon. In this section, we will see that when the interface is reduced into nanoscale dimension of the metallic particle, the free electron cloud can oscillate resonantly with electromagnetic field, resulting in non-propagating surface plasmon. This resonance is called the *localized surface plasmon* resonance (LSPR). We will begin with an overview problem of optical responses, including scattering,

absorption and extinction, of an arbitrary object. Then, appropriate analytical treatments will be discussed, depending on the size of the particle, to show how this give raise to the phenomenon of the LSPR.

1.4.1 Scattering, absorption and extinction

Generally, when light interacts with an object, it can be scattered or absorbed by the object. While absorption corresponds to the energy dissipation (heating) in the object, scattering is an elastic interaction, i.e. the object re-emits the electromagnetic field without changing the wavelength. The total energy that an object takes from the incident light, thus it is attributed to scattering and absorption, is called extinction. Usually, these optical responses of the object are characterized by optical cross-sections. This section aims to define these optical cross-sections. Let us consider a general situation where an arbitrary scatter object of relative permittivity $\varepsilon(\omega)$ with a finite size is surrounded by a homogeneous transparent medium and is excited by an incoming plane wave \vec{E}_{inc} , as shown in Figure 1.8.

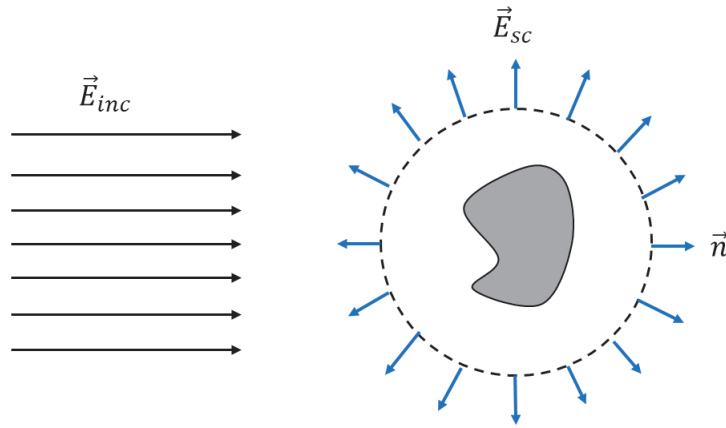


Figure 1.10: **Schematic diagram of optical responses of an arbitrary particle under the plane wave excitation.** The dotted ring presents an imaginary surface with surface normal vector \vec{n} , which may be used to calculate the energy flux in the far field.

Scattering cross-section

It is clear that not all the photons but only a finite number of photons of the incoming light are scattered by the object. Therefore, the probability that leads to the scattering is proportional to an effective area, so-called scattering cross-section. The scattering cross-

section is defined as the ratio between the average scattered power P_{sc} and the intensity of the incident field I_{inc}

$$\sigma_{sc} = \frac{P_{sc}}{I_{inc}} = \frac{1}{|\langle \vec{S}_{inc} \rangle|} \iint_A \langle \vec{S}_{sc} \rangle \cdot \vec{n} dA \quad (1.22)$$

where $\langle \vec{S}_{inc} \rangle$ and $\langle \vec{S}_{sc} \rangle$ respectively are the time-average Poynting vector of the incident and scattered field. Here, the EM energy flux of scattering through an imaginary surface A far from the object (Figure 1.8) can be calculated as $P_{sc} = \iint_A \langle \vec{S}_{sc} \rangle \cdot \vec{n} dA$, with \vec{n} is an outward-facing normal vector. It is important to note that the scattering cross-section has unit of area but it does not represent a geometrical cross-section of the object. Instead, the physical meaning of scattering cross-section is related to the energy of the incident light that has been lost in scattering.

Absorption cross-section

Since the object has a permittivity, it can be considered as a perturbation of the background medium [39]. Therefore, the total fields around the object can be represented as a sum of the incident fields and scattered fields:

$$\begin{aligned} \vec{E}_{tot} &= \vec{E}_{inc} + \vec{E}_{sc} \\ \vec{H}_{tot} &= \vec{H}_{inc} + \vec{H}_{sc} \end{aligned} \quad (1.23)$$

As the medium is non-absorbing, the total EM energy flux inward the imaginary surface around the object will be equal to the absorbed power

$$P_{abs} = - \iint_A \langle \vec{S}_{tot} \rangle \cdot \vec{n} dA \quad (1.24)$$

The minus thus said that the direction of the time-averaged Poynting vector of the total field $\langle \vec{S}_{tot} \rangle$ (inward) is opposite to \vec{n} (outward). In the analogy to scattering, we can define absorption cross-section as

$$\sigma_{abs} = \frac{P_{abs}}{I_{inc}} = - \frac{1}{|\langle \vec{S}_{inc} \rangle|} \iint_A \langle \vec{S}_{tot} \rangle \cdot \vec{n} dA \quad (1.25)$$

Extinction cross-section

The time-averaged Poynting vector of the total field $\langle \vec{S}_{tot} \rangle$ can be formulated as a function

of the fields as

$$\begin{aligned}
 \langle \vec{S}_{tot} \rangle &= \frac{1}{2} Re(\vec{E}_{tot} \times \vec{H}_{tot}^*) \\
 &= \underbrace{\frac{1}{2} Re(\vec{E}_{inc} \times \vec{H}_{inc}^*)}_{\langle \vec{S}_{inc} \rangle} + \underbrace{\frac{1}{2} Re(\vec{E}_{sc} \times \vec{H}_{sc}^*)}_{\langle \vec{S}_{sc} \rangle} + \underbrace{\frac{1}{2} Re(\vec{E}_{inc} \times \vec{H}_{sc}^* + \vec{E}_{sc} \times \vec{H}_{inc}^*)}_{?}
 \end{aligned} \quad (1.26)$$

Here, the first and second terms of equation 1.26 are equal to the time-averaged Poynting vectors of incident and scattered fields $\langle \vec{S}_{inc} \rangle$ and $\langle \vec{S}_{sc} \rangle$, respectively. We now want to find the physical meaning of the last cross term. Applying the area integration for both sides of equation 1.26, we have

$$\begin{aligned}
 \iint_A \langle \vec{S}_{tot} \rangle \cdot \vec{n} dA &= \iint_A \langle \vec{S}_{inc} \rangle \cdot \vec{n} dA + \iint_A \langle \vec{S}_{sc} \rangle \cdot \vec{n} dA + \iint_A \frac{1}{2} Re(\vec{E}_{inc} \times \vec{H}_{sc}^* + \vec{E}_{sc} \times \vec{H}_{inc}^*) \cdot \vec{n} dA \\
 -P_{abs} = 0 + P_{sc} + \iint_A \frac{1}{2} Re(\vec{E}_{inc} \times \vec{H}_{sc}^* + \vec{E}_{sc} \times \vec{H}_{inc}^*) \cdot \vec{n} dA
 \end{aligned} \quad (1.27)$$

Here $\iint_A \langle \vec{S}_{inc} \rangle \cdot \vec{n} dA = 0$ is the result of the conservation of the incoming and out-coming energies through the imaginary surface. We can express the cross term as

$$- \iint_A \frac{1}{2} Re(\vec{E}_{inc} \times \vec{H}_{sc}^* + \vec{E}_{sc} \times \vec{H}_{inc}^*) \cdot \vec{n} dA = P_{sc} + P_{abs} = P_{ext} \quad (1.28)$$

which as shown, is equal to the sum of the scattered power and the absorbed power. Therefore this term is extinct power $P_{ext} = P_{sc} + P_{abs}$, which tells that the object can take some energy from the incoming field and then distributes it into scattering and absorption. The energy that the incident field has lost is called extinction. Besides, from equation 1.28, we can interpret the extinction as an interference between the incident and scattered fields. Now, we can formulate the extinction cross-section as

$$\sigma_{ext} = \frac{P_{ext}}{I_{inc}} = \frac{1}{|\langle \vec{S}_{inc} \rangle|} \iint_A \frac{1}{2} Re(\vec{E}_{inc} \times \vec{H}_{sc}^* + \vec{E}_{sc} \times \vec{H}_{inc}^*) \cdot \vec{n} dA \quad (1.29)$$

Subsequently, we also have $\sigma_{ext} = \sigma_{sc} + \sigma_{abs}$.

For numerical calculation: The absorption cross-section can be calculated by applying the Poynting's theorem for the harmonic field in a homogeneous medium $\nabla \cdot (\vec{E}_{tot} \times \vec{H}_{tot}^*) =$

$-\vec{j}^* \cdot \vec{E}_{tot}$, with \vec{j} is the current density that the incident field induces in the particle. Making a volume integration of this equation yields to the absorbed power

$$P_{abs} = \frac{1}{2} \iiint_V \text{Re}(\vec{j}^* \cdot \vec{E}_{tot}) dV \quad (1.30)$$

Similarly, we also can express the extincted power in the term of volume integral of the current density by applying the reciprocity theorem $\nabla \cdot (\vec{E}_{inc} \times \vec{H}_{sc}^* + \vec{E}_{sc} \times \vec{H}_{inc}^*) = -\vec{j}^* \cdot \vec{E}_{inc}$, we obtain

$$P_{ext} = \frac{1}{2} \iiint_V \text{Re}(\vec{j}^* \cdot \vec{E}_{inc}) dV \quad (1.31)$$

The two expressions 1.30 and 1.31 of the powers of absorption and extinction would be very useful for numerical calculations.

Optical responses of metallic nanoparticles: Problem with size

Now we will use the optical cross-sections discussed above to characterize the optical response of metallic nanoparticles. Roughly, because of the small dimension, the EM field can penetrate significantly inside the nanoparticles, however, the penetration can be different depending on the particle's size. Figure 1.11 considers two spherical metallic nanoparticles of different radii, which are surrounded by a non-absorbing medium and submitted to an incident field.

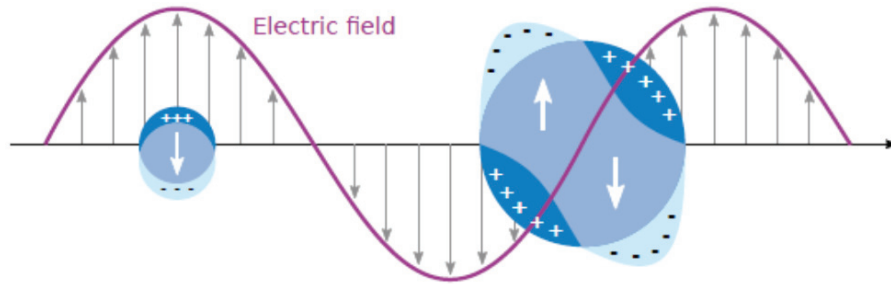


Figure 1.11: **Schematic diagram of optical responses of an arbitrary metallic particle under the plane wave excitation.** Depending on the particle's size, the external field induce a dipole or multipole in the particles. Source: PhD thesis of [5]

For a vanishing small particle of diameter is much smaller than the wavelength of light in the surrounding medium ($a \ll \lambda$), the field is homogeneous over the particle volume. Therefore, the oscillating EM field can be simplified to an electrostatic field and the optical

responses of the small particle now can be analyzed using the quasi-static approximation.

On the other hand, for a large particle of diameter in the order of wavelength ($a \sim \lambda$), it can feel the spatial variation of the field, resulting in a more complex surface charge distribution. In this case, a rigorous theory is required to study the optical responses of the particle. This theory was developed completely by Mie in 1908 [40]. The discussion in the following sections will be separated based on the two regimes of the particle's dimension.

1.4.2 Quasi-static approximation

In this section, we aim to consider the interaction of EM waves with a small metallic nanoparticle of characteristic dimension is much smaller than the wavelength. Using the quasi-static approximation, we will see that the absorption and scattering cross-sections can be resonantly enhanced at the LSPR.

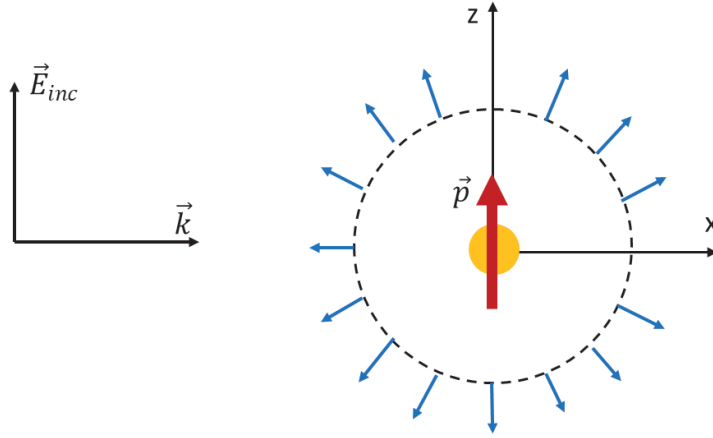


Figure 1.12: **Schematic diagram of a small spherical metallic nanoparticle subjected to an EM plane wave.** The particle of radius $a \ll \lambda$ is approximated to a dipole of moment \vec{p} .

We consider the most convenient geometry for an analytical treatment: a spherical particle of the radius $a \ll \lambda$ is submitted to a plane-wave illumination $\vec{E}_{inc}(x, t) = E_0 e^{-i(\omega t - kx)} \cdot \vec{e}_z$, surrounding by an isotropic, non-absorbing medium with dielectric constant ε_d . The dielectric function of the particle in response to the applied field is described by a complex number $\varepsilon_m(\omega)$. The sketch of the situation is illustrated in Figure 1.12.

The strategy to find $\varepsilon_m(\omega)$ is first solving the Laplace equation in the absence of free

charges for potential $\nabla^2 V = 0$, from which we can calculate the electric field $\vec{E} = -\nabla V$ inside and outside the particle. The boundary conditions at the interface of the particle are also applied for both the potential and normal components of the displacement field. In the following, we will present the main results as the consequences of the quasi-static approximation:

Electrostatic field of excitation: the spatial variation of the incident field over the particle volume can be ignored. Therefore, the harmonically oscillating field can be simplified to an electrostatic field $E_{inc}(t) = E_0 e^{-i\omega t}$.

Induce dipole surface plasmon: free electron cloud of the metallic particle oscillates in response to the applied EM field, yielding an oscillating induced dipole of moment $\vec{p}(t) = \varepsilon_0 \varepsilon_d \alpha \vec{E}_{inc}$ with polarizability α can be given by:

$$\alpha = 4\pi a^3 \frac{\varepsilon_m(\omega) - \varepsilon_d}{\varepsilon_m(\omega) + 2\varepsilon_d} \quad (1.32)$$

We can see that the polarizability α of the particle is resonantly enhanced at the vanishing of $\varepsilon_m(\omega) + 2\varepsilon_d$. For the case of small $Im[\varepsilon_m(\omega)]$, the resonance condition simplifies to $Re[\varepsilon_m(\omega)] = -2\varepsilon_d$. For particles made from Drude metal with dielectric function negligible damping $Re[\varepsilon_m(\omega)] \approx 1 - \omega_p^2/\omega^2$, the value of α can approach maximum at a frequency

$$\omega_{LSPR} \approx \frac{\omega_p}{\sqrt{\varepsilon_m(\omega) + 2\varepsilon_d}} \quad (1.33)$$

When the frequency of the applied field is ω_{LSPR} , the electron cloud in the metallic nanoparticle oscillates collectively and results in resonance that enhances the polarizability. This resonance is called the localized surface plasmon that can appear in the optical spectra. We can see that the resonance frequency ω_{LSPR} depends on the dielectric function of the environment ε_d , which makes metallic nanoparticles employed for optical sensing. Besides, ω_{LSPR} is not affected by the particle's size as a consequence of the quasi-static approximation.

Field enhancement: As a consequence of the quasi-static approximation, if we look at the particle from the outside, we could see it as a dipole located in the electrostatic field. Therefore, a total field outside the particle can be interpreted as a superposition of the incident field and the near field of the dipole ($kr \ll 1$), where its electric field is $\sim 1/r^3$.

The electric field outside the particle can be determined from the associated potentials via $\vec{E} = -\nabla V(\vec{r})$ and is formulated as

$$\vec{E}_{out} = \vec{E}_0 + \frac{3\vec{e}_r(\vec{e}_r \cdot \vec{p}) - \vec{p}}{4\pi\epsilon_0\epsilon_d} \cdot \frac{1}{r^3} \quad (1.34)$$

Here we see that the resonance in α at ω_{LSPR} also implies resonant enhancement in the dipolar field. For example, if we consider the \vec{E}_{out} on the surface of a particle $r = a$ and at around the induced dipolar axis (i.e., \vec{E}_{out} is strongest), we can obtain a maximum field enhancement at resonance ($Re[\epsilon_m(\omega)] = -2\epsilon_d$) as

$$\frac{E_{res}}{E_0} \approx 1 + \frac{3Re[\epsilon_m(\omega)]}{Im[\epsilon_m(\omega)]} \quad (1.35)$$

For example, if we take a gold nanoparticle illuminated by $\lambda = 650\text{nm}$ which has $\epsilon_m = -11 + 1i$ [11], the field at the poles along the axis of dipolar surface plasmon enhances by ~ 30 times as compared to the field E_0 of the surrounding medium. Since the resonance is also associated with the field enhancement, the metallic particle can act as a local refractive index sensor, which is the most sensitive within the near-field region of order 10-50nm.

Optical cross-section enhancement: As the particle is approximated to a dipole, its scattered power P_{sc} can be calculated from the Poynting vector associated with its far-field radiation, i.e., retaining only the term $1/r$ of the dipole field [39]. For the absorption, the mean power absorbed by the particle is responsible by the imaginary part of the polarizability α via expression $P_{abs} = \frac{1}{2}E_0^2\omega\epsilon_d Im(\alpha)$. On the other hand, the particle is subjected to an incident plane wave, which has an average incident irradiance $I_{inc} = \frac{1}{2}\sqrt{\epsilon_d}cE_0^2$. Recalling the definition of the scattering and absorption cross-sections in equations 1.22 and 1.25, respectively, we obtain

$$\begin{aligned} \sigma_{sc} &= \frac{P_{sc}}{I_{inc}} = \frac{1}{6\pi}\epsilon_d^2\left(\frac{2\pi}{\lambda}\right)^4|\alpha|^2 \\ \sigma_{abs} &= \frac{P_{abs}}{I_{inc}} = \sqrt{\epsilon_d}\left(\frac{2\pi}{\lambda}\right)Im(\alpha) \end{aligned} \quad (1.36)$$

Besides, from the scattered far-field of the dipole, we can determine the interference with the incident field, from which the extinction cross-section can be calculated [40], resulting in

$$\sigma_{ext} \approx \sigma_{abs}.$$

The dependence of the optical cross-sections on the polarizability α implies that they exhibit the same resonance condition at LSPR frequency ω_{LSPR} . Noticing that α scales with a^3 (equation 1.32) or V , with v is the volume of the spherical particle, we can see that $\sigma_{sc} \sim V^2$ and $\sigma_{ext} = \sigma_{abs} \sim V$. When the size of the particle decreases, it is clear that the extinction is dominated by absorption. In the other words, the small plasmonic particles are good absorbers and bad scatters. Besides, the σ_{sc} is proportional to $1/\lambda^4$, which corresponds to the Rayleigh scattering.

1.4.3 Mie theory

We have shown that the resonantly absorbing and scattering light field of vanishingly small particles is well-predicted by the quasi-static approximation. In response to the EM field that approximates constant throughout the particle, the electrons oscillate collectively respected to the fixed ion, forming a dipolar mode. However, for a particle of dimensions in the order of wavelength, it feels the inhomogeneous spatial variation of the driving field. A more complex surface charge distribution encloses the particle, which can induce multipolar modes. In this situation, the dipolar or quasi-static approximation is no longer valid, and a rigorous electrodynamic treatment is required. Mie in 1908 developed a complete theory that gives an appropriate analytic solution to scattering and absorption problems for a sphere of arbitrary radius embedded in a homogeneous non-absorbing medium.

A detailed description of the Mie theory can be found in the book of Bohren and Huffman [41]. Generally speaking, the theory still follows the main strategy of calculating the optical cross-sections of the object: applying the boundary conditions for fields inside and outside the particle, which are also necessarily satisfied Maxwell's equations. To address the higher-order modes, the field outside the particle, including incident and scattered fields, and the internal field are expanded into a series of the two basic vector functions \vec{M} and \vec{N} . These functions have all the required properties of an electromagnetic field in a homogeneous medium: solenoidal fields ($\nabla \cdot \vec{\psi} = 0$) and satisfy the vector Helmholtz wave equation ($\nabla^2 \vec{\psi} + k^2 \vec{\psi} = 0$), where $\vec{\psi}$ stands for electric field \vec{E} and magnetic field \vec{H} . Therefore, \vec{M} and \vec{N} are referred to the vector spherical harmonics, which can be constructed from the scalar function ψ in

spherical coordinates as

$$\begin{aligned}\vec{M} &= \nabla \times (\vec{r}\psi) \\ \vec{N} &= \frac{1}{k}(\nabla \times \vec{M})\end{aligned}\tag{1.37}$$

where \vec{r} is the radius vector. These expressions are necessary to satisfy the vector Helmholtz wave equation and the problem of finding solutions to the field equations can simplify the finding solutions to the scalar wave equation ψ . By resolving the scalar Helmholtz equation in the spherical coordinates, we can obtain solutions to a scalar function

$$\begin{aligned}\psi_{elm} &= P_l^m(\cos\theta)z_l(kr)\cos m\phi \\ \psi_{olm} &= P_l^m(\cos\theta)z_l(kr)\sin m\phi\end{aligned}\tag{1.38}$$

where notations e and o stand for even and odd due to the presence of cosine terms. The $P_l^m(\cos\theta)$ is associated with *Legendre polynomials*. The $z_l(kr)$ are the spherical *Bessel functions* of 1st, 2nd, or 3rd kind, each involves in the expansions of incident, internal, or scattered fields, depending on whether it either converges or diverges at the origin. Indices m and l are integers, $l \geq 1$ and $-l \leq m \leq +l$, which determine the form of each vector spherical harmonics \vec{M}_{lm} and \vec{N}_{lm} . Here, l corresponds to the order of polarity of the different resonant modes, e.g. dipolar ($l = 1$), quadrupolar ($l = 2$), and m is the azimuth number. The fields now can be developed to an arbitrary order from a linear combination of these basis functions.

Returning to the scattering and absorption problem, while the incident field is already known (e.g. plane wave), the expansions of the scattered field and the internal field contains four unknown coefficients. These expansion coefficients can be found by applying the boundary conditions at the interface of the sphere: the tangential components of the vector fields across the surface boundaries are preserved. Finally, the extinction and scattering cross-section can be derived by calculating the flux of the Poynting vector over an imaginary surface enclosing the particle. The extinction cross-section is expressed as

$$\begin{aligned}\sigma_{ext} &= \frac{1}{|\langle \vec{S}_{inc} \rangle|} \iint_A \frac{1}{2} \text{Re}(\vec{E}_{inc} \times \vec{H}_{sc}^* + \vec{E}_{sc} \times \vec{H}_{inc}^*) \cdot \vec{n} dA \\ \sigma_{ext} &= \frac{2\pi}{k^2} \sum_{l=1}^{\infty} (2l+1) \text{Re}(a_l + b_l)\end{aligned}\tag{1.39}$$

and scattering cross-section is given by

$$\sigma_{sc} = \frac{1}{|\langle \vec{S}_{inc} \rangle|} \iint_A \langle \vec{S}_{sc} \rangle \cdot \vec{n} dA$$

$$\sigma_{sc} = \frac{2\pi}{k^2} \sum_{l=1}^{\infty} (2l+1)(|a_l|^2 + |b_l|^2)$$
(1.40)

Here, the a_l and b_l are called Mie coefficients (the expressions can be found in [41]). The cross-section is given by the sum, this means that the energy scatters through independent modes corresponding to a_l and b_l , with l defining the order of the polarity of the modes. When the particle size is much smaller than the wavelength, the contribution of all modes beyond the lowest order may be negligible. The cross-sections remain only dipolar term, which recovers the quasi-static approximation with corrections.

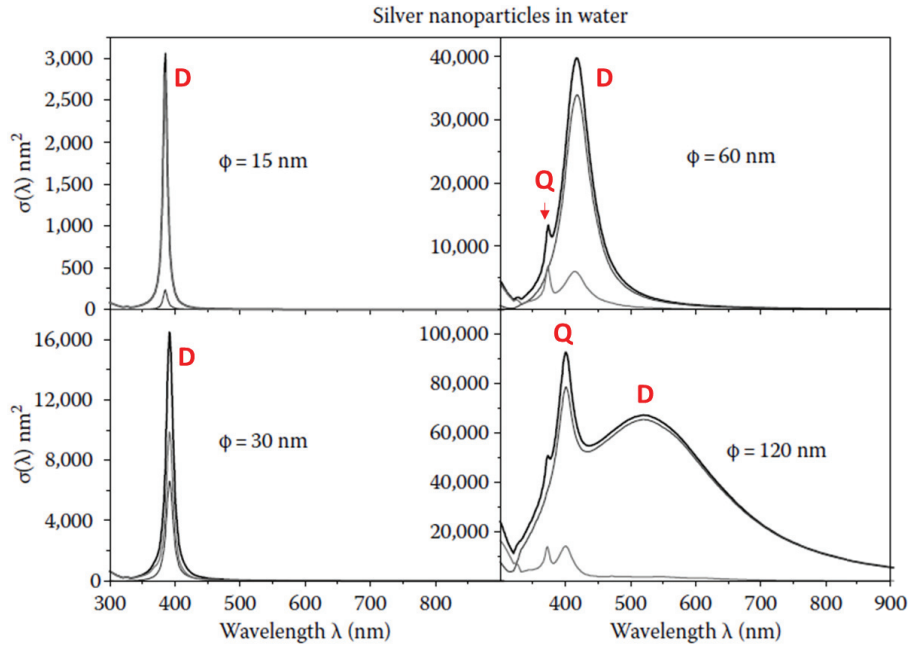


Figure 1.13: **Optical cross-sections of silver nanoparticles of various radii ϕ in water calculated by Mie theory.** Extinction is presented bold black line, absorption is presented in grey line, and scattering is shown in thin black line. Here, D labels for dipolar mode and Q labels for quadrupolar mode. Adapted from [9].

For example, the Figure 1.13 presents the results of the Mie theory for 4 silver spheres with radii of 15nm, 30nm, 60nm, and 120 nm, surrounded by water ($n = 1.33$) [9]. We can see that for small sizes, extinction is dominated by absorption and exhibits only the dipolar

mode. When the radius increases, the scattering contributes significantly to the extinction and the resonance is very different from the one expected in the quasi-static approximation: resonance of dipolar mode is red-shifted and quadrupolar mode appears at a lower wavelength.

The Mie theory can be applied to spherical core/shell structure and extended to several spherical nanoparticles in an interaction excited by an incident plane wave. For particles with shapes that cannot be approximated by spheres or ellipsoids, numerical methods are employed to calculate the optical cross-sections.

Chapter 2

Coupling a dipole to multilayer surface plasmon devices

Hybridization of surface plasmon in the multilayer structures allows for enhancing the performance of single-surface plasmons, such as extending the propagation length to around 1 order of magnitude or deep-subwavelength confinement of light. In this Chapter, we investigate numerically the surface plasmon hybridized inside the planar multilayer structure by employing a dipole as a probe. The first section will be dedicated to presenting how we can use the classical approach to study the spontaneous emission of a dipole. Then by calculating the spatial spectrum of the power dissipated by a buried inside the plasmonic structure, we can identify and construct the optical modes that are supported by the structure. Moreover, figures of merit were deduced, including the Purcell factor and coupling efficiency to each identified mode. We mainly focus our study on two multilayer structures: (i) a realistic insulator/metal/insulator (IMI) device and (ii) alternative N-stacks of metallic and insulator thin films. For the IMI device, we found that the structure can support many modes including the long-range surface plasmon of a few ten μm propagation length and waveguide modes. The coupling efficiency to the modes can be controlled by the position and orientation of the dipole. For the N-stack device, we show that when N is large, the plasmon modes evolve toward an energy continuum in a manner similar to the energy bands in a solid.

Contents

2.1 Spontaneous emission of an emitter	46
2.2 Spontaneous emission of a dipole near planar interfaces	51
2.3 Coupling a dipole to fundamental planar plasmonic structures	53
2.4 Coupling a single dipole to a long-range surface plasmon device	59
2.5 Surface plasmon hybridized dressed states	64

2.1 Spontaneous emission of an emitter

Quantum description: a two-level system

Proper treatment of the interaction of light and matter (molecules or other emitters) requires rigorous theoretical treatment of quantum electrodynamics (QED), in which both electronic states of an emitter and electromagnetic field are quantized. An emitter is described as a two-level system: ground state $|g\rangle$ of energy E_g and excited state $|e\rangle$ of energy E_e . Interacting with a quantized radiation field promotes electrons from the ground state to the excited state, subsequently relaxing into the fundamental level after a certain time, accompanied by the emission of a photon of energy $\hbar\omega_0 = E_e - E_g$. The spontaneous emission is thus defined as the emission of a photon by a system previously brought to an excited state and occurs independently of any external field. This process is schematized in Figure 2.1a.

As the relaxation is spontaneous, the probability that the recombination takes place is an exponential decrease of time $e^{-\Gamma t}$, with Γ being the decay rate of spontaneous emission; which is inverse proportional to the lifetime of the excited state of the emitter. Before Purcell's

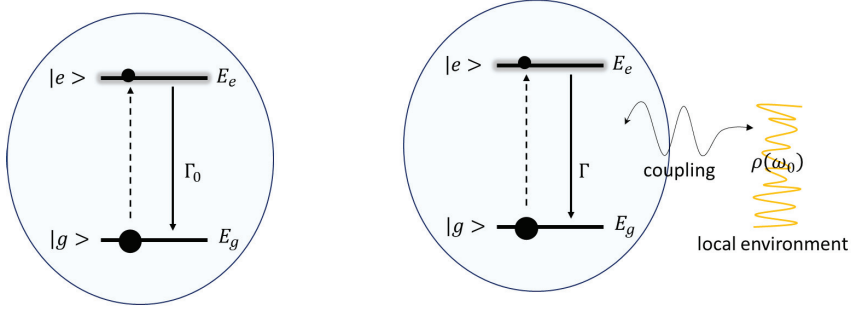


Figure 2.1: **Spontaneous emission: Quantum description.** An emitter is described as a two-level system: (a) the relaxation in a homogeneous medium and (b) coupling to local environment defined by its local density of state $\rho(\omega_0)$.

analysis in 1946 [42], the rate of spontaneous emission was thought to be the unchangeable property of atoms or emitters, which is expressed in vacuum as [43]:

$$\Gamma_0^q = \frac{\omega_0^3 \mu_{ge}^2}{3\pi_0 \hbar c^3} \quad (2.1)$$

where $\hbar\omega_0$ is the difference between ground and excited energies and μ_{ge} is the dipole matrix element between the two optical transition levels.

It has been realized later that the spontaneous emission can be modified by interaction between the emitter and its electromagnetic environment. The modified rate is usually expressed by Fermi's golden rule [44] and is rewritten as:

$$\Gamma^q = \frac{2\omega_0}{3_0 \hbar} \mu_{ge}^2 \cdot \rho(\omega_0) \quad (2.2)$$

Here, the decay rate depends on two factors: the internal structure of the emitter represented by the transition dipole moment μ_{ge} and the electromagnetic environment, which is described by the local density of states (LDOS) $\rho(\omega_0)$ at frequency ω_0 . The LDOS is the number of electromagnetic modes, per unit frequency and per unit volume. In other words, the presence of the local environment opens new channels that are available for the emitter to radiate into, and thus modify the spontaneous emission rate through its LDOS (Figure 2.1b). The idea of enhancement of spontaneous emission was first proposed by Purcell [42], through coupling an atom to a cavity. The ratio between the modified and free-space emission rates

has thus come to be known as the Purcell factor:

$$F_P = \frac{\Gamma^q}{\Gamma_0^q} \quad (2.3)$$

Classical treatment: a harmonic oscillator

The classical picture of spontaneous emission can be described by treating an emitter as a harmonically oscillating dipole. In terms of energy, a harmonic oscillator can be equivalent to a system that has an infinite number of equidistant levels. As the dipole oscillates, it dissipates its energy (determined by integrating the Poynting vector over a surface enclosing the emitter) into electromagnetic radiation. The spontaneous emission rate is now equivalent to the damping rate of the harmonic oscillator, which is defined as the rate at which the energy decayed to $1/e$ of its initial value. In an arbitrary environment, the classical spontaneous emission rate can be found by resolving the equation of motion:

$$\frac{\partial^2 \vec{\mu}}{\partial t^2} + \Gamma_0^{cl} \frac{\partial \vec{\mu}}{\partial t} + \omega_0^2 \vec{\mu} = \frac{e^2}{m} \vec{E}_{loc}(\vec{r}_0) \quad (2.4)$$

where e and m respectively are the charge and mass of electron, $\vec{\mu}$ is the dipolar moment of the dipolar emitter [39]. The term on the right of the equation is related to the driving force $\vec{F} = -e\vec{E}_{loc}(\vec{r}_0)$, and induced the local field $\vec{E}_{loc}(\vec{r}_0)$ that arrives back to the dipole (at position \vec{r}_0) after being scattered by the inhomogeneous environment. For example, this field can be reflecting field from an interface if the emitter is placed in proximity to this interface.

In the free space, this backscattered field is absent and the equation is now the equation of motion for an undriven harmonic oscillator, oscillating at the natural frequency ω_0 with a damping rate Γ_0^{cl} . The spontaneous emission rate of the emitter in the free space is now equal to Γ_0^{cl} , which is given by:

$$\Gamma_0^{cl} = \frac{e^2 \omega_0^2}{6\pi_0 m c^3} \quad (2.5)$$

With the presence of an inhomogeneous environment, both the emission rate Γ_0^{cl} and the oscillating frequency ω_0 are modified by self-interacting with its backscattered field. These can be found (as we will present in detail later) by resolving equation 2.4.

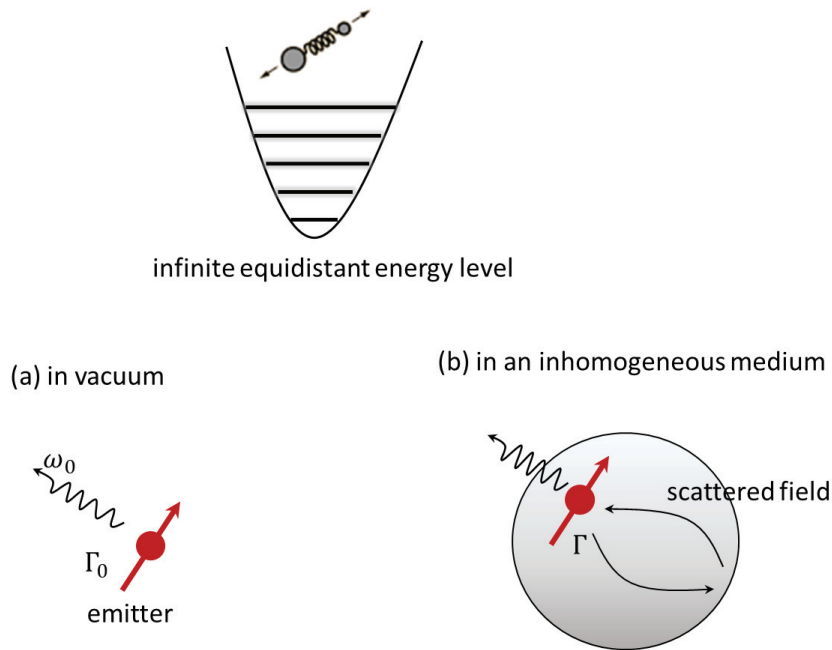


Figure 2.2: **Spontaneous emission: Classical approach.** An emitter is described as a harmonic oscillator of the infinite equidistant energy levels. The damping rate can be modified by the homogeneous medium induced the backscattered field of the medium.

Connecting both pictures

We stress that the decay rate calculated from the harmonic oscillator system is not as rigorously accurate as the one obtained by quantum treatment. Yet, it is possible to account for the spontaneous emission modification of the decay rate $\Gamma^{cl}/\Gamma_0^{cl}$, as we will show later, this gives the same result as the Purcell factor determined by the quantum treatment, under certain conditions. So the question is in which conditions that the classical theory still works properly for the calculation of normalized decay rate? This happens in the situation, in which an emitter is a two-level system, and reacts as a harmonic oscillator. When the two-level system is driven, some electrons distributed at the ground state will be promoted in the excited state. This happens similarly for the harmonic oscillator, except for after being excited, the electrons can immediately go to above-excited states, as the harmonic system contains an infinite number of equidistant energy levels. Thus, the two-level system and the harmonic oscillator could be identical at a weak excitation, from which we can neglect the excitation in higher levels of the harmonic oscillator. This requires the interaction with $\vec{E}_{loc}(\vec{r}_0)$ to be weak, resulting in the shift of frequency being small compared to ω_0

and both terms of $\vec{\mu}$ and $\vec{E}_{loc}(\vec{r}_0)$ have a harmonic time dependence $e^{-i\omega t}$, with ω is new resonance frequency. Replacing these trial solutions for dipole moment and the driving field into equation 2.4, we obtain:

$$-\omega^2 - i\Gamma_0\omega + \omega_0^2 = \frac{e^2}{m\mu_0} E_{r,loc} \quad (2.6)$$

where μ_0 is the amplitude of dipolar moment $\vec{\mu}$ and $E_{r,loc}$ is the complex amplitude of the component field along dipole axis \vec{u}_r of $\vec{E}_{loc}(\vec{r}_0)$. The solution of ω in equation 2.6 is a complex number represented as $\omega = Re(\omega) + Im(\omega)$, in which the real part defines the frequency shift as $\Delta\omega = Re(\omega) - \omega_0$ and the imaginary part determines the total decay rate as $\Gamma = -2Im(\omega)$. As the excitation is weak, the frequency shift should be small compared to its natural frequency: $\Delta\omega \ll \omega_0$. Besides, we assume that the dipolar oscillator has $\Gamma \ll \omega$ (i.e. the oscillation amplitude remains unchanged over period of oscillation), so that later the quadratic terms of Γ^{cl} can be neglected. Applying these assumptions into equation 2.6, we obtain the solution:

$$\begin{aligned} \Delta\omega &= -\frac{\Gamma_0^2}{8\omega_0} - \frac{1}{2} \frac{e^2}{\mu_0\omega_0 m} Re(E_{r,loc}) \\ \Gamma^{cl} &= \Gamma_0^{cl} + \frac{e^2}{\mu_0\omega_0 m} Im(E_{r,loc}) \end{aligned} \quad (2.7)$$

These two solution means that the radiation of a dipole in an inhomogeneous medium leads to the modification of the total decay rate and the shift of resonance frequency, which are respectively responsible for the imaginary and real parts of the backscattered field. Now we can determine the normalized spontaneous emission rate classically as:

$$\frac{\Gamma^{cl}}{\Gamma_0^{cl}} = 1 + \frac{6\pi_0 c^3}{\mu_0\omega_0^3} Im(E_{r,loc}) \quad (2.8)$$

Following [39], the scattered field induces by dipole, at the location of the dipole itself $\vec{r} = \vec{r}_0$, can be represented by the Green's function as $E_{r,loc}(\vec{r}_0) = G(\vec{r}_0, \vec{r}_0)$ (projected along the dipole axis). On other hand, the LDOS can be calculated from the imaginary part of the Green's function: $\rho(\omega_0) \propto Im[G(\vec{r}_0, \vec{r}_0)]$, from which the modification of spontaneous emission rate calculated by the quantum treatment (i.e., Fermi's golden rule) and the classical

self-interaction are equivalent:

$$F_P = \frac{\Gamma^q}{\Gamma_0^q} = \frac{\Gamma^{cl}}{\Gamma_0^{cl}} \quad (2.9)$$

The derivation of the connection between the LDOS and the imaginary part of Green's function can be found in the book [39] of Lukas Novotny and Bert Hecht. In this chapter, now we can use the classical treatment for spontaneous emission of emitter, that latter will be deployed for studying the plasmonic structures.

2.2 Spontaneous emission of a dipole near planar interfaces

The expression of the Purcell factor $F_P = \frac{\Gamma^q}{\Gamma_0^q} = \frac{\Gamma^{cl}}{\Gamma_0^{cl}}$ suggests that we can use the classical approach to study the dynamics of spontaneous emission of a dipole. To serve the purpose of studying the planar plasmonic structure, we first study the spontaneous emission of a dipole near planar interfaces. Lukosz [45, 46, 47] first determined an analytical expression of $\frac{\Gamma^{cl}}{\Gamma_0^{cl}}$ for a dipole in the vicinity of interfaces by a classical near-field calculation. The near-field emission of the dipole is displayed as a superposition of plane waves and evanescent waves of varying in-plane wavevector $k_{||}$. As the decay rate of the dipole is proportional to the total power it radiates

$$P_{tot} = -\frac{dW_{dipole}}{dt} = -\Gamma W_{dipole} \quad (2.10)$$

where W_{dipole} is the dipole's energy, the calculation of $\Gamma^{cl}/\Gamma_0^{cl}$ (or the Purcell factor) is equivalent to the calculation of the normalized total power P/P_0 radiated by the dipole (where P_0 is the power radiated by the dipole in vacuum). To effectively excite the surface plasmon modes that will be discussed later, we employ a dipole that is perpendicular to the interface. Following [46], we express the normalized dissipated power as:

$$\left(\frac{P_{tot}}{P_0}\right)_{\perp} = \frac{3}{2} \text{Re} \left(\int_0^{\infty} (1 + c^p) \cdot \frac{u^3}{\sqrt{1 - u^2}} du \right) \quad (2.11)$$

where $u = \frac{k_{||}}{k_0} = \sqrt{1 - (k_{z,i}/k_0)^2}$ is the normalized in-plane wavevector, with $k_0 = \omega/c$ is the wavevector in vacuum and $k_{z,i}$ represents the vertical component of the wavevector in

the medium i where the dipole is located.

The expression 2.11 can be interpreted as the interference of the field of the dipole in an infinite medium and the reflected field of the nearby interfaces. The latter is represented by the complex field amplitude c^p , which is determined by the boundary conditions for p-polarized fields. Considering two distinguished situations: a dipole near a semi-infinite layer (c_{\downarrow}^p , Figure 2.3a) or a dipole is buried in a layered medium consisting of multilayer ($c_{\downarrow\uparrow}^p$, Figure 2.3b); the complex field amplitudes are respectively given by:

$$c_{\downarrow}^p = r_{i,\downarrow}^p(u) \cdot e^{2ik_{z,i}d_{\downarrow}} \quad (2.12)$$

and

$$c_{\downarrow\uparrow}^p = \frac{2r_{i,\downarrow}^p(u)r_{i,\uparrow}^p(u)e^{2ik_{z,i}(d_{\downarrow}+d_{\uparrow})} + r_{i,\uparrow}^p e^{2ik_{z,i}d_{\uparrow}} + r_{i,\downarrow}^p e^{2ik_{z,i}d_{\downarrow}}}{1 - r_{i,\downarrow}^p(u)r_{i,\uparrow}^p(u)e^{2ik_{z,i}(d_{\downarrow}+d_{\uparrow})}} \quad (2.13)$$

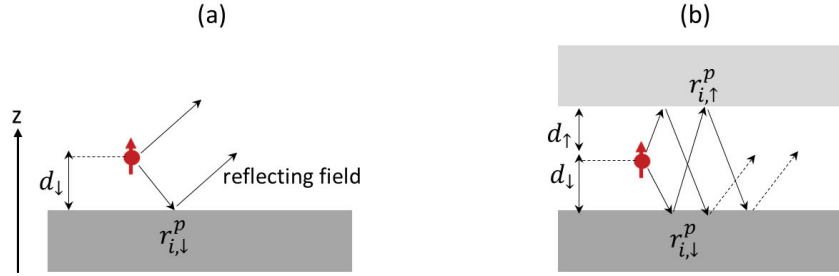


Figure 2.3: **Two situation of a dipole near interfaces.** Radiating of a dipole near (a) a single interface: direct radiation of dipole can interfere with its reflection on the interface and (b) in between two interfaces: multiple interactions are induced by the two interfaces.

The indices \downarrow, \uparrow respectively, denote upward and downward media. For multilayer structure, $r_{i,\downarrow}^p$ and $r_{i,\uparrow}^p$ correspond to the Fresnel reflection (p-polarization) coefficients calculated by the transfer matrix (see Ph.D. these of Kelvin [48]). The quantities d_{\downarrow} and d_{\uparrow} are the distance from the dipole to the below interface and upper interface. The geometry is schematized in Figure 2.3. In the case of a dipole close to the planar interface (Figure 2.3a), it only feels the reflection of the surface. For a dipole embedded in a layered medium (Figure 2.3b), the fields emitted by the dipole are initially reflected by the interfaces i, \uparrow and i, \downarrow and are then reflected back and forth between the two interfaces. This leads to the multiple beam-interference factors appearing as the denominator in the expression 2.13 of $c_{\downarrow\uparrow}^p$.

The integral in the expression 2.11 represents the normalized power dissipated by the dipole in the directions of the optical modes whose component in-plane wavevector is u . The values of $u < 1$ correspond to radiative emission, and the values $u > 1$ are associated with near-field emission. By separating the integral spatially in different domains of u , the optical modes of the system can be identified. We, therefore, employ a single vertical dipole as a local probe to study plasmonic structures. In the following, from the calculation of the dissipated power presented above, we extract three important physical quantities for the characterization of the plasmonic system:

- the spatial distribution of the dissipated power α_{\perp} that allows identifying the contribution of the component optical modes,
- the coupling efficiency to the modes β^m ,
- the Purcell factor F_P

2.3 Coupling a dipole to fundamental planar plasmonic structures

The layered structure with subsequent lateral patterning are based around three fundamental structures: (i) insulator/ metal (IM), (ii) insulator/metal/insulator (IMI), or (iii) metal/insulator/metal (MIM). In this Chapter, we first employ a dipole to investigate the optical modes supported by these planar plasmonic structures. Figure 2.4 illustrates the schematic of each structure. For calculation, the insulator and the metallic layers are assumed to be air and gold ($n_{Au} = 0.15 + 3.32i$ at $\lambda = 650\text{nm}$ [11]), respectively. To effectively excite the optical modes of the surface [45], we place a vertical dipole emitting at $\lambda = 650\text{nm}$ in the air layer at a distance of $d_{\downarrow} = 15\text{nm}$. The gap in the IMI and MIM structures has an equal thickness $g = 2d_{\downarrow} = 30\text{nm}$. We stress that the main goal of this work is to probe in a given configuration the Purcell factor and the optical modes, the choice of the configuration's parameters is not optimal.

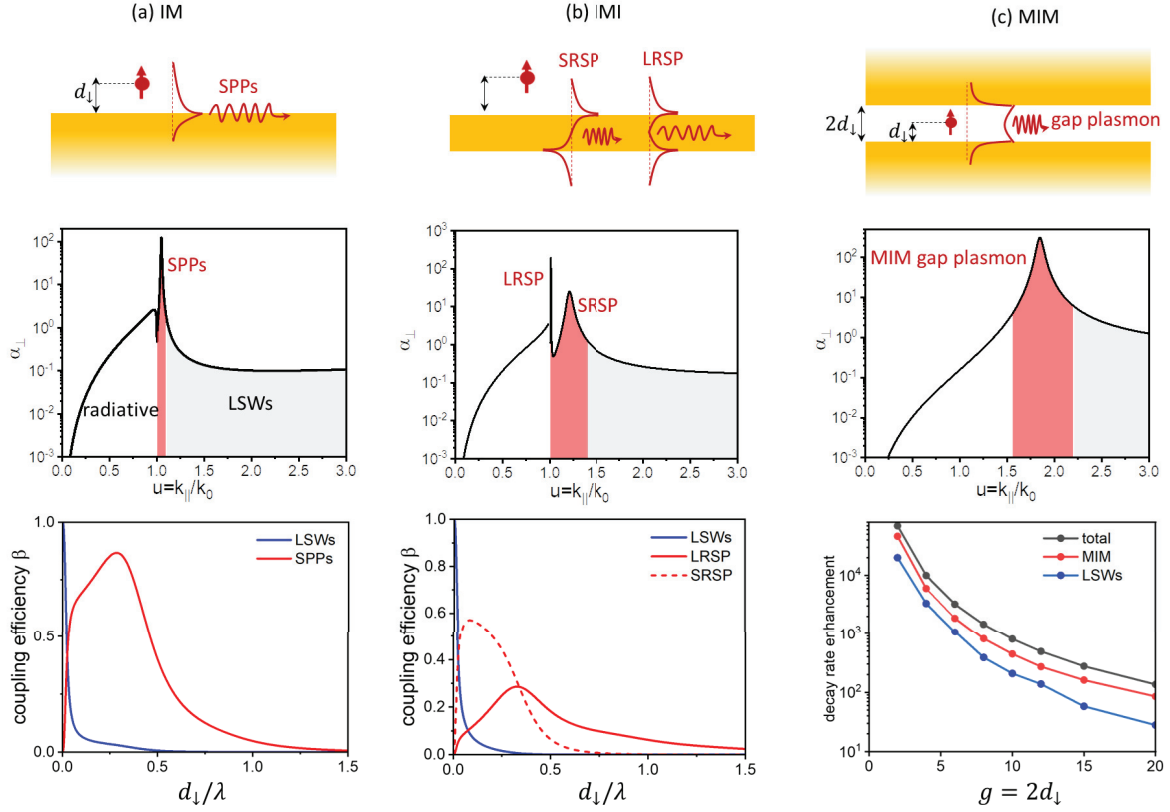


Figure 2.4: **Coupling a dipole to surface plasmon.** (a) single insulator/dielectric (IM) interface. (b) insulator-metal-insulator (IMI) structure. (c) metal-insulator-metal (MIM) structure. Second row: Calculation of spatial spectrum of the power dissipated by the dipole. Third row: Calculation of coupling efficiency to the modes as a function of the dipole’s distance (IM and IMI) and decay rate enhancement of the MIM modes as a function of the gap thickness.

Identification of optical modes supported by the structure

To determine the optical modes supported by the structure, we calculate the spatial spectrum of the power dissipated by the dipole (i.e., the dissipated power as a function of the normalized in-plane wavevector u), which is given by:

$$\alpha_{\perp}(u) = \frac{d\left(\frac{P_{tot}}{P_0}\right)_{\perp}}{du} \quad (2.14)$$

The calculation of α_{\perp} is presented in Figure 2.4 (second row). The presence of the surface plasmon in each structure is filled in red, which superimposes to a broad “background” containing both values of u less than 1 (far field) and greater than 1 (near field). For

$0 < u < 1$ (white region), the processes associated with photon radiation the free-space. The mode corresponds to values of u above surface plasmon modes (grey region) referred to as lossy surface waves (LSWs) or quenching. This transfers the dissipated power of the dipole to the electron-hole pairs of metal.

For the IM structure, we observe a peak at $u = 1.1$ (red region), which is associated with the wavevector of SPPs propagating along the air/ gold interface ($k_{SPP}/k_0 = 1.1$). In the case of IMI structure, the spatial spectrum of α_{\perp} features two distinctive peaks in the near-field regime ($u > 1$), which results from the SPP the hybridization of SPPs bound to each interface. The mode at smaller u has a narrower width (which means fewer losses or longer propagation length) and is called long-range surface plasmon (LRSP). The other one holds an opposite feature and is referred to as short-range surface plasmon (SRSP). In terms of the field, these two modes are also usually referred symmetric (LRSP) and anti-symmetric (SRSP) gap modes. The mode hybridization in the IMI structure is very sensitive to the surrounding dielectric optical indices. If the difference between the optical index of the upper and lower insulators are very different (10%), the SPPs of each interface will be decoupled, and only the independent SPPs will remain [49]. In the MIM structure, the SPPs on either side of the insulator medium similarly hybridize to form symmetric gap mode (the anti-symmetric mode is cut-off at roughly $\lambda/2n$ [38, 50]), which features as a monomode with a broad width on the spatial spectrum of α_{\perp} .

For comparison with the two other structures, the gap MIM has the largest k_{\parallel} and spectra full-width at half-maximum (FWHM), which means the strongest field confinement. However, the confinement of the gap MIM is accompanied by short propagation length. The propagation length of the mode is determined by the imaginary part of the k_{\parallel} as $L = 1/(2Im(k_{\parallel}))$, which in turn is related to the FWHM of the plasmon peaks as $Im(k_{\parallel}) = k_0.FWHM$. From this, we deduce the propagation lengths of $9\mu m$ (SPPs), $2\mu m$ (SRSP), $44\mu m$ (LRSP), and $10nm$ (gap MIM).

Coupling efficiency to the mode

In proximity to the metallic surface, the emission process of a dipole is mainly a competition between the surface plasmon modes and quenching (LSWs). We define the β -factor, which gives the fraction of the total dissipated power funneled into one mode by integrating

the spatial spectrum over the spatial region yields to the mode. It can be represented as

$$\beta = \frac{P_m}{P_{tot}} = \frac{\Gamma_m}{\Gamma_{tot}} = \frac{\int_{u \in \text{modes}} \alpha_{\perp}(u) du}{\int_0^{+\infty} \alpha_{\perp}(u) du} \quad (2.15)$$

This fraction is equivalent to the normalized decay rate of dipole emission into the mode. Figure 2.4 (third row) shows the β -factor of surface plasmon modes and quenching calculated as a function of the normalized separation d_{\downarrow}/λ (for IM and IMI) or the insulator gap thickness g (for MIM). When the g changes, we note that the dipole is always placed in the middle of the gap as $d_{\downarrow} = g/2$.

In the IM and IMI structures, there are optimal distances yield to a maximum of β -factor of plasmon modes: $\beta_{SPP}^{max} = 80\%$ at $d_{\downarrow} = 0.3\lambda$, $\beta_{SRSP}^{max} = 55\%$ at $d_{\downarrow} = 0.25\lambda$, and $\beta_{LRSP}^{max} = 55\%$ at $d_{\downarrow} = 0.5\lambda$. At these optimal distances, the plasmon modes largely overcome the quenching (blue curve, Figure 2.4). Above this distance, the radiative is the dominant channel. The quenching tends to be localized near the metallic surface, which has the coupling efficiency scales as d_{\downarrow}^{-3} as $d_{\downarrow} \rightarrow 0$. This scaling is understood from the local and static nature of the quenching. Below 10nm, the quenching is the dominant decay channel of the dipole.

For the MIM structure, we prefer to present the normalized decay rate of the modes Γ_m/Γ_0 rather than their coupling efficiency because the structure does not exhibit an optimal distance where the coupling efficiency to the mode reach maximum, as seen in the IM and IMI structures. Indeed, the gap mode and the quenching have identical separation distance d_{\downarrow}^{-3} scaling as d_{\downarrow} vanished (Figure 2.4). We note that the dissipated power into quenching of MIM gap (or quenching rate) is $\sim 2 - 3$ times higher than that of the dipole near a single interface of IM or IMI structure. Interestingly, we find that the coupling to plasmon gap mode overcomes the quenching despite the very proximity to the metal ($d_{\downarrow} < 10\text{nm}$). This is attributed to the slowdown of the gap plasmon mode (group velocity decrease) and thus strong field confinement when the gap thickness is reduced [51, 52].

The Purcell factor

The Purcell factor defines the total decay rate enhancement (as compared to vacuum decay rate Γ_0) that can be calculated by integrating the spatial spectrum of α_{\perp} over all values of u ,

$$F_P = \frac{\Gamma}{\Gamma_0} = \int_0^{+\infty} \alpha_{\perp}(u) du \quad (2.16)$$

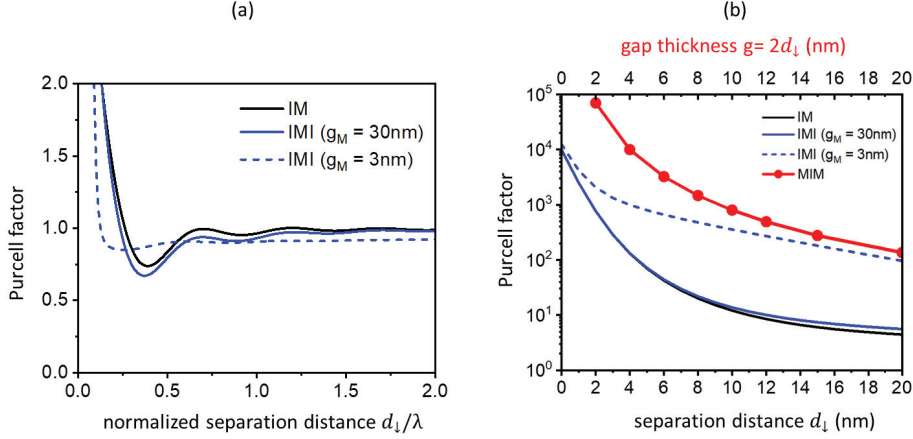


Figure 2.5: **The Purcell factor.** (a) Purcell factor of the dipole in the IM and IMI structure as a function of the dipole distance. Two gap thicknesses of the IMI structure are considered: $g_M = 3\text{nm}$ and $g_M = 30\text{nm}$. (b) Similar to (a) but focusing on smaller distance and compare to the MIM structure. Only the IMI of $g_M = 3\text{nm}$ is considered.

Figure 2.5 a shows the calculation of F_P as a function of the normalized separation distance d_{\downarrow}/λ of the IM and IMI structure. We can see that the Purcell factor of the IMI with the gold slab thickness $g_M = 30\text{nm}$ (blue line) is nearly identical to that of the single air/gold interface (black line). When the dipole is far from the interface, the F_P slightly oscillates around unity ($\Gamma = \Gamma_0$) due to the interference between the far-field radiation of the dipole and its reflected field from the surface. As $d_{\downarrow} < 10\text{nm}$, the Purcell factor of these two structures increases rapidly; however, this is dominantly due to the quenching as shown in Figure 2.4.

In Figure 2.5 b, we also calculate the Purcell factor of the MIM structure as a function of gold thickness $g = 2d_{\downarrow}$, focusing on the thicknesses of interest $g < 20\text{nm}$. We note that dielectric gap thickness at a 10nm scale is possible to achieve by state-of-art lithography or self-assembled monolayer of molecules ($g < 2\text{nm}$) [53, 54]. Here we find that the F_P is also significantly enhanced as the gap thickness reduces ($F_P \approx 10^5$ at $g = 2\text{nm}$) and is more prominent by around 2 orders of magnitude than that of IM or IMI ($g_M = 30\text{nm}$) structures. Moreover, as proved previously, the large F_P of the MIM structure is predominantly driven by

the gap plasmon mode but not the quenching, even at very small d_{\downarrow} . It is thus apparent that the MIM nanogaps can provide extreme light confinement inside the dielectric gap that its excitation can compete with the quenching, thus propelling their use in various applications related to enhancing spontaneous emissions such as single photon sources or sensing.

The IMI structure with extremely thin metallic gap thickness

Above we have considered the IMI structure with gold thickness $g_M = 30\text{nm}$, which shows no significant difference in Purcell factor as compared to a single IM interface. In fact, above the gold's skin depth ($> 20\text{nm}$), the F_P of the IMI structure is not understood to depend on the gap thickness, except that the plasmon mode hybridization is loose. Here, we are interested in calculating the Purcell factor of an IMI structure with a very small thickness, $g_M = 3\text{nm}$ for example (the thinnest metal sheets have reached), shown as the blue dashed line in Figure 2.5 . This geometry has been recently studied in graphene plasmonics [55] or nanoparticle-on-foil system [56], which allow tightly confined light and can be used as molecular sensing. Here we find that in the far-field regime (d_{\downarrow} is large, Figure 2.5a), the F_P is nearly unaffected by the presence of very thin gold film thickness, which shows no significant difference from that of a dipole in a vacuum. In contrast, in the near-field regime (Figure 2.5b), the F_P of 3nm-gap-IMI is largely enhanced by 2 orders of magnitude compared to 30nm-gap-IMI, which is an asymptote to the huge F_P of the MIM structure for $10 < d_{\downarrow} < 20\text{nm}$. This is primarily contributed by the strong field confinement of the as-symmetry IMI mode (SRSP) as its field is null inside the metal gap [56]. Besides, in terms of the in-plane wavevector (k_{\parallel}), when g_M reduces, k_{\parallel} of LRSP mode remains unchanged and very close to the k_{\parallel} of SPPs on a single gold interface. In contrast, k_{\parallel} of SRSP largely increases by ~ 10 times, making it possible to be confined inside the extremely thin gold gap. When $d_{\downarrow} < 10\text{nm}$, the Purcell factor curve of the 3nm-gold-IMI structure converges toward the Purcell factor curve of IM, and the 30nm-gold-IMI structure owing to the dominance of the quenching in this regime.

2.4 Coupling a single dipole to a long-range surface plasmon device

Studying the plasmon modes hybridized inside the IMI structure above reveals several promising advantages of the long-range surface plasmon modes: very few losses compared to the SPPs at the single interface as long as millimeter range propagation length can be reached [37], and the tolerance on the structure symmetry is a few percent (achievable experiment). The LRSPs are thus the potential for many applications and have been proposed for optoelectronic devices [57], energy transfer [58], and biological sensors [59]. In a recent paper, we experimentally demonstrated a strong coupling between the LRSP and J-aggregate dyes [37]. We demonstrated that this device enhances the coupling and, depending on the position of the dyes, new modes can be excited.

The motivation of this section is to present a new study of the “more realistic” LRSP device [60, 37] in the weak coupling regime. Using the same dipolar approach above, we focus on the identification and reconstruction of the different modes supported by the device. Besides, the coupling efficiency to the mode is extracted depending on the dipole’s position and orientation. Finally, we present an optimization procedure as a guideline for future optoelectronic devices.

The device is presented in Figure 2.6a. We set the same gold slab of 30nm between two finite glass layers denominated substrate and superstrate (index 1.5, thicknesses 750nm) and we place the whole structure on a prism of index 1.8. The dipole is placed at $d_{\downarrow} = 50\text{nm}$ from the gold layer inside the superstrate. This configuration is also known as Otto or leakage configuration [29, 61]. The chosen parameters here serve the purpose of demonstrating the system, while their influence will be discussed later.

Identification and reconstruction profile of optical modes supported by the device

Figure 2.6b shows the spatial spectrum of α_{\perp} of the dipole as a function of u . We can that the device supports the plasmonic modes (LRSP and SRSP) located at $u > 1.5$. Furthermore, new modes appear for $u \in [1; 1.5]$, which belongs to the glass side of index 1.5. The inset presents the Purcell factor as a function of the distance from the gold layer. No difference is

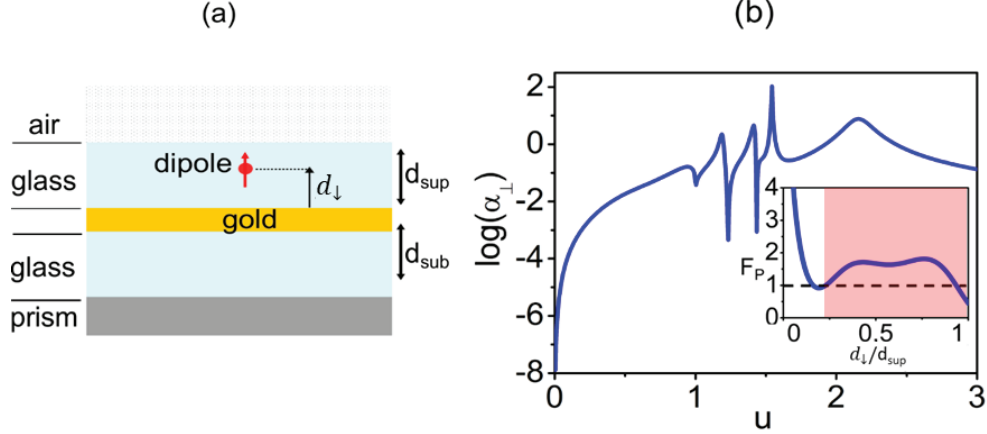


Figure 2.6: **A realistic long-range surface plasmon configuration.** (a) Schematic of the structure. (b) Plot α_{\perp} as function of the in-plane wavevector u . Inset: Corresponding Purcell factor.

observed with the case of IMI structure in Figure 2.5a in the near-field regime ($d_{\downarrow} = 50\text{nm}$) but a new structure appears in the far-field distance (red arrow). These new modes are thus propagative, belong to the glass, and will be attributed to wave-guided-modes (WGMs). In Figure 2.7, we present a procedure to identify, optimize and reconstruct each mode's profile.

The identification of the optical modes is done by comparing the intensity reflection coefficient (R_p , R_s) as function of the normalized in-plane wavevector u in p and s polarizations with the calculated α_{\perp} . These latter three curves are plotted in Figure 2.7a. It is important to note that for reflectivity calculations, the wavevectors are limited by the index of the prism ($u < 1.8$). We see that the modes in the α_{\perp} curve also appear in R_p at the same positions, resulting from the vertical dipole near an interface mostly radiating p-polarized field inside a higher index medium [39]. On the other hand, if we set a horizontal dipole, the dissipated power would have been distributed in both p and s modes (the role of the dipole orientation will be examined at the end of this section). The mode at α_{\perp} ($u = 1.6$) appears only in p-polarization, while it is absent in s-polarization. This dependence on the polarization confirms that this mode has plasmonic nature, which we attribute to LSRP mode. Moreover, we observe that the SRSP is located at α_{\perp} ($u > 1.6$), thus making it impossible to detect in this configuration. For $1 < u < 1.5$, many other modes are present in both polarizations. These modes are attributed to wave-guided modes (WGMs).

In Figure 2.7b, we calculated the coupling efficiency β of the vertical dipole within the

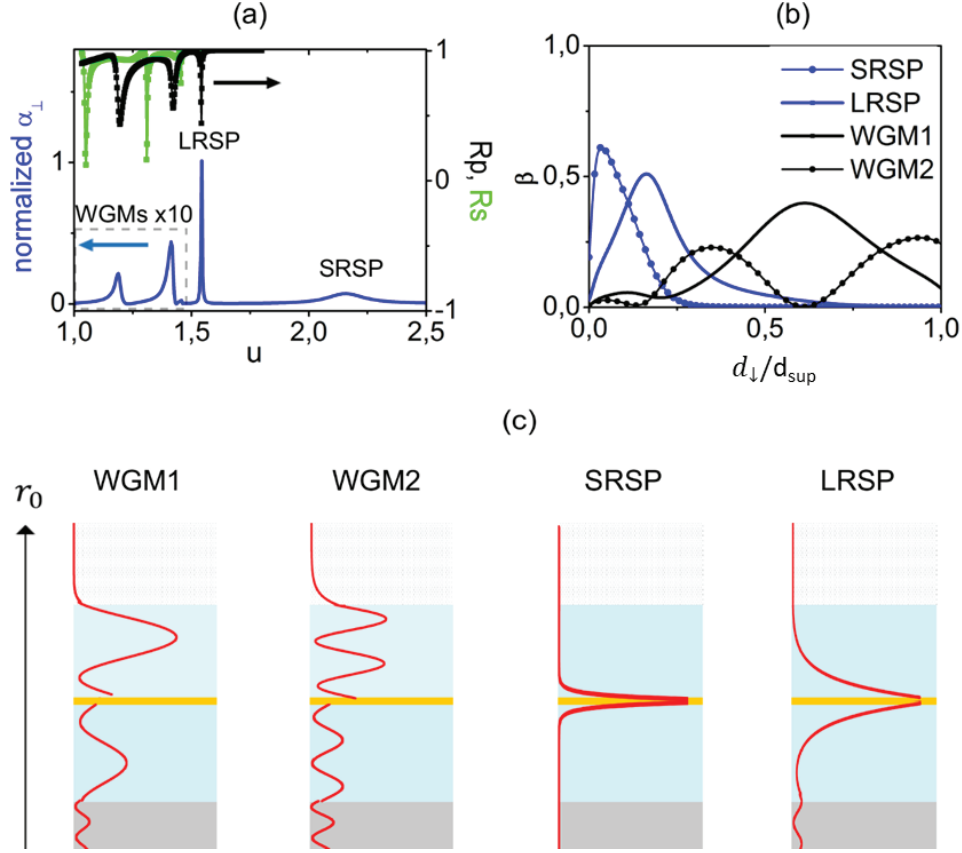


Figure 2.7: (a) Dissipated power and reflectivity simulated as a function of u . (b) Coupling efficiency to the different modes as a function of the vertical distance in the glass. (c) Mode profiles $|\vec{e}_n(r_0)|^2$.

superstrate as a function of the separation distance to the gold. First, we note that the coupling efficiency of the LRSP and the SRSP does not change in this device as compared to the ideal structure IMI with insulator sides made from glass. The finite size of the structure (750nm of glass thickness) does not disturb these modes. Secondly, we see that the coupling efficiency to the guided modes can be: $\beta_{WGM}^{max} = 40\%$, which is obtained deeply inside the glass layer. We have one and two maxima for WGM1 and WGM2 respectively which seem to reproduce the spatial shape of the modes. One important feature is that the number of modes depends on the position of the dipole inside the glass slab. For example, for a dipole position at $d_{\downarrow} = 0.3d_{sup}$, three modes are excited with 25% of total power dissipated to WGM2, 15% to the WGM1, and 15% to LRSP.

To complete the description of the modes and to display the energy propagation within the structure, we reconstruct the mode profiles. It has been shown that in the case of discrete

modes, the LDOS can be formulated through a summation. This calculation is then weighted by the amplitude of the eigenmodes at the dipole position r_0 as [62]:

$$\rho(r_0, \omega) = \sum_n |\vec{e}_n(r_0)|^2 \delta(\omega - \omega_n) \quad (2.17)$$

We have reconstructed the mode profile $|\vec{e}_n(r_0)|^2$ by first selecting the mode wavevector u and then moving the position of the dipole. Figure 2.7c presents the profile structure of the four modes independently. We observe the profile shape of the plasmon with an exponential decrease in the dielectric surrounding the gold. In the case of the WGM, we observe the number of nodes, in the upper glass, according to the order of the mode. We notice that the WGM profiles are not completely symmetric in the superstrate because of the as-symmetry in terms of the optical index of the surrounding medium (i.e., the device around the gold film).

Optimization of coupling efficiency

Until now, only a vertical dipole has been set to clarify the discussion and to optimize the coupling to plasmonic modes. Using complementary reflectivity calculations, we have identified all the modes. In Figure 2.7a, we also clearly see that the waveguided modes also occur for s-polarization which may be excited with a horizontal dipole. Depending on the purpose of various applications, it may be more interesting to mostly couple to the LRSP or to both LRSP and WGMs in a defined proportion.

For all these reasons, we introduce a new contrast parameter C between the LRSP and the WGM. This factor of merit highlights the tolerance and optimization of the coupling within the desired mode.

$$C = \frac{\beta_{LRSP} - \beta_{WGM}}{\beta_{LRSP} + \beta_{WGM}} \quad (2.18)$$

The coupling efficiencies for WGMs are integrated for $u \in [1; 1.5]$. Figure 2.8 displays the behavior of C with the most important parameters which are the gold distance and the dipole orientation. We retrieve the previous result which is a better coupling to the LRSP with a vertical dipole at short distances. In this case, the range of angle tolerance is around 20° . A horizontal dipole ($\theta = 90^\circ$) will barely couple to the LRSP (only at very short distances).

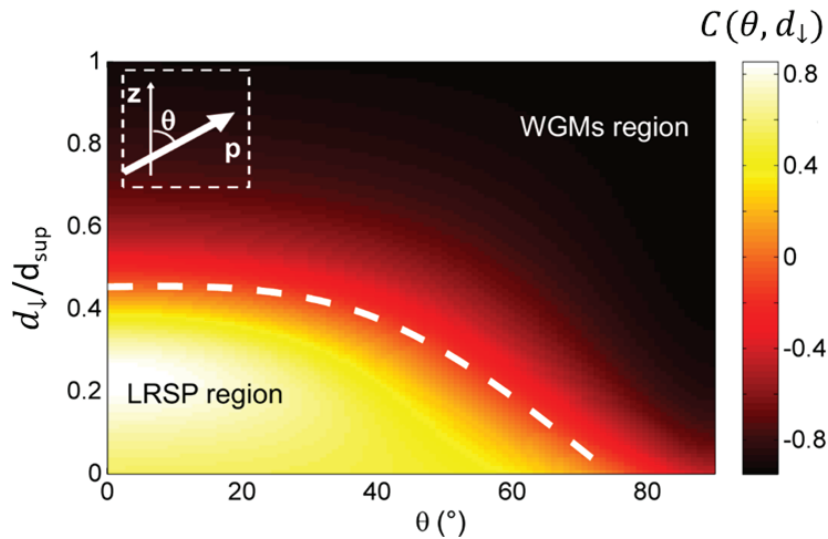


Figure 2.8: **Contrast map as function of the vertical distance d_{\downarrow} in the superstrate and with the dipole orientation θ .** The dash lines point-out the delimitation between each region. Inset: schematic of the dipole orientation.

There is an intermediate range (for $C = 0$), where the dipole will couple to each mode with equivalent efficiency, this region is marked with the white dash. This calculation is only valid for one dipole. In the case of a monolayer of random independent emitters, we have to average our calculation over all orientations θ .

Conclusion: To conclude this section, we have investigated the dipole coupling into a Long-Range plasmonic device. In a symmetric configuration where a gold slab is inserted in-between two identical mediums, the dipole may radiate into a Long-Range plasmon. The dissipated power is redistributed into the Long Range as well as in a Short Range plasmon. The coupling efficiency to the LRSP is around 57 and the propagation length is around 44m for wavelength of 650nm. In an even more realistic configuration, where the mediums have finite sizes, waveguided modes may also appear in the dielectric layers without modifying the properties of the LRSP. According to the orientation of the dipole, the coupling efficiency may be optimized and balanced between the LRSP and the WGM. One interesting feature is that these channels may be independent (in wavevector) or coupled (excited by the same dipole) depending on the optimization. This configuration may be interesting for multimode integrated devices such as single photons on chip, quantum entanglement or for optical communications. More details of this part can be found in [49].

2.5 Surface plasmon hybridized dressed states

Multiple-hybridization between metallic layers inside plasmonic nanocavities displays properties similar to atomic-dressed states. In this framework, we propose to numerically and analytically investigate the case of a multilayered structure composed of N stacks of metallic (M) and insulator (I) thin films. We also use a vertical dipole as an optical probe buried inside the structure to excite the optical modes. To understand the multiple-plasmon hybridization of the structure, we begin with a layered structure with a small number of metallic slabs ($N = 3; 4$). When the number of blocks is increasing, we will show that the resulting modes evolve toward an energy continuum in a manner similar to the energy bands in a solid.

Surface plasmon modes of alternative insulator/metal multilayer: begin with 3 and 4 metallic layers

In the following, we discuss about the construction of the plasmonic modes due to multi-hybridization by first analyzing coupling between 3 and 4 metallic layers. These configurations are labeled MIMIM and MIMIMIM. In Figure 2.9, the dissipated power is calculated and the profile of each mode is extracted for each geometry. All layer thicknesses are set to 20nm.

In the case of 3 metallic layers, we observe two modes noted M1 and M2 in Figure 2.9a. We clearly observe different widths in u for these modes which is a fingerprint of their losses. In Figure 2.9b, the M1 mode, with smaller losses, is rather located near the outer limit of the structure, whereas the M2 mode, which has more losses, is propagating close to the central metallic layer.

In the case of 4 metallic layers, we observe the appearance of three modes with different widths. The profile of these new modes displays similar features as those presented in Figure 2.9a and b. The first mode M1, with the narrowest width, is more likely located in the central insulator. Its profile increases in the vicinity of the external metallic layers. By contrast, the modes (M2 and M3) with broader widths tend to localize closer to the central metallic layer. In particular, the intermediate M2 mode is vanishing inside the middle of the structure. Considering the cases of 3 and 4 metallic layer structures, we generally observe

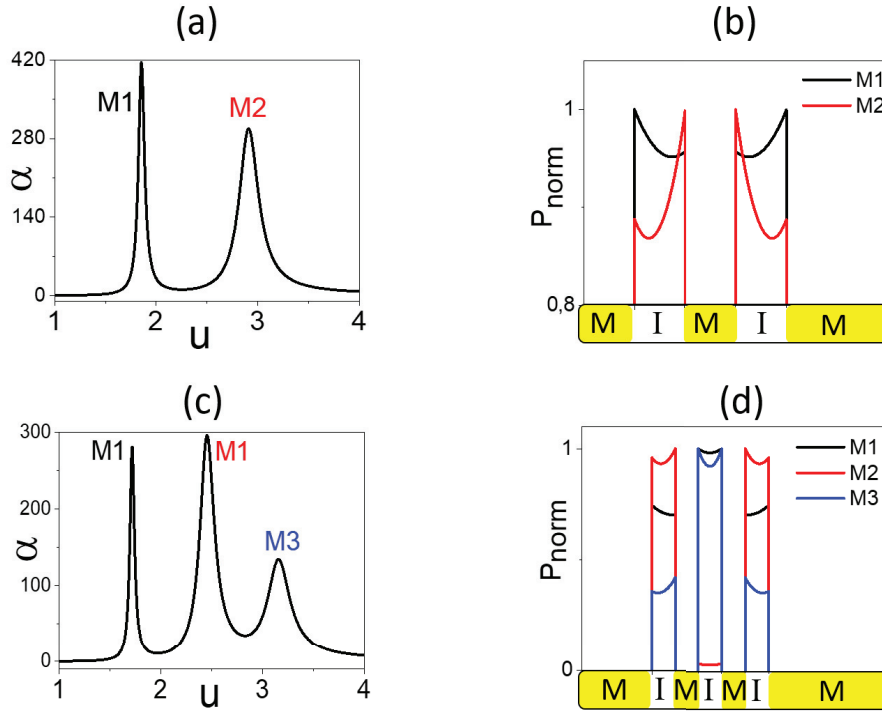


Figure 2.9: **Three and four multilayers.** Dissipated power as a function of the wavevector u for (a) MIMIM and (c) MIMIMIM structures. (b,d) Corresponding spatial profiles of each selected mode. The dipole is placed at 10nm from the metal in the left insulator (I) layer displayed (b,d). The finite layer thicknesses are set to 20nm.

that the modes which present more losses are those that are more closely located near the central metallic layer. In both cases, the SPP modes at lower wavevector display fewer losses, propagate farther, and increase systematically near the external metallic layers.

Multiple-plasmon hybridization between metallic layers

To understand the creation of these new coupled modes, one of the insulator (I) layers is replaced by a dielectric with a variable refractive index n , while the other insulators are air. On the basis of our previous analysis, changing the optical index is expected to detune the respective energies between the modes to decouple them [63, 64]. This results in a characteristic anti-crossing pattern. For this analysis, we assume that the independent modes are those of the MIM structure. The evolution of the independent MIM mode where the index of dielectric n is changed is denoted MnM and the results are presented in Figure 2.10.

We observe the appearance of 2 and 3 branches for the case of 3 and 4 metallic layers

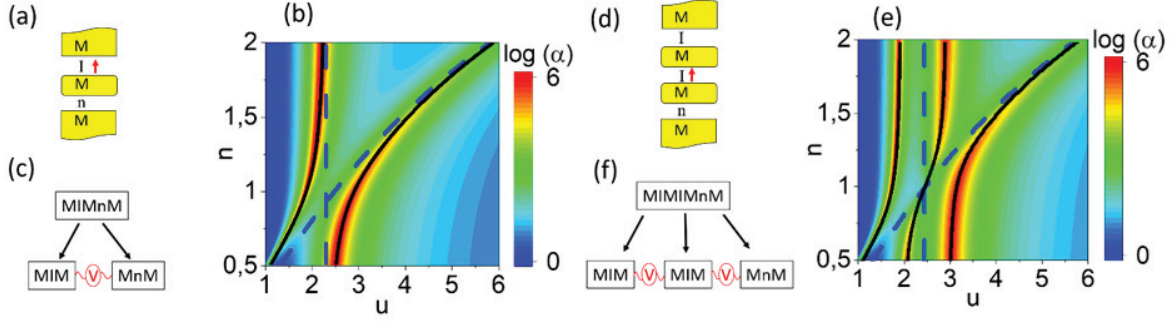


Figure 2.10: **Construction of plasmonic modes in the case of structures with 3 and 4 metallic layers and a dielectric layer of variable refractive index.** (a,d) Schemes of the devices. The position of the dipole is shown by a red arrow and located at 10nm from the metallic surface. (b,e) Evolution of α_{\perp} as function of n and u of the associated structures. The dashed lines are the positions of the independent modes (u_{MIM} and $u_{MnM}(n)$) and the continuous lines are the calculated eigenmodes of the interaction matrix. (c,f) Schematic diagram of the mode construction for 3 and 4 metallic layers respectively.

in the anti-crossing maps (Figure 2.10b, e). For example, for 4 metallic layers, a simple matrix formalism, grounded on physical considerations, can be introduced to reproduce the simulations. This case is based on the interaction between three coupled MIM structures. The interaction matrix can be written as:

$$u_{MIMIMnM} = \begin{pmatrix} \tilde{u}_{MIM} & V_{12} & V_{13} \\ V_{12} & \tilde{u}_{MIM} & V_{23} \\ V_{13} & V_{23} & \tilde{u}_{MIM}(n) \end{pmatrix} \quad (2.19)$$

In matrix $u_{MIMIMnM}$, we insert the wavevectors of the SPP for the MIM structure \tilde{u}_{MIM} . This value can be slightly corrected due to the finite size of the layer. The SPP wavevector of the MnM structure is noted as $\tilde{u}_{MIM}(n)$. These two values are extracted from simulations. We also define V_{ij} as the interaction strength between i and j layers, in order to reproduce the numerical simulation. In Figure 2.10b, e, we present, in black continuous lines, the calculated eigenmodes from the matrix. These results are superimposed on the simulations for the cases of 3 and 4 metallic layers. We found that only the first neighbor's MIM structures are interacting and that the coupling strength between neighbors does not depend on the overall structure (namely 3 or 4 metallic layers). For the case of 4 metallic layers, the independent mode of the MIM structure is used twice in the matrix. As these 2 modes are degenerate

(wavevector \tilde{u}_{MIM}), only one vertical dash line appears in Figure 2.10e. In the case of 4 layers of equation 2.19, we deduce $V_{12} = V_{23} = V = 0.5$, $V_{13} = 0$. The wavevector of the MIM plasmon of the single IM interface is corrected by 0.25, so that $\tilde{u}_{MIM} = u_{MIM} + 0.25$. Finally, we also found that the correction to MnM is $\tilde{u}_{MnM} = u_{MnM}(n) + 0.3$. The most important result is that, in the case of successive layers with the same thickness and index, we always have only first neighbors coupling with the same coupling $V = 0.5$. Finally, it is worthwhile to note that the regime of strong coupling can be achieved when the ratio of the coupling strength to their intrinsic losses is higher than 1 [64]. In our case, the coupling strength is $2V = 1$ and the losses, given by the width of the independent MIM mode, is $\Delta u = 0.1$. The strong regime criterion is, therefore, $V / \Delta u \gg 1$.

Surface plasmon hybridization: N layers

In the following, we analyze the evolution of these hybridized modes as a function of the number of metallic layers. All dielectric layers are set to air to maximize the hybridization coupling strength. We note N_b as the number of metallic layers so that the overall structure possesses $(N_b - 1)$ air layers. For example, the MIM structure is obtained for $N_b = 2$. The thicknesses of both finite gold and air layers are set to 20nm. The dipole is placed in the center of the global structure (similar to Figure 2.10). If the center is air, the dipole is placed in the center and if it is metallic, the dipole is set 10nm above. The results are presented in Figure 2.11.

In Figure 2.11a, we see that the number of plasmonic modes increases with the number of layers. It is important to note that in our simulations, the dipole probes the Local Density of Optical States (LDOS). We see that for the case of 8 gold layers, the amplitudes of the modes are different. The distribution of the nodes of the various modes in the structure are different, so that the dipole may not be able to excite all the modes with the same efficiency. Nevertheless, when the number of layers is very large, all the modes merge to form a continuum in a similar way as the energy bands in a solid. The simulated colormap in Figure 2.11b illustrates this evolution. We see that when N_b is increasing, multiple hybridization occur and we observe the coalescence of all modes. In Figure 2.11a and b, we also detect two asymptotic limits of the wavevector values that will be noted $u_{limit} = u_{max}$ or u_{min} .

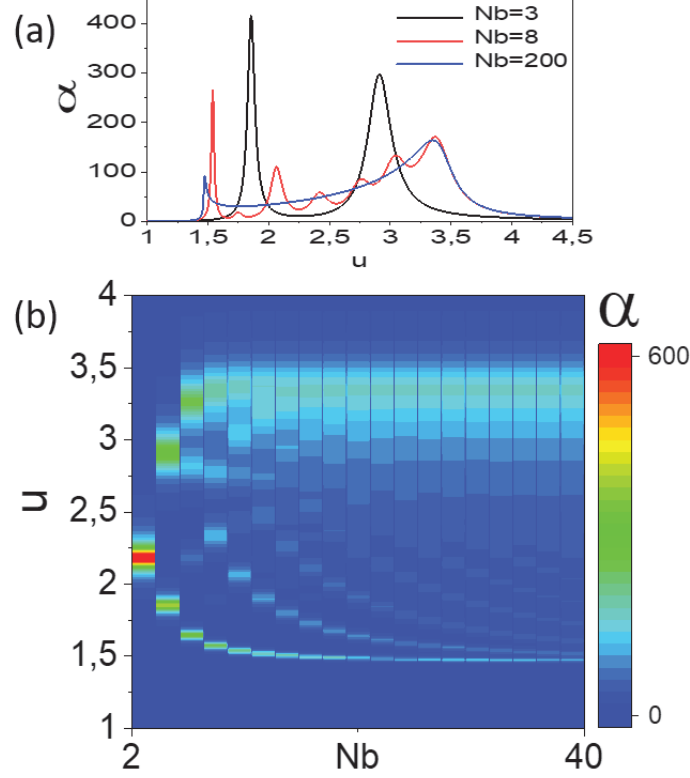


Figure 2.11: **Evolution of the dissipated power α as function of the number of metallic layers N_b .** (a) Dissipated power α as a function of the in-plane wavevector u for 3 different numbers N_b (3, 8 and 200) and (b), as a colormap with u and N_b from 2 (MIM scheme) to 40.

In Figure 2.11b, we find them close to $u_{max} = 3.4$ and $u_{min} = 1.5$. These asymptotic values are dependent on the thickness of the gold or the air layers as illustrated in Figure 2.12. As expected, the asymptotic evolution ($N_b \rightarrow \infty$) of the wavevector u tends to the initial values of building blocks (MIM or IMI) presented in Fig.1. When increasing the thicknesses (e_M or e_I), the building blocks forming the overall structure become actually decoupled. When the dielectric layer thickness e_I is infinite, the global structure tends to an IMI scheme with long-range (LR_{IMI}) and short-range (SR_{IMI}) plasmon. In the opposite case, when the metallic layer thickness e_M is very high, the global structure adopts the behavior of a MIM structure with one plasmon mode (SPP_{MIM}).

Conclusion: To conclude this section, we have studied multiple hybridization between MIM structures. Hybridization occur at a small distance between adjacent MIM blocks with

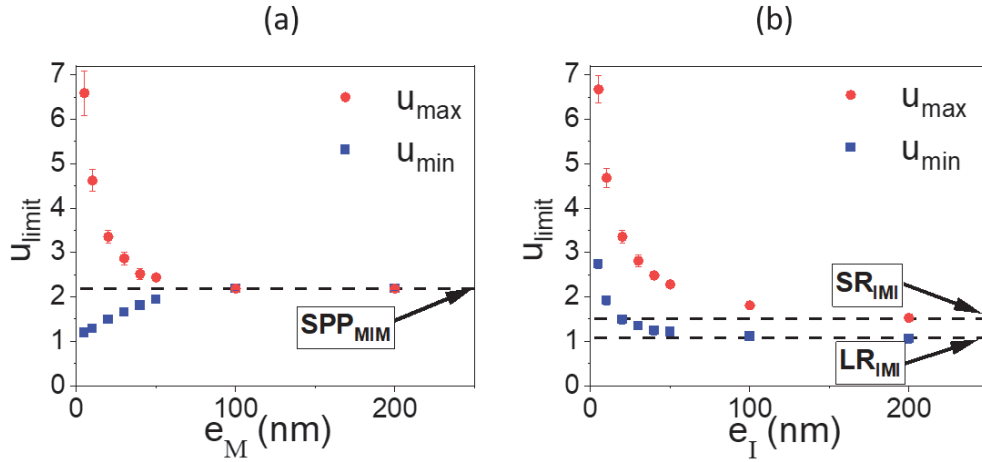


Figure 2.12: **Evolution of asymptotic bounds u_{limit} of the mode continuum.** (a) u_{limit} as function of the metallic thickness e_M (air layers thickness kept to 20nm) and (b), as function of the air thickness e_I (gold layers of 20nm thick).

a coupling strength V . To model this coupling, we used a strong coupling matrix formalism and proposed a schematic diagram in Figure 2.10c, f. We found that the coupling strength between adjacent layers is independent of the number of layers but is directly related to the thicknesses and the indices of the layers, as found for Bragg mirrors. Increasing the number of layers causes a multi-hybridization process and the plasmonic modes merge to construct a continuum similar to the formation of energy bands in a solid. Our result is also valid for the opposite case where the outside layers are made of insulators. The development of this work has many potential applications in plasmonic for architecture design in optoelectronics. More details of this section can be found in [65].

Chapter 3

Experimental methods for Surface Plasmons

We introduce optical techniques used in this Thesis for the investigation of localized surface plasmons (LSPR) in single metallic nanoparticles and de-localized surface plasmons (SPPs) at planar interfaces. The polarization-resolved scattering of the particles is determined by dark-field imaging. We employ Fourier-plane filtering to achieve nearly background-free images. For the planar interfaces, the wavevector-matching condition is necessarily satisfied to launch propagating SPPs, in contrast to LSPR, where its plasmon resonances can be excited by direct light illumination. We present here techniques for increasing the wavevector component of excitation light by means of evanescent waves or scattering from a point source. In terms of detection, the SPPs propagating on the interface are collected by leakage radiation microscopy. The SPPs are characterized by inspecting both Fourier-plane images (k -space) and real-space images. In combination, these experimental methods will be applied to study LSPR of gold bipyramid nanoparticles and gold film in the following chapters.

Contents

3.1	Investigation of the optical response of metallic nanoparticles	71
3.2	Dark-field scattering polarimetry	73
3.2.1	Dark-field imaging by Fourier-plane filtering	73
3.2.2	Single metallic nanoparticle spectroscopy	77
3.2.3	Scattering polarimetry	79
3.3	Exciting and imaging propagating surface plasmon	80
3.4	Launching SPPs by leakage radiation microscopy	84
3.5	Launching SPPs by scattering from a point source	87

3.1 Investigation of the optical response of metallic nanoparticles

The study of localized surface plasmon resonances is not only necessary for the fundamental understanding of the properties of nanoparticles but also for practical applications such as emission enhancement [66, 67] and sensing [68]. The scattering of metallic nanoparticles at a single level can be investigated by means of methods based on near-field and far-field characterizations. Near-field optical microscopy provides information about the optical response, including the local field distribution and the spectrum of plasmon modes [69, 70]. One strategy is to employ a local probe, *e.g.*, fiber tip with an aperture ($\sim 100\text{nm}$), for investigation of the evanescent field of the particle. Because of the complex tip-particle interactions, the near-field methods require a large effort to interpret the results obtained in the far-field and

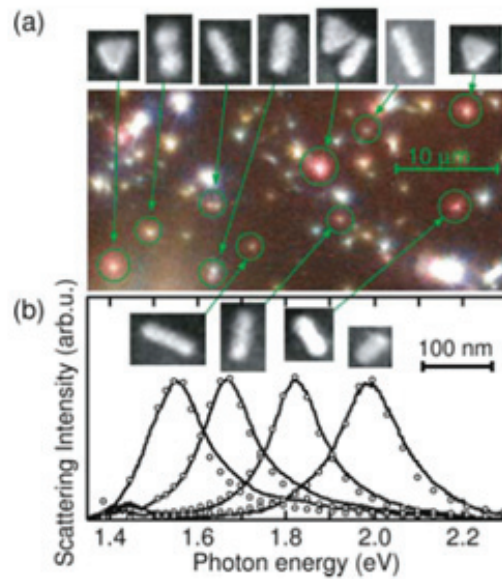


Figure 3.1: **Observation of single gold nanoparticles by dark-field imaging.**(a) Dark-field image together with SEM images.(b) scattering spectra. Source: Kuwata et al.,2003 [71].

thus being limited in spectroscopy and sensing applications.

In dark-field microscopy, scattered light is selectively collected by filtering the incident light away from the detector. Thus, the particles appear in dark-field images as bright spots, induced by scattering, over a dark background. As apposed to near-field microscopy, single-nanoparticle observation in dark-field imaging is only achieved for well-separated nanoparticles. The nearly background-free measurement is usually achieved by using a condenser to construct the illumination in an annular beam and scattered light is collected in a cone of a smaller aperture [71, 72, 59]. Another approach is to locally probe the particles by evanescent waves from a total internal reflection illumination of an interface and scattering collection takes place in the free space of the smaller optical index medium [73]. Due to this simple operation and relatively fast acquisition time, dark field spectroscopy has been widely performed to study scattering of various nanoparticles of different geometry and in different environment. Figure 3.1 shows an example of a dark-field image and corresponding scattering spectra of individual gold nanoparticles [71]. Even under the diffraction limit, the gold nanoparticles of various sizes and shapes enable to distinguish based on their spot color

or spectrum resonance, defined by the resonance wavelength of the localized surface plasmon.

It is worth noting that dark-field spectroscopy or scattering-based techniques are not suitable for very small nano-objects, *e.g.*, few tens nanometers for silver and gold nanospheres, surrounded by a background of scatters. This is due to the fact that the scattering cross-section scales rapidly with the square of particle volume V^2 . Therefore, the scattering of the particles is overwhelmed by the background scattering (low signal-to-noise ratio). On the other hand, absorption is the dominant optical response in this small-size regime, and thus absorption-based techniques are alternatives for sub-10nm nanoparticle detection [74, 75].

In our work, the gold bipyramid nanoparticles (AuBPs) has relatively small volume (equivalent to a sphere of radius ~ 25 nm). However, the bipyramids are able to produce a strong scattering cross-section under resonant excitation due to the large oscillation strength of plasmons along the main axis of the particles (*i.e.*, longitudinal localized surface plasmon resonances). Therefore, we employ dark-field microscopy to measure the scattering spectrum and analyze the polarization of the bipyramids.

3.2 Dark-field scattering polarimetry

3.2.1 Dark-field imaging by Fourier-plane filtering

In order to achieve nearly background-free images for dark-field imaging, our strategy is to discriminate angularly the incident and scattered light by Fourier-plane filtering. Let us first present the principle of the Fourier-plane manipulations. This technique is not only employed to support the measurement of the scattering of localized surface plasmon of the gold nanoparticle but also to characterize the propagating surface plasmon at the planar interfaces.

What is Fourier-plane imaging?

Mathematically, Fourier transform is a function that allows transforming between two reciprocal domains, *e.g.*, the time-temporal frequency or space-spatial frequency domains, by multiplying the input function by an exponential that is linear in phase and making integration. In optics, the two-dimensional Fourier transform of light diffracted from an object can be made by propagating the light at a very large distance or just simply using a

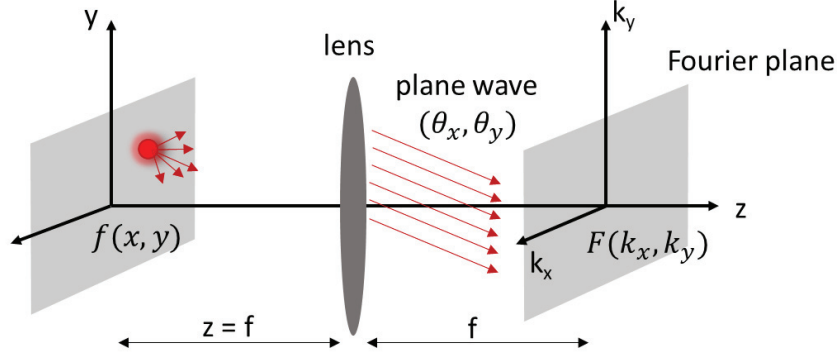


Figure 3.2: **Fourier transform of light by a lens.** Spherical wave produced from one point source at position (x, y) on the object is transformed to plane waves, each moving in a direction (θ_x, θ_y) . Imaging the back focal plane (Fourier-plane) of the lens gives angular distribution of diffracted light.

converging lens. The Fourier transform in the latter case is depicted in Figure 3.2.

The field distribution in the back focal plane (BFP) of the lens ($\tilde{E}(k_x, k_y)$) can be interpreted as a superposition of plane waves or Fourier transform of the diffracted field $E(x, y)$ from the object and is expressed as:

$$\tilde{E}(k_x, k_y, z = f) = \iint E(x, y) \cdot e^{-i(k_x x + k_y y)} dx dy \quad (3.1)$$

We can see that the lens makes Fourier transform light waves from the real space (x, y) to Fourier space defined by wavevectors (k_x, k_y) or angles (θ_x, θ_y) with $\theta_x \approx -x/f$ and $\theta_y \approx -y/f$ (paraxial approximation). If a screen is placed at the BFP, we would image the spatial frequency spectrum (or angular distribution) of diffracted light from the object, the so-called radiation pattern. The Fourier-plane imaging is thus extensively used in nano-optics to access the angular spectrum of propagating radiation. For example, this technique has been used to probe the single fluorescence molecule orientation [76, 77] or measure the directionality of plasmonic antennas [78].

In our work, we image the radiation pattern in the BFP of an inverted oil immersion high numerical aperture objective (Nikon 60x, NA = 1.49). For a light-emitting object deposited on the glass substrate, the objective can collect all radiation confined inside azimuth angle $\theta_{max} \sim 80^\circ$. Figure 3.3a depicts an arbitrary radiated beam is refracted at the surface of the

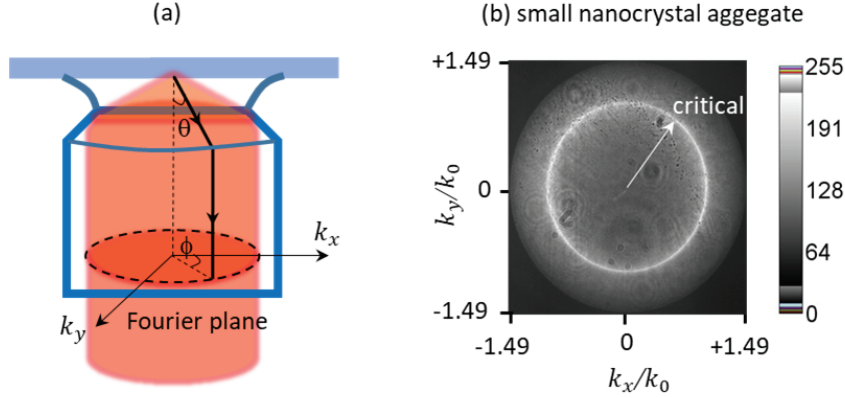


Figure 3.3: **Fourier-plane imaging by a high numerical aperture objective.** (a) Scheme of a radiation collected and projected on the BFP of the objective. (b) Emission diagram of an aggregation of CdSe/CdS nanocrystals in the vicinity to the glass substrate is recorded by an oil immersion objective.

objective and then projected onto the BFP. The spherical angular coordinates (θ, ϕ) of this radiation can be obtained from the polar coordinates $(n \sin \theta, \phi)$ in the BFP, where $n \sim 1.5$ is the refractive index of glass.

The resulting intensity distribution on the Fourier-plane image is related to the radiation pattern by:

$$I_{FP}(k_x, k_y) = I(\theta, \phi) \cdot 1/\cos \theta \quad (3.2)$$

where $I_{FP} \sim |\tilde{E}(k_x, k_y)|^2$ and $k_x/k_0 = n \sin \theta \cos \phi$, $k_y/k_0 = n \sin \theta \sin \phi$. The refracting surface of the objective is approximated as a reference sphere and the apodization factor $1/\cos \theta$ is introduced in order to conserve the energy along each radiation path [39].

As an example, we employ the oil immersion objective to measure the emission diagram of an aggregation of CdSe/CdS nanocrystal deposited on a glass substrate (Figure 3.3b). We refer to the radial coordinate $n \sin \theta$ as the “in-plane wavevector” $k_{||} = \sqrt{k_x^2 + k_y^2}$ of the radiation normalized by k_0 . In the Fourier-plane image, the radius of the upper bound (red circle) corresponds to the maximum collection of the objective (NA = 1.49). A bright circle at $k_{||}/k_0 = 1$ is associated with the critical angle of the total internal reflection (TIR) at the glass/air interface: $\theta_c = \sin^{-1}(1/n) = 41.8^\circ$. The intensity of the radiation pattern peaks at the critical angle is interpreted as the evanescent components of the fluorescence. This field can couple to the far-field radiation beyond the critical angle ($\theta > \theta_c$) when the particle is

placed near the glass substrate [39].

Dark-field imaging by Fourier-plane filtering

Now let us return to our main work where we make manipulations in the Fourier plane to obtain scattering from AuBPs. For a small bipyramid particle size, the localized surface plasmon resonance of AuBPs behaves like a linear radiating dipole. Because of the presence of the interface, the scattering is mostly redirected towards a denser index medium at angles beyond the critical angle of TIR. Therefore, our strategy is to excite the particle in the air and collect its forward scattering in the glass. Figure 3.4 presents the main idea of the measurement: the particle is illuminated in a small aperture and collection takes place in glass by a high numerical aperture objective. The collection consists of both transmitted excitation and forward scattering that mostly distributes at larger angles. The low spatial frequency of the excitation is filtered out of detection by using a beam stop installed in the BFP (or Fourier plane) of the objective. Finally, only scattering of the particle is effectively collected.

In the detection, only a fraction of the total scattered power $P_{sca} = I_{inc} \cdot \sigma_{sca}$ is collected and can be parameterized as:

$$P_{sca}^D = I_{inc} \cdot \iint_D \frac{\partial \sigma_{scat}}{\partial \Omega} d\Omega \quad (3.3)$$

where I_{inc} is the incident intensity and σ_{scat} is the scattering cross-section of the nanoparticle that will be enhanced at LSPR wavelength. The power P_{sca}^D depends on the collection angle of the detector (D) and the radiation pattern of the scattering ($\frac{\partial \sigma_{scat}}{\partial \Omega}$). In which the scattering pattern can be modified by the local environment. For example, in the case of AuBPs placed near an air/glass interface, the scattering is transmitted or reflected by the interface, and thus the scattered power in each medium depends on the Fresnel coefficients.

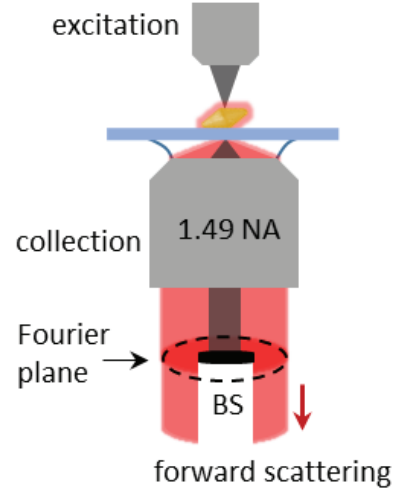


Figure 3.4: Dark-field imaging by Fourier-plane filtering.

3.2.2 Single metallic nanoparticle spectroscopy

Usually, the polarization-resolved fluorescence of single nanoemitters (e.g., dye molecules or nanocrystals) is measured by counting all fluorescent power detected on an avalanche photodiode. For metallic nanoparticles, scattering spectrum is necessarily recorded in order to identify the optical mode for the polarization analysis. The experimental setup for single particle measurements is depicted in Figure 3.5. In general, two excitation channels are possible: from the top (transmission configuration) and/or from the back (reflection configuration) of the collection objective, while there are three detection modes: dark-field imaging, spectroscopy, and Fourier-plane imaging, respectively, all for single particles deposited on a glass substrate.

For the dark-field imaging, we utilize the transmission configuration. The particles are excited by the beam from a fiber-coupled white lamp focused by a 0.25-NA objective. Then, both the scattered light and the direct illumination are collected in transmission by the oil immersion objective (NA = 1.49). The matching refractive indices of the oil and the glass substrate ensure the acquisition of the scattering in a homogeneous medium of index $n \sim 1.5$. As mentioned previously, a beam stop needs to be installed in the Fourier plane of the collection objective in order to block the transmitted excitation. However, it is difficult to access the primary Fourier plane (F.P, Figure 3.5a) because it usually lies inside the objective's body. Therefore, a confocal system is employed to make an image of F.P at position $F'.P'$ (Figure 3.5a). The size of the beam stop is optimized at NA = 0.45 to cut off the low spatial frequency of the direct transmission and retain only the scattered light. It is supported by a thin and homogeneous glass coverslip (thickness $\sim 130\mu m$) so that the phase delay between spatial frequencies can be negligible. In addition, a diaphragm is integrated into the beam stop in order to control the collection numerical aperture. The signal is then recorded by an imaging spectrometer (Andor, Kimera 193i model), *i.e.*, images are captured at the zero order of the grating. Different lenses are performed to switch between the real space (L_r) and the Fourier space (L_F).

Manipulation of the beam stop in the Fourier plane

In order to achieve a nearly background-free image, the position of the beam stop in the secondary Fourier plane $F'.P'$ is adjusted in live-mode imaging. For this, both excitation

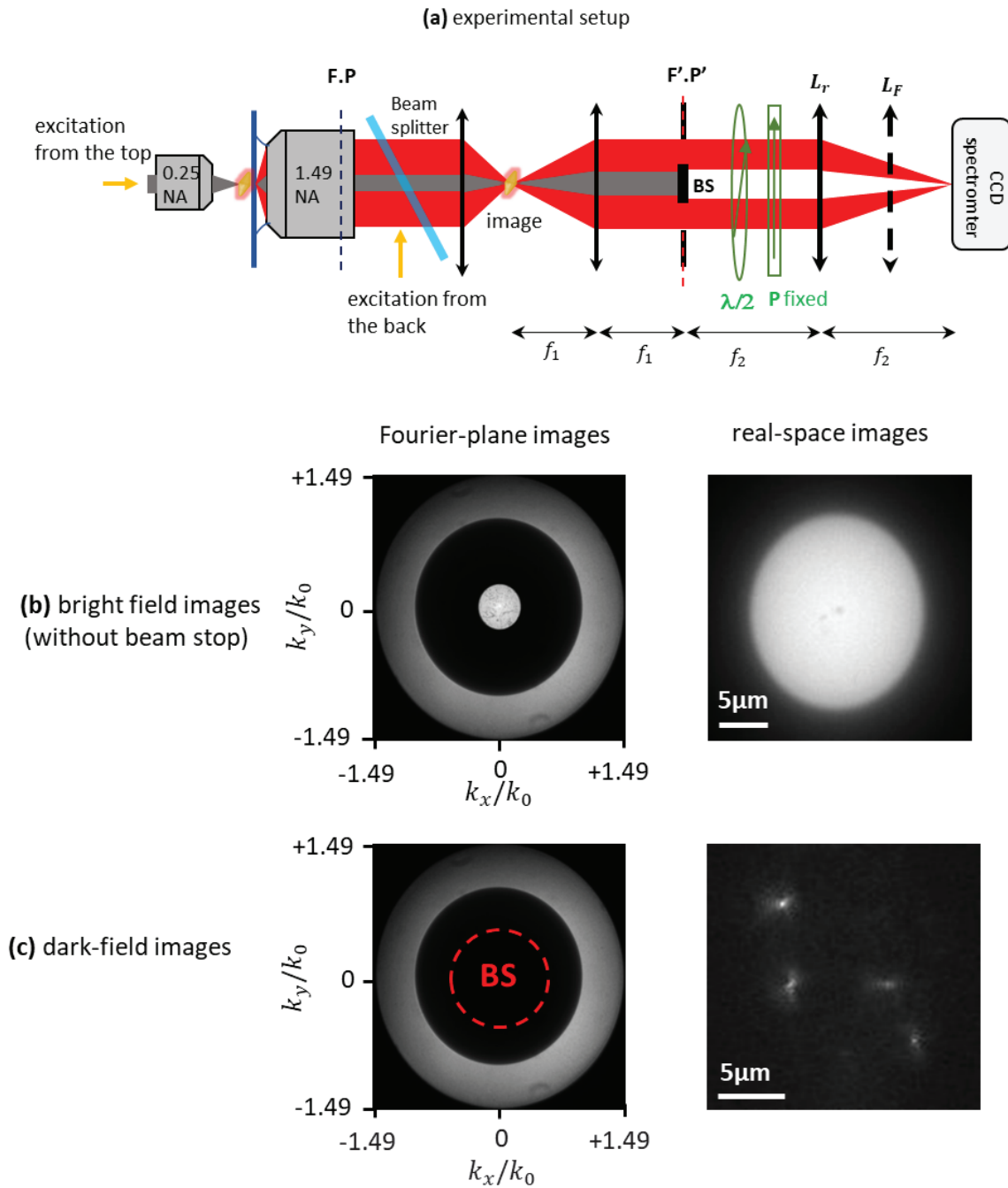


Figure 3.5: **Dark-field imaging and polarization analysis.** (a) Schematic of the experimental setup: F.P: primary Fourier plane of the objective, $F'.P'$: image of the F.P, BS: beam stop, $\lambda/2$: achromatic half-wave plate, P: fixed polarizer, L_r : lens for real-space imaging, L_F : lens for Fourier-plane imaging. (b) and (c) Fourier-plane images and associating real-space images before and after, respectively, the beam stop is introduced to filter the excitation. The bright disk in (b) is associated with the excitation beam.

channels from the top and from the back of the oil objective are performed. The recorded images are shown in Figure 3.5b and c. Angular distribution of the two excitation channels can be observed in the Fourier-plane image (Figure 3.5b, left). The bright disk in the center (radius $k_{||}/k_0 = 0.25$) comes from the direct transmission of the white-lamp incidence, while the rest is the light reflected by the glass substrate when the oil objective is illuminated from the back. We can see a bright two-dimensional ring as the result of the TIR of light beams exceeding the critical angle $\theta_c = 41.8^\circ$ ($k_{||}/k_0 = n \cdot \sin \theta_c = 1$) of the glass/air interface. In this case, the full back focal plane of the objective is illuminated and thus, the radius of Fourier-plane image is limited by $k_{||}/k_0 = NA = 1.49$. In the corresponding real-space image of the bright field (Figure 3.5b, right), we only see the direct image of the excitation beam (induced by the core of the fiber) but not the AuBPs due to the overexposure. However, when the beam stop is introduced in the center of the Fourier-plane image to block the excitation (red-dotted circle, Figure 3.5c, left), we can see that AuBPs appear in the real-space image (Figure 3.5c, right) as well-separated bright spots on the dark background. The particles are then selected individually and sent to the spectrometer. The obtained spectra have a good signal-to-noise ratio because evanescent components of scattering are effectively collected.

3.2.3 Scattering polarimetry

The polarization analysis is then performed by the combination of an achromatic half-wave plate $\lambda/2$ rotating with an angle $\alpha/2$ and a fixed polarizer plate (see Figure 3.5a). The role of the half-wave plate and the polarizer is equivalent to a single rotating polarizer of analysis angle α , however, maintaining a polarization state to enter the spectrometer. Because the polarization analysis will be employed to deduce the 3D orientation of AuBPs later, the polarization devices are necessarily placed in the detection after the oil objective but not in the excitation (polarization analysis of excitation only gives the information about the in-plane angle [79, 80]). It is worth noting that the beam splitter is removed and the dielectric mirrors are alternated by the silver mirrors (if used) to avoid depolarization. A calibration test has been conducted and showed that the depolarization of the overall experimental system is below 3° .

For polarization analysis, the scattering spectra are simultaneously recorded for each

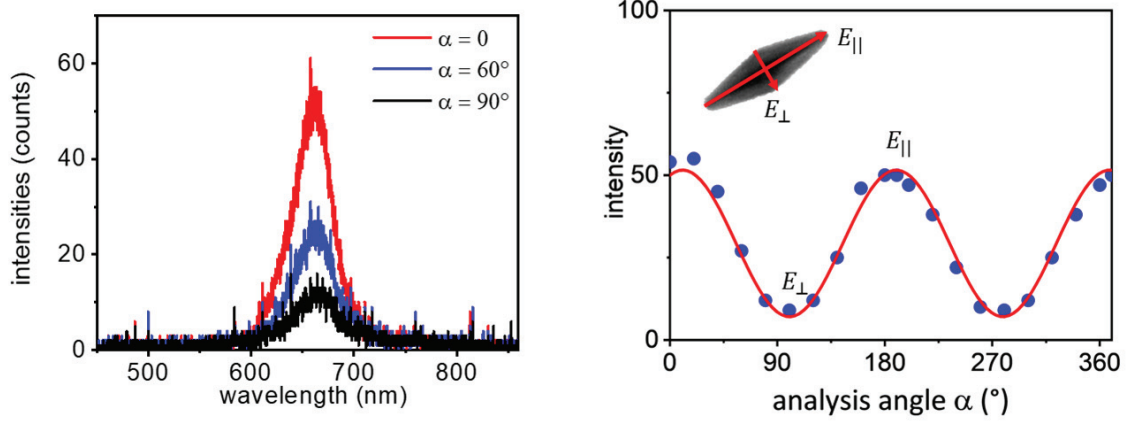


Figure 3.6: **Polarization analysis of scattering.** Scattering spectrum of a single particle is recorded for each analysis angle α . The detected intensities at resonance (blue dots) are plotted as a function of α following the Malus's curve (red line).

rotating angle of the half-wave plate. For instance, Figure 3.6 (left) shows three scattering spectra of a single AuBP respectively recorded for $\alpha = 0$, $\alpha = 60^\circ$, and $\alpha = 90^\circ$. We can see that all the spectra peak at wavelength $\lambda = 670\text{nm}$ associated with the longitudinal LSPR of the AuBP. The intensity at resonance is maximum when the polarizer is in the direction of the longitudinal axis of AuBP (E_{\parallel}) and is minimum in the orthogonal direction (E_{\perp}). For others, the detected intensities oscillate between the maximum and minimum values following the curve of Malus' law (red line, Figure 3.6 right).

3.3 Exciting and imaging propagating surface plasmon

Excitation of propagating surface plasmon polaritons (SPPs)

In order to excite propagating surface plasmon, both energy and momentum conservation are necessarily accomplished. However, for a given energy $h\omega$, the wavevector of SPPs k_{SP} on a dielectric/metal interface is always greater than the wavevector of light k in the dielectric. This can be seen in the SPPs dispersion relation (see Chapter 1) where the SPP dispersion curve lies under the light line (given by $\omega = kc$). Therefore, SPPs excitation by light propagating in free space is not possible unless its in-plane wave vector is increased. There are several ways to achieve the wavevector-matching, including both local SPPs excitation by near-field optical microscopy [81] and macroscopic excitation using a prism or grating

coupling [29, 28, 30], or using spontaneous emission of fluorophores [82, 83]. In this Thesis, the propagating surface plasmon is excited by means of evanescent waves and scattering from a point source.

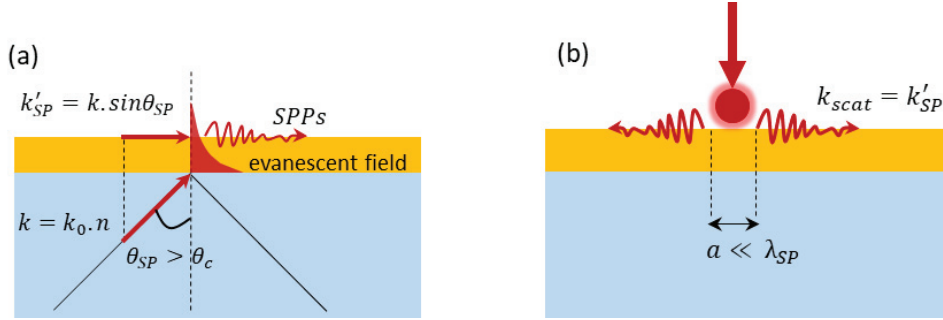


Figure 3.7: **Generation of propagating SPPs.** (a) SPPs of an air/gold interface is generated by evanescent field from glass/gold interface. The incident angle of the excitation beam needs to be higher than critical angle of air/glass interface: $\theta_{SP} > \theta_c$. (b) SPPs excitation by scattering from a small particle ($a \ll \lambda_{SP}$) on the gold surface

SPPs excitation by a Kretschmann configuration: An approach is to excite SPPs of a planar dielectric/ metal interface by means of evanescent waves from another higher refractive index medium that is brought into contact with the metal surface. This is usually known as the Kretschmann configuration [28]. Figure 3.7a shows an example scheme: a thin gold film is sandwiched between air and a glass substrate ($n \sim 1.5$). The wavevector of any light beam propagating inside the glass is always greater than that in the air by a factor of refractive index n ($k = k_0 \cdot n$). Thus, the SPPs at the air/gold interface can be excited by light beams from glass traveling under incident angles θ_{SP} , corresponding to in-plane wavevector equal the real part of the SPPs wavevector: $k'_{SP} = k_0 \cdot n \cdot \sin \theta_{SP}$. The incident angle θ_{SP} is necessarily greater than the critical angle $\theta_c = \sin^{-1}(1/n)$ of the TIR at the air/glass interface. In addition, an effective SPPs excitation is only achieved for critical thicknesses of the metal film (*e.g.*, $\sim 50\text{nm}$ for gold) from which the evanescent wave created at the glass/metal interface can penetrate through the metal layer.

SPPs excitation by near field: The surface plasmon can also be generated by scattered light from a point source whose characteristic dimensions are smaller than the wavelength ($a \ll \lambda$), *e.g.*, surface defects, particles on the surface [82] or structured holes in the metal film [32, 84]. The electromagnetic field can be localized in the near-field regime of the scattered

sources where wavevectors extend beyond the light cone of the propagating wave. Therefore, it is possible to excite the SPPs if the point source is near the interface (Figure 3.7b). Besides, the directivity of the SPPs launching on the interface is defined by the radiation pattern of the point source.

Imaging propagating SPPs by leakage radiation microscopy

The SPPs field propagating along the air/metal interface does not couple to free waves in the air but can be leaked through the metal film and damped into radiation in the glass substrate. This can be interpreted by inspecting the dispersion relations. Figure 3.8 plots the dispersion relations of SPPs and light propagating in free spaces of air ($k_0 = \omega/c$) and a substrate ($k = n.\omega/c$). We can see that the SPP dispersion curve of metal/air interface is always located in the forbidden region of the air light line, and therefore SPPs do not radiate to the free space in the air. However, the radiation loss of SPP into the substrate can appear in a region of the dispersion curve that lies in between the light lines of air and substrate, the so-called “leakage radiation” (Figure 3.8).

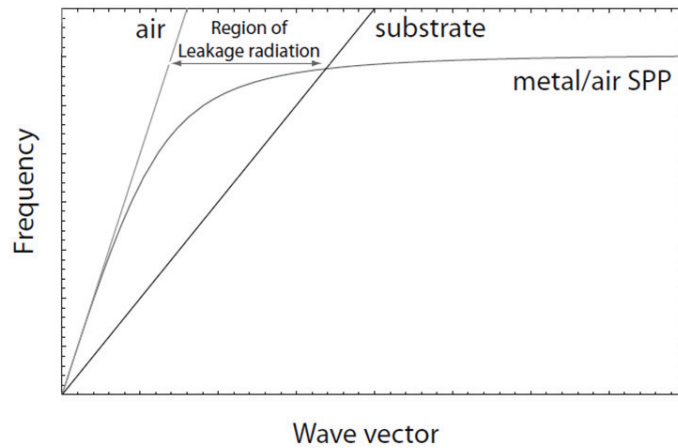


Figure 3.8: **Dispersion relation of SPPs at a metal/air interface.** Region of leakage radiation locates in between light lines of air and substrate. Source: S. Maier [7]

The leakage radiation of SPPs can be collected by using the prism (Kretschmann configuration) or the oil-immersion objective (the index of oil is taken very close to that of the glass). In this Thesis, we employ a high numerical aperture objective ($NA = 1.49$) to investigate the leakage SPPs. There are several advantages of using the objective lens than the prism. Besides allowing tightly focused beams and higher resolution to visualized SPP propagation,

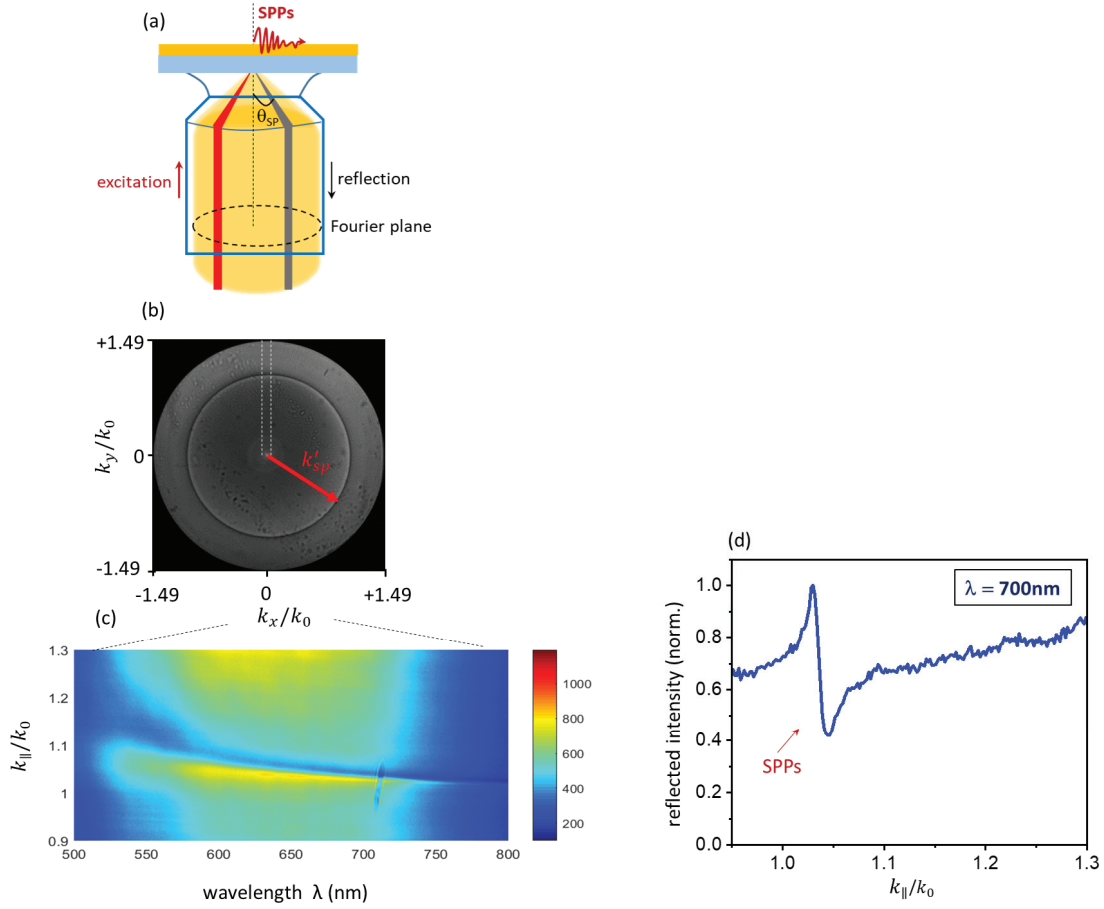


Figure 3.9: **SPPs by leakage radiation microscopy.** (a) Schematic of excitation and collection of SPPs by the oil-immersion objective. (b) A measured Fourier plane where the excited SPPs show their footprint as a dark circle of radius k'_{SP} . (c) Dispersion of selected direction on the Fourier-plane (white lines in (b)). (d) Intensity profile of a vertical line cut on the 2D map of (b) at 700nm. In-plane wavevector $k_{||} = \sqrt{k_x^2 + k_y^2}$

a single acquisition of the SPPs dispersion is possible to obtain in the BFP of the objective that encodes information about the angular distribution of the radiation. On the contrary, the measurement of the SPPs dispersion by the prism in the Kretschmann configuration must be made repeatedly for each excitation angle. In the following, we will use the oil objective to investigate the SPPs launched by the two described techniques using evanescent waves and scattering.

3.4 Launching SPPs by leakage radiation microscopy

Figure 3.9 depicts the excitation and collection of SPPs propagating over an air/gold interface by leakage radiation microscopy. The 45nm-gold is deposited on the glass substrate (thickness $\sim 130\mu m$) and is brought into contact with the oil immersion objective. The objective's back focal plane is completely filled by a white lamp illumination (reflection configuration). For clarity, we only depict the excitation on one side of the objective (Figure 3.9a). For a given wavelength, an associated wavevector fulfilled the wavevector matching condition (red ray) will be responsible for SPPs excitation, whereas others will be reflected or transmitted through the gold film. Therefore, the partial excitation light that excited SPPs will show up as a minimum in the reflectivity (grey ray, Figure 3.9a). The oil objective with $NA = 1.49$ contains all desired angles to excite SPPs corresponding to the white lamp spectrum. All the information related to the angular distribution is encoded inside the Fourier-plane image of the objective in Figure 3.9b. The Fourier-plane image is filled by the reflection of the white lamp on the gold/glass substrate. The dark circle ring is the result of the partial reflection of light after exciting SPPs at the air/gold interface and has a radius proportional to the real part of SPPs wavevector $k'_{SP} = k_0 \cdot n \cdot \sin\theta_{SP}$.

Measuring the SPPs dispersion relation

Each point in the Fourier-plane image encodes information about radiation angles (θ, ϕ) and wavelength λ . In order to obtain the SPPs dispersion $k_{SP}(\lambda)$, we make an image of the Fourier plane onto a vertical entrance slit of the spectrometer and close the slit (width $\sim 100\mu m$) to select one direction of the reflection (white lines Figure 3.9b). An obtained spectra image is shown in Figure 3.9c. This is a two-dimensional map of reflected intensities $I(k_{\parallel}/k_0, \lambda)$. The SPP dispersion can be seen as a dark blue trace above the light line of the air $k_{\parallel} = k_0$ that retrieves all the features of the typical SPP dispersion of a dielectric/metal interface. In the near infrared wavelength region, the SPP propagation constant k'_{SP} is asymptotically approached the light line and bends away when the wavelengths decrease. Besides, the width of the SPP dispersion (which is proportional to the imaginary part of the SPP wavevector k''_{SP}) is broadened when the wavelength is getting smaller, especially where the interband transitions take place (below 550nm).

Identifying SPPs from the reflectivity

We now want to examine the properties SPPs by taking a closer look at the dispersion relation. We select one wavelength on the SPPs dispersion map, $\lambda = 700nm$ for example, and plot the reflected intensity as a function of the in-plane wavevector k_{\parallel}/k_0 in Figure 3.9d. The SPPs is characterized by a dip in reflectivity. As mentioned earlier, this missing light can be interpreted as a conversion to the SPPs which carry away the energy along the interface so that it cannot reach the spectrometer. Therefore, the full width at half maximum Γ_{SP} of the dip is contributed by all the losses of the SPPs excited at the air/ gold interface and can be expressed as:

$$\Gamma_{SP} = \Gamma_{abs} + \Gamma_{LK} + \Gamma_{scat} \quad (3.4)$$

where Γ_{abs} is Ohmic damping caused by the absorption of metal; Γ_{LK} is the leakage radiation into glass substrate that depends on thickness of metallic film; and Γ_{scat} is damping caused by the surface roughness of the metallic surface. If the surface roughness is neglected ($\Gamma_{scat} = 0$), the reflection coefficient in the region of the resonance can be approximated as a Lorentzian function

$$R = 1 - \frac{4\Gamma_{LK}\Gamma_{abs}}{[k_{SP} - (k_{SP}^{(0)} + \Delta k_{SP})]^2 + (\Gamma_{abs} + \Gamma_{LK})^2} \quad (3.5)$$

The formula is obtained from [7] where the calculation is based on the Fresnel coefficients. In which, $k_{SP}^{(0)}$ is the wavevector of SPPs propagating along the interface of two infinite media air/metallic. This is not equal, but is shifted by Δk_{SP} from the wavevector k_{SP} of SPPs of the air/metal/glass system due to the finite thickness of metallic film and the leakage radiation of SPPs into glass substrate. From the formula, it is apparent that a zero reflectivity can be achieved for a critical metal film thickness that allows $\Gamma_{LK} = \Gamma_{abs}$. At this thickness, there is also a perfect destructive interference between the reflected light and the leakage radiation of SPPs [7, 39].

Usually, the complex value of k_{SP} can be obtained by fitting the reflected curve with the Lorentzian function. In our experimental situation, this is not straightforward because the reflected curve of SPPs dose not really have a well-defined shape due to a low efficiency of SPP excitation. This is because of the fact that only small proportion of the white-lamp incidence is responsible for SPPs excitation when the full back focal plane of the objective is

illuminated. A more efficient way to excite SPPs can be achieved by using an off-axis laser beam to locally excite SPPs around angles associated with k_{SP} . The highly focused laser beam also allows for an excitation in a diffraction-limited spot area and thus the propagation length of SPPs can be measured directly in the real-space image. Moreover, the excitation of a continuum of SPPs at different wavelengths is possible by using a white-light continuum laser. The SPPs dispersion appears as a rainbow jet in the Fourier-plane image [85].

Measuring dielectric film thickness by SPP dispersion

As shown above, leakage radiation microscopy using white lamp for excitation is not efficient and accurate to determine characteristics of SPPs at given excited wavelength (e.g., decay length, wavevector). However, because the measurement allows to retrieve the dispersion of SPPs, it can be useful for tracing the change of optical index of the near environment: a thin dielectric film deposited on gold film for example.

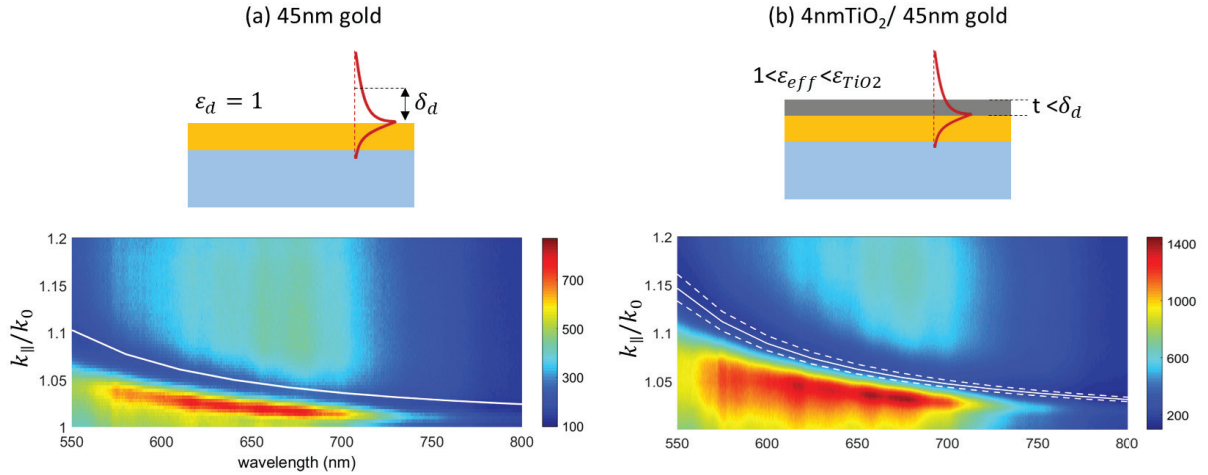


Figure 3.10: **Dispersion relation of SPPs at different interfaces.** (a) air ($\varepsilon_d = 1$)/45nm gold film and (b) air/4nm-TiO₂ ($\varepsilon_{TiO_2} = 2.4$)/45nm gold film. ε_{eff} is an effective index of air and thin TiO₂. White lines is the simulation of SPP dispersion where dotted lines is simulated for $t = 3\text{nm}$ and $t = 5\text{nm}$.

Figure 3.10 show SPP dispersion measured by leakage radiation microscope for two kind of films: (a) bare gold film in air and (b) 4nm-TiO₂ deposited on gold film. We can see that the dispersion curve of the latter is shifted to higher $k_{||}$ as compared to the bare gold film. This happens at all the wavelength of experimental window; however, is more significant in the lower wavelengths. Besides, the centre (or the dip where reflection is minimum) of the

measured dispersion is well-followed the simulated curves (solid white lines). Changing the TiO₂ film thickness by $t \pm 1$ nm already shows the visible shift of the SPP dispersion (dotted white lines). Therefore, this measurement allows us to determined nanometric-scale thickness of thin films with 1nm of precision. Here, the thin film induces the changing of the optical index at interface, which leads to shift SPP dispersion following $k_{SP} = k_0 \cdot \sqrt{(\varepsilon_d \varepsilon_m) / (\varepsilon_d + \varepsilon_m)}$. In the case of air/gold interface, ε_d is equal to the refractive index of air $\varepsilon_d = 1$. When thin TiO₂ film is deposited, now the the optical index of above surface can be considered as a mixing of air and TiO₂, which is called effective index ε_{eff} . Therefore, now it is similar a single interface between a dielectric medium of $\varepsilon_d = \varepsilon_{eff}$ and gold. This is still true as long as the TiO₂ thickness is sufficient smaller than the evanescent decay length of SPPs in the air $t < \delta_d$. The shift of SPP dispersion presented here is also the mechanism behind sensing applications based on surface plamson.

3.5 Launching SPPs by scattering from a point source

The increase of the free-space wavevector to excite SPPs can be achieved by means of scattering from a subwavelength point source such as defects or structured ridge on the metallic surface. For example, we use non-absorbing silica bead nanoparticles to excite SPPs of the air/gold interface. The beads have an average diameter of 150nm and refractive index ~ 1.5 , and are deposited separately on the 45nm-gold film. A simplified experimental scheme is drawn in Figure3.11a where the bead is excited by a focused laser beam ($\lambda = 650nm$) and the leakage radiation is collected by the oil immersion objective. The beam stop is also installed in the Fourier plane to block the transmitted laser beam.

When the bead is excited by the laser, any scattered light satisfies the wavevector-matching condition is responsible for generation of SPPs. The SPPs are then leaked into glass substrate and appears in the Fourier-plane image as a bright circle. Figure3.11b show an example of a Fourier-plane image which is measured by the experimental scheme on the left. Here, the radius of the red ring is proportional to $k'_{SP} = k_0 \cdot n \cdot \sin \theta_{SP}$, which is just above $k_{||} = k_0$. Because only partial scattering involves the SPPs excitation, the Fourier-plane image can be interpreted as a superposition of the SPPs leakage radiation and the

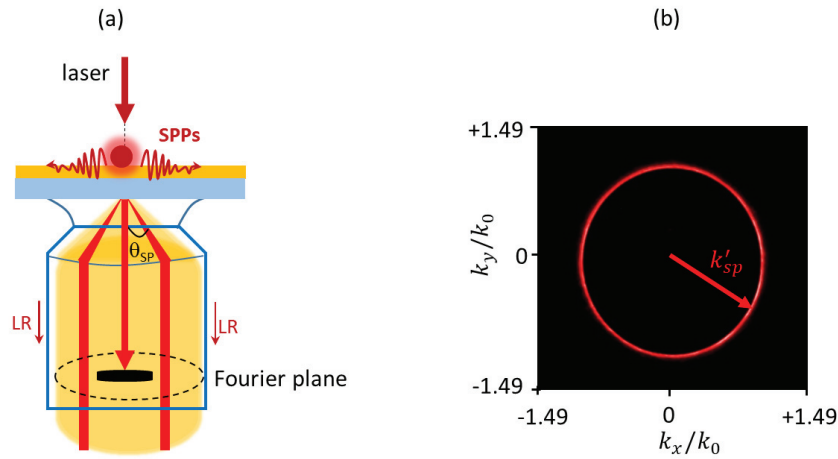


Figure 3.11: **Launching SPPs by scattering from a nanobead.** (a) Schematic of experimental setup. The particle is excited by a 650nm-laser. LR is the leakage of SPPs. Black disk is a beam stop, which is used to block the transmission of the laser (b) A measured Fourier plane where the leakage SPPs show their footprint as a bright red circle of radius k'_{SP} .

background scattering. Here, we can see that the contribution of SPPs is dominant due to its confinement characteristic, while the background scattering is negligible.

Chapter 4

Measuring the 3D Orientation of Single Gold Bipyramid Nanoparticle

Similarly to the elongated nanoparticles, the field enhancement around the gold bipyramid nanoparticles (AuBPs) also displays high anisotropy. A simulation shows that this enhancement is strongest near end tips along the longitudinal axis of the AuBPs and is about 25 times greater than a sphere [5]. This is so-called longitudinal surface plasmon resonance (LSPR) which is mostly sensitive to the local environment at the vicinity of the tips. Thus, in the case of a AuBP on a high index or an absorbing substrate, e.g., a gold mirror, how the particle lies on the surface plays an important role. Furthermore, the knowledge of the nanoparticle orientation is required to maximize the desired properties for many applications. Among them, we can cite dipolar interactions and directional scattering. For instance, color routing has been achieved by manipulating the scattering diagram of two interacting metallic nanoparticles [86, 87]. Another wide range of examples may be found in controlling the spontaneous emission of single emitters with nanoparticles by tailoring their local electromagnetic environment with applications in nanoantennas [88, 66], light-emitting devices, Raman spectroscopy, and biosensors. It is then crucial that the emitter and the metallic nanoparticles are well aligned in order to maximize their coupling.

In this Chapter, the 3D orientation of a single AuBP is determined by plasmon-resonant scattering polarimetry. The AuBPs are deposited on a glass substrate in order to avoid any significant orientation-induced effects such as an LSPR shift or the appearance of new modes. Here, we develop a technique to precisely control the collection angle by Fourier-plane filtering of the scattering. The crucial role of the collection numerical aperture is also studied and discussed thoroughly.

Contents

4.1	Properties of Gold Bipyramid nanoparticles	90
4.2	Scattering polarimetry for orientation measurement	93
4.3	Orientation of the AuBPs on the glass substrate	97
4.4	Role of collection numerical aperture	99
4.5	Conclusion	104

4.1 Properties of Gold Bipyramid nanoparticles

The synthesis procedure of the AuBPs used in this work has been described previously [89, 90]. Briefly, the nanoparticles are produced by a colloidal seeded growth method. The bipyramid anisotropic growth is controlled by adjusting the amount of gold salt and the nature of the reductant, surfactant and structural agent. Eventually, this method produces water-soluble AuBPs stabilized by a bilayer of cetyltrimethylammonium bromide (CTAB) that prevents the particles from aggregation.

The morphology of the bipyramids has been studied by a transmission electron microscope (TEM) (Fig 4.1). The AuBPs with sizes deduced from the TEM images have an average length $L=70\text{nm}$ and width $W=25\text{nm}$ with rounded tips and edges (rounding radius $r=5\text{nm}$). However, the real sizes might be different from these measured values by 5 - 10% depending on the orientations of the AuBPs which is due to the fact that the TEM gives 2D projections of the particles. Moreover, the precise shape of the AuBPs is also observed in 3D electron tomography, a technique that reconstructs the volume of particles from a series of 2D projection TEM images recorded at different angles. The reconstruction from the 3D-electron-tomography images (Fig 4.1c) shows that the AuBPs are twisted at the middle with 5 triangular facets on each pyramidal half.

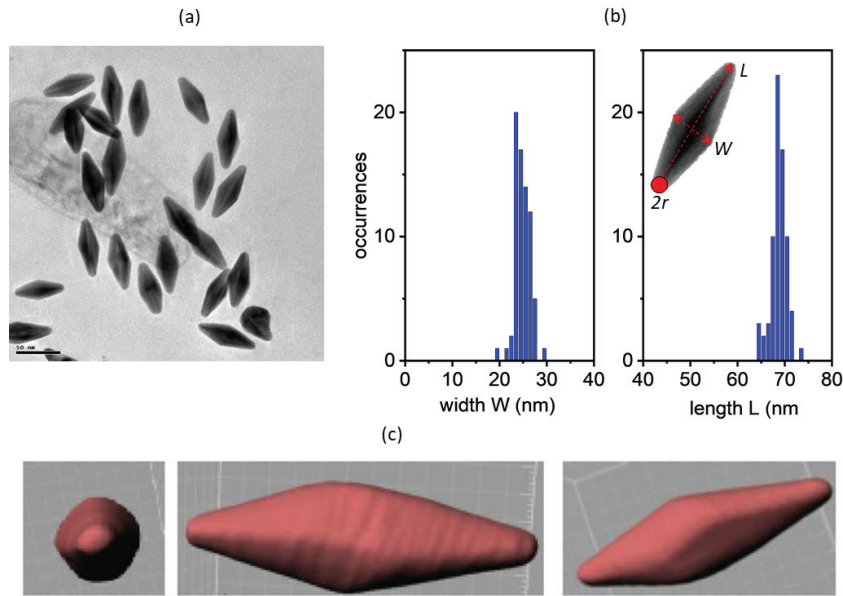


Figure 4.1: **Morphology of the AuBPs.**(a) TEM image of the AuBPs.(b) Distributions of the length L and width W measured on the TEM images, r denotes for a rounding radius of the tips green(c) 3D shape of a AuBP reconstructed from tomographic TEM.

The optical response of the AuBPs is studied by both ensemble measurement and at the individual level. The UV-visible spectrum of the bipyramid suspensions (Fig4.2) shows two distinct peaks: (i) a broad band around 500-600 nm associated with the transverse LSPR and (ii) a more intense and narrow band at the near infra-red region (750-1050 nm) attributed to longitudinal LSPR of the AuBPs. The bi-products (spheres or nanorods) might contribute to these resonances, but only a small proportion (around 5% [89]). For different sample preparations in Fig 4.2, the wavelength at which the longitudinal LSPR occurs can be tuned by changing the size and aspect ratio of the AuBPs. However, controlling the aspect ratio is more favorable because increasing the size of a particle leads to broadening of the resonance that is mostly caused by multipolar excitations [89].

At a single particle level, the scattering spectrum of a AuBP on a glass substrate is stimulated by COMSOL and measured by dark-field spectroscopy (Fig 4.3). In the calculation, the particle is excited by an unpolarized plane wave in a normal incidence. We can see that the simulated spectrum is dominated by an intense band centered at 740nm associated with the longitudinal LSPR. The charge distribution of this mode (inset, Fig4.3a) shows the strong localization around the tips of the bipyramid, which resembles an induced dipole. On

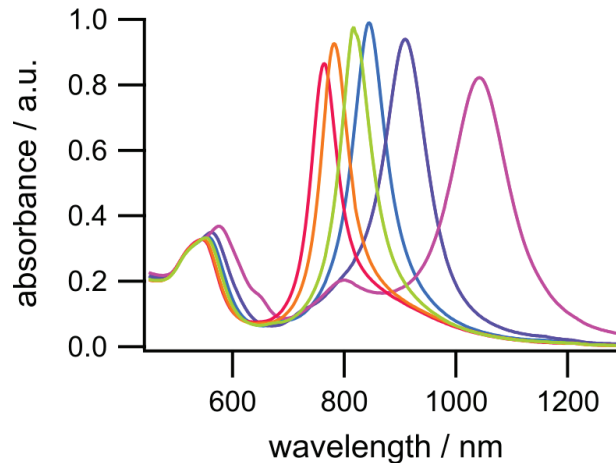


Figure 4.2: **Optical study on ensembles of biyramids:** UV-visible spectra of different suspensions of the AuBPs. Source: Navarro et al [90].

the contrary, the quadrupolar mode is also excited at around 580 nm, however, this mode weakly scattered light because of its zero net dipole moment. Interestingly, a small resonance that arises at 650 nm is the result of hybridization between the radiating dipolar and the non-radiating quadrupolar modes. This interaction is mediated by the substrate and therefore, only appears when the AuBPs have a facet contact with the surface. In addition, the hybridization is more significant if the particles are deposited on the higher optical substrate [91, 92]. At the single particle level, the transverse LSPR yields virtually non-contribution to the scattering cross-section due to its very weak dipolar moment and strongly damping by the interband transitions (below 550 nm) [11, 9].

The dark-field spectroscopy ¹ is performed to retrieve almost the forward-scattering of each individual AuBP and a scattering spectrum is shown in Fig 4.3b. We can see that only the longitudinal LSPR shows up as a well-defined line while the other modes are vanished due to the too weak signal-to-noise ratio. The spectrum follows very well the Lorentzian fit (red curve) centered at 700nm with narrow full width at a half-maximum (FWHM) of 40nm. This value is equivalent to a resonator with quality factor $Q \sim 20$, suggesting that the AuBPs can be used as plasmonic probes with a good Q factor that is very beneficial for sensing applications [5, 75].

¹see Chapter 3

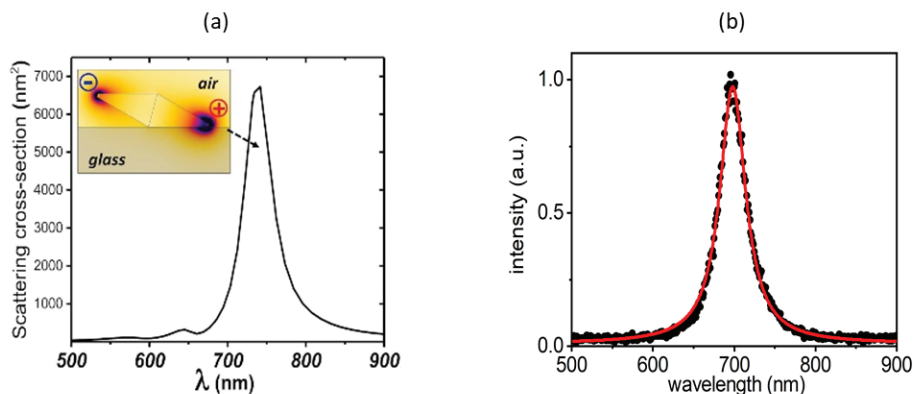


Figure 4.3: **Optical studies of the AuBPs at a single level.** (a) Numerical simulations of scattering spectrum of a AuBP on the glass substrate excited by a unpolarized plane wave. Inset: charge distribution associated with the main resonance (720nm). (b) Scattering spectrum measured by the dark-field spectroscopy (black dots) and fitted with the Lorentzian function.

4.2 Scattering polarimetry for orientation measurement

In general, the orientation of a single nanoparticle is obtained experimentally from their radiation pattern or by polarization analysis. First, we briefly review the principles of the conventional methods for the determination of orientation, with possible applications.

Methods of emission orientation determination

Fourier-plane imaging: the emission of the nano-object is directly encoded in the radiation pattern that can be accessed by imaging the intensity distribution in the objective's back focal plane (Fourier plane). This method has been applied to measure the orientation of various materials, including nanocrystals [93, 94], fluorescent molecules [77], or gold nanoparticles [59, 92]. Besides orientation, the emission Fourier plane image is able to discriminate the dipole dimensions of the emitter [76]. However, this method usually requires very sensitive detectors and a large number of photons to obtain a sufficient signal-to-noise ratio.

Defocused imaging: by just a slight displacement of an objective out of its focal plane, the defocused patterns on the recorded images can be used to retrieve the orientations of the object [95, 96]. This method offers a very convenient implementation but its precision is very sensitive to the alignment and aberrations of the experiment setup.

Focused orientation and position imaging (FOPI): the core idea is to place the particles on an absorbing substrate, e.g. gold, to enhance the vertical dipolar component of the object inducing a focused doughnut-shape image [97]. The 3D orientations are extracted from this image without angular degeneracy.

Anisotropy measurement: determine the in-plane orientation by using a polarization beam splitter to separate optical responses of nano-objects into two orthogonal polarization directions to measure the optical anisotropy. This method is commonly used to measure the orientation of dynamic nanoparticles in biological solutions [98]. Besides, it also allows for determining the dipole dimension of nano-objects.

Emission polarization analysis: emission polarization is analyzed by continuously rotating a polarizer placed on the emission path. The 3D orientations are extracted from the detected intensity as a function of rotating angles. This method allows for determining the orientation of the emitter in situations, e.g. in proximity to a gold film, for which the radiation pattern-based techniques are not sufficiently sensitive [79, 76].

Theoretical framework of scattering polarization analysis

In our study, we determine the orientations of a single AuBP by polarization analysis of its longitudinal LSPR scattering. While the scattered light is effectively collected by Fourier-plane filtering in the dark-field imaging (see Chapter 3), the measurement and the analytical model of the polarization analysis are suggested from the emission polarization analysis [79, 99]. This technique has been successfully applied to determine the 3D orientation of a permanent dipole inside semiconductor nanocrystals [76] or fluorescent molecules [100]. In our work, we are also able to use this method to measure orientations of the induced dipole associated with the longitudinal LSPR, which is equivalent to the orientation of the AuBPs. In the following, we present a brief description of the theoretical modeling used in this study to interpret the data and extract the 3D orientation of a AuBP. A more comprehensive calculation of the different environments can be found in this Ph.D. thesis [80].

To illustrate the relation between the orientation of a dipole and its polarization, we consider the simple case of a linear dipole radiating in a homogeneous medium. The 3D orientation is defined by an in-plane angle Φ and an out-of-plane angle Θ as shown in Fig4.4a.

The emission of the dipole is collected by an objective and then analyzed by a polarizer that continuously rotates with an analysis angle α . The radiation of the dipole in each direction is characterized by its emission diagram, which spreads mostly in the transverse directions to the dipole axis and there is no radiation at all in the direction of the dipole. We can see in Fig4.4 that the collected emission by the objective is strongly polarized for the horizontal dipole $\Theta = 90^\circ$ (opposite for the vertical dipole $\Theta = 0$).

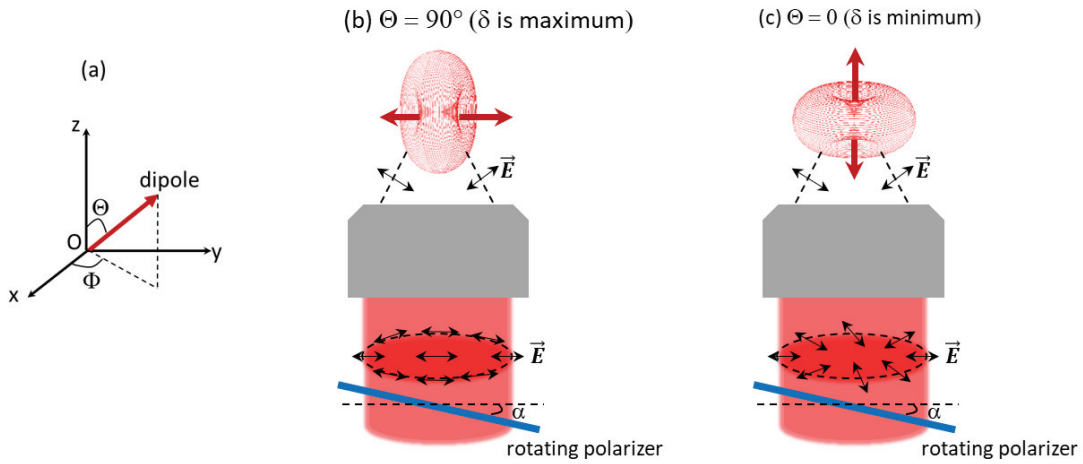


Figure 4.4: **Schematic of a simulated situation of a dipole radiating in a homogeneous medium.** (a) 3D orientation of the dipole is defined by angles (Θ, Φ) . Emission diagram of a horizontal dipole (b) and a vertical dipole (c) is collected by an objective and analyzed by a rotating polarizer (α is the analysis angle).

The model calculates the sum of the emission polarization along each propagation direction that has taken into account the apodization factor of the objective. Ultimately, the in-plane dipole orientation Φ can be extracted from the dependence of the polarized intensity I as a function of the analysis angle α :

$$I(\alpha) = I_{min} + (I_{max} - I_{min}) \cdot \cos^2(\Phi - \alpha), \quad (4.1)$$

This equation shows that the emission intensity is partially polarized, with a Malus component in the square-cosine function. On the other hand, the out-of-plane orientation Θ defines the contrast between the maximum and minimum values of the detected intensities

and therefore can be deduced from the measured degree of polarization (DOP) δ :

$$\delta = \frac{I_{max} - I_{min}}{I_{max} + I_{min}} \quad (4.2)$$

For example, vertical and horizontal dipoles induces strongest polarization and depolarization, respectively, and thus, δ is maximum for $\Theta = 90^\circ$ and is minimum for $\Theta = 0$ (Fig 4.4).

It is important to note that $I(\alpha)$ and δ are parameterized with the following values:

- The dipolar dimension of the nanoparticles, e.g. 1D dipole - a linear radiating dipole (nanorod [101]), 2D dipole - an incoherent sum of two orthogonal 1D dipoles (dot-in-plate [76]), or 3D dipole - an incoherent sum of three 1D dipoles (isotropic emitters).
- The collection numerical aperture of the objective.
- The environment close to the dipole, e.g. optical index or interface.

In the case of the AuBPs, the simulated situation is depicted in Fig 4.5. The emitter is located in the air near a glass interface (refractive index $n \sim 1.5$) described as a semi-infinite medium. Given the emitter's length $L = 70$ nm (average size of the AuBPs deduced from the TEM images), the scattering AuBP is modeled as a point-like dipole located at a distance $z = (70/2) \cdot \cos\Theta$ (nm) from the glass surface. The emission of the dipole is collected by an oil immersion objective ($NA = 1.49$), a minor part of the collected light is cut off by a beam stop ($NA_{bs} = 0.45$) placed at the Fourier-plane of the objective, and then analyzed by a polarizer that is continuously rotated with an analysis angle α .

For this situation, the calculation has to take into account the transmission and redirection of the emission at the air-glass interface. Besides, the sums of the emission inside a solid angle of collection is limited by the beam stop ($\theta_{min} = \text{asin}(NA_{bs}/n)$) and the objective numerical aperture ($\theta_{max} = \text{asin}(1.49/n)$).

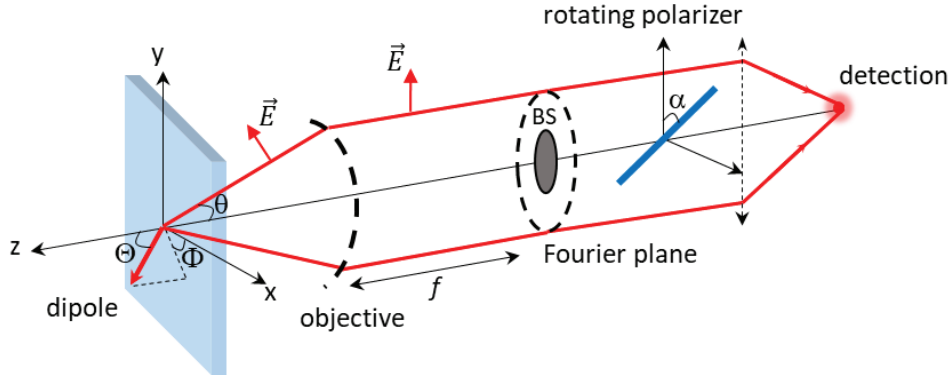


Figure 4.5: **Schematic of a simulated situation of associated with the AuBPs.** The bipyramid is modeled as a linear dipole at a vicinity to a glass substrate. Off-axis angle θ related to the collection angle. BS denotes for a beam stop.

4.3 Orientation of the AuBPs on the glass substrate

In this section, we apply the described scattering polarization analysis to measure the orientations of the AuBPs. The sample is prepared by drop-casting the AuBPs solution on a clean glass substrate without any specific surface treatment or controlling the orientation. The concentration of the AuBPs has been adjusted to display well-separated nanoparticles (around 1 AuBP per $50\mu\text{m}^2$). The experimental configuration of the dark-field imaging and polarization analysis has been depicted in the Chapter 3. In the following, the procedure to measure the 3D orientations of an individual AuBP is presented first, then this measurement of the out-of-plane angle is repeated for other AuBPs to obtain the orientation distribution.

Determination of the 3D orientation of a single AuBP

We plot on Fig 4.6a the dependence of the scattering intensity on the analysis angle α . The measured intensity oscillates between I_{max} and I_{min} (red dots) with a square-cosine dependence in good agreement with Eq 4.1. This fit (blue line) gives $\Phi = 30^\circ$ and $\delta = 0.72$.

Alternatively, the values I_{max} and I_{min} can be obtained directly by looking for the maximum and minimum of the scattering spectrum. Such spectra of a single AuBP are shown in Fig 4.6b. For this AuBP, we have a resonance at 670nm with a narrow FWHM of 40nm. This resonance is attributed to the longitudinal LSRP mode. Using Eq 4.2, we calculate that $\delta = 0.7$ for this particle, which is different by only 3% from δ extracted from the Malus dependence in Fig 4.6a. Therefore, for our following measurements, δ will be simply deter-

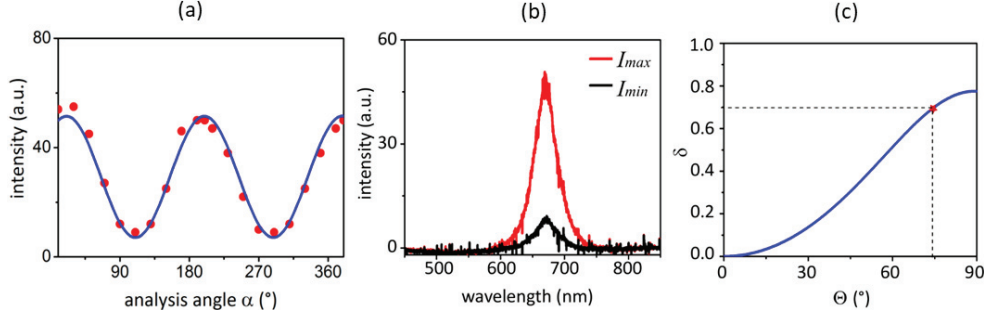


Figure 4.6: **Polarimetric measurement of an isolated AuBP.** (a) The intensity of the scattering spectra as a function of the analysis angle α . The red dots are the experimental measurements. The blue line corresponds to the fit with Eq 4.1. (b) Scattering spectra for two orthogonal polarizations corresponding to maximum (I_{max}) and minimum (I_{min}) intensities. (c) Theoretical dependence of δ on the dipole orientation Θ . The dashed line represents the experimental δ extracted from (b).

mined by taking I_{max} and I_{min} on the scattering spectrum. Once δ is known, Θ is determined from the theoretical dependence $\delta(\Theta)$ [77, 80] as presented in Fig 4.6c that gives $\Theta = 75^\circ$.

Statistical orientation Θ of the AuBPs

In the above section, we gave a description about the procedure to measure 3D orientation for one bipyramid by scattering polarization analysis. In the following, we present a statistical measurement of the out-of-plane angle θ . This angle is the important parameter that might lead to different interaction between the AuBPs and the substrate.

We perform the same measurement of δ for a selection of 30 AuBPs. Fig 4.7a presents the result as a distribution of δ between 0.5 – 0.8. By using the theoretical curve of $\delta(\Theta)$ reported previously, we deduce out-of-plane orientation Θ and report its histogram in Fig 4.7b. These values might be directly linked to the specific geometry of the AuBPs. We, therefore, calculate a geometrical orientation

$$\Theta_{contact} = \frac{\pi}{2} - \tan^{-1} \frac{W - 2r}{L - 2r} \quad (4.3)$$

which is associated with the cases from which a facet of the AuBPs touches the surface, with the widths W , the lengths L , and the rounding radius r deduced from the TEM images, and plot the distribution in Fig 4.7c. Both angular histograms display a peak at around 75° , but the extension of the wings on either side of this peak is larger by 15° for the polarization

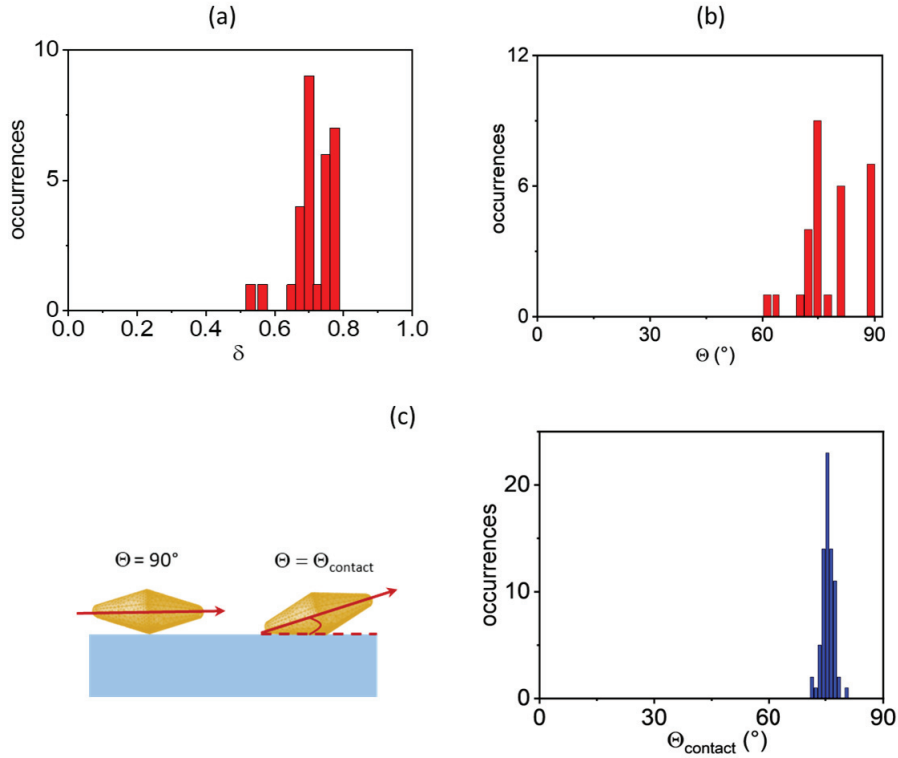


Figure 4.7: **Orientation distribution of the deposited AuBPs on the glass substrate.** (a) Histograms of measured δ and (b) deduced orientations Θ , for 30 AuBPs by the polarization analysis. (c) Illustration of orientations when a AuBP is horizontal ($\Theta = 90^\circ$) or touches the surface (Θ_{contact}), and histogram of Θ_{contact} is calculated from the TEM images.

analysis. Especially, many AuBPs are measured depositing parallel to the substrate ($\Theta = 90^\circ$). This orientation might be induced by the stabilizer surrounding the AuBPs (CTAB, $\sim 2\text{nm}$ [89]) or the surface roughness of the glass ($\sim 3\text{nm}$, measured by profilometer). However, these side factors do not introduce any unpredictable orientations as we did not find any particle with $\Theta < 60^\circ$. These angles are observed in the previous study [5, 102] on the AFM image, but for the case of overlapping of two AuBPs. However, the dark-field scattering spectrum allows us to identify whether the object is a single AuBP or an aggregation.

4.4 Role of collection numerical aperture

The previous theoretical analysis [99] stated the important role of the collection numerical aperture (NA) in the interpretation of experimental values of δ . Fig 4.8 demonstrates how

the curve $\delta(\Theta)$ is significantly varied when different NA objective is used. This is due to the fact that the emission of a 1D dipole into a specific direction is always polarized and thus, different collection NA results in different values of δ . In this section, the relation between δ and collection NA is investigated experimentally, providing deep insights to the polarization analysis: (i) another way to measure orientation with higher certainty, and (ii) the choice of an optimal collection objective for the measurement.

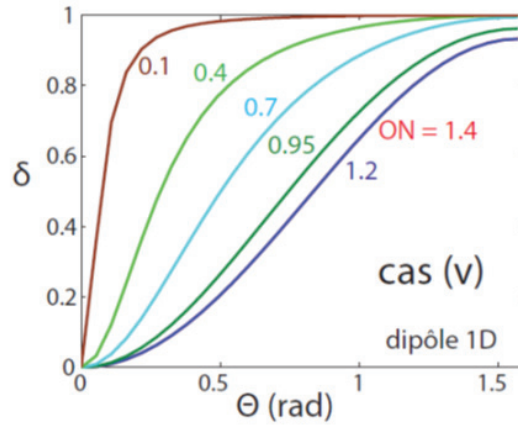


Figure 4.8: Theoretical calculation of $\delta(\Theta)$ for 1D dipole with different collection NA (ON: overture numerique), calculated in a situation when the dipole is located in the air, near a glass surface, and without presence of a beam stop. Source: PhD thesis of C. Lethiec [80]

The dependence of δ on the collection NA

To change the collection NA, we set a diaphragm at the secondary Fourier-plane position together with the beam stop (see Chapter 3) as shown in Fig (Chap 3). We, therefore, study δ as a function of NA for $NA \in [0.45; 1.49]$. Fig 4.9a presents the determination of δ for 5 values of NA on the same AuBP. For each diaphragm radius (corresponding to a specific NA), we measured δ as previously explained (see Fig 4.6). Because, the decrease of the collection NA means fewer emission is collected, we also measure the evolution of the scattering maximum intensity I_{max} with NA. The experimental results agree well with a theoretical fit (solid lines). These calculations have taken into account the presence of the beam stop at $NA = 0.45$. If we omit the presence of the beam stop and integrate over all collected angles down to $\theta = 0$, only a slight difference is observed (dash line in Fig 4.9b) because most of the scattering occurs above the critical reflection angle $\theta_c = \sin^{-1}(1/n)$. This confirms that the polarization analysis protocol is not fundamentally modified by working in the dark-field

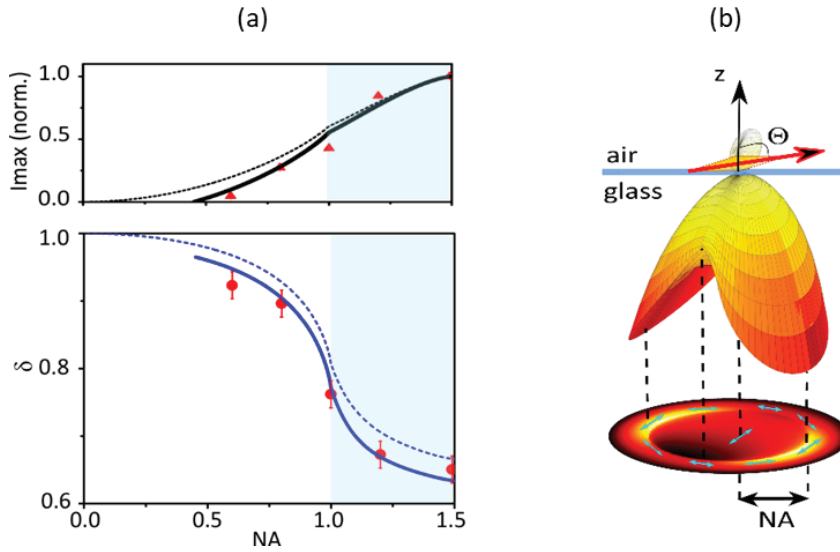


Figure 4.9: **Evolution of the polarization measurement as a function of the objective numerical aperture.** (a) δ and normalized maximum intensity I_{max} . Red dots are experimental measurements on the same single AuBP. The lines show two cases of theoretical calculations: $NA \in [0.45; 1.49]$ with a 0.45-NA beam stop (solid lines) and $NA \in [0; 1.49]$ without any beam stop (dashed lines). The blue zone corresponds to radiation directions above the critical angle. (b) Simulated scattering diagram and its projection on the Fourier plane.

mode.

During the opening of the diaphragm, δ drops by 30%, especially near the critical region defined by $NA_c = n \sin \theta_c = 1$. This trend can be understood by correlating to the emission diagram. For that purpose, we calculated the radiation pattern in the Fourier plane of a dipole near a glass substrate and in the same experimental situation as for the AuBPs (Fig 4.9b). The center of the Fourier plane corresponds to a narrow solid angle of collection where the direction of the polarization is only linked to the projection of the dipole in the plane of the substrate resulting in $\delta \approx 1$. When collection NA increases, the radiated field is no longer parallel to the dipole, and different radiation directions show different field polarization, so that δ , averaged over all collected angles, is lowered. This effect is stronger at large NA because the scattered field is radiated mostly at high angles, as the evanescent waves of the dipole near-field in air couple to the light propagating modes in glass [39] (blue zone, Fig 4.9a).

Validation of dipole model and extraction of Θ from the curve $\delta(NA)$

As mentioned in the theoretical framework section, to extract Θ from δ , many parameters need to be included in the calculation. While the experimental configuration (collection NA, optical index, substrate, etc) is easily defined, the dipolar nature of the nanoparticles is not always straightforward to confirm. Besides, an ambiguous dipole dimension of nanoparticles might lead to a significant uncertainty of obtained Θ . In fact, the calculation showed that for the specific experimental situation like our study, at a given value of δ , depending on 1D or 2D dipolar particles, the corresponding values of Θ can be different by up to more than 50° [79]. Some previous works need to combine polarization analysis with a supporting measurement to address the nature of the radiation. For example, Fourier plane imaging has been performed to confirm the 2D dipolar nature of the CdSe/CdS nanoplatelets for the orientation determination [76].

It turns out that the fit of many measured δ on the curve $\delta(NA)$ in the Fig 4.9a is a good way to validate the dimension of dipole that should be included inside the calculation. Furthermore, from this curve, Θ is also able to be extracted. The AuBP in Fig 4.9 for instance, the fit of 1D dipole model follows very well the measured data and gives an out-of-plane orientation $\Theta_{fit} = 69^\circ$ with $\pm 2^\circ$ of precision². This value is nearly equal to the orientation obtained from the curve $\delta(\Theta)$ (see Figure 4.6), however, holding a greater confidence. This is due to the fact that the curve $\delta(\Theta)$ is calculated for a fixed collection NA = 1.49 which is only one point on the curve $\delta(NA)$. Besides, the minor different between Θ and Θ_{fit} here is because of the AuBP behaves very similar to a 1D dipole, thus, the fits of the two curves should give the same orientation. In conclusion, from the measurement of $\delta(NA)$, we are more certain about the choice of dipolar nature of the particle for the simulation as well as extraction of its associated orientation.

Which NA is optimal for the measurement of Θ ?

The strong dependence $\delta(NA)$ raises a fundamental question about which objective numerical aperture should be used for the polarimetric measurement. The best NA of an objective to precisely determine a dipole orientation is a compromise between two factors: (i) a strong $\delta(\Theta)$ dependence, and (ii) a good intensity collection efficiency. Let us discuss two extreme cases of nearly parallel or vertical dipoles (as opposed to the substrate surface).

² Θ_{fit} denotes for orientations extracted from $\delta(NA)$, to distinguish with Θ obtained from $\delta(\Theta)$

In the case of elongated nanoparticles that are nearly horizontally deposited ($\Theta > 70^\circ$) such as bipyramids or nanorods, it can be seen clearly in Fig 4.8 that a very narrow NA is not appropriate for the measurement because δ is always unity for every orientations in this region. On the contrary, a large collection NA is favorable results from a minor change in orientation leading to a significant variation of δ . Furthermore, when a dipole is located near a glass-air interface, the most perpetuated polarization and concentrated emission are located around the critical angle, and thus, the collection objective with NA falls inside this region might be the best choice for orientation measurement.

To strengthen our hypothesis, we extract Θ at every collection NA $\in [0.6; 1.49]$ from the curve $\delta(\Theta)$ for the same AuBP. The accuracy of Θ at an associated NA is evaluated based on its quantitative difference with the most precise value - Θ_{fit} extracted from the curve $\delta(NA)$, defined by $\Delta\Theta = \frac{\Theta_{fit} - \Theta}{\Theta_{fit}}$ (%). Figure 4.10 displays the obtained results of $\Delta\Theta$ at different NA and the error of Θ_{fit} is taken as a reference (grey bar). We clearly see that $\Delta\Theta = 0$ at NA = 1-1.1 for all the presented AuBPs with the exception of the last AuBP ($\Theta_{fit} = 85^\circ$). In addition, the errors increase when the AuBPs orient more parallel to the substrate surface. Actually, the polarization analysis is the least sensitive to probe Θ in the range between $80-90^\circ$ because δ is nearly constant for every collection NA [79].

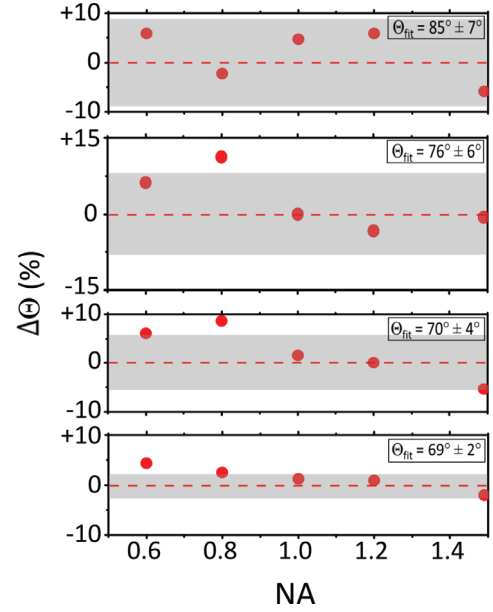


Figure 4.10: Relative different between Θ and Θ_{fit} as a function of NA measured for 4 AuBPs (red dots). Grey bars display the errors of measured Θ_{fit}

In the case of a nearly vertical dipole ($\Theta < 10^\circ$), a small NA objective allows a more accurate determination of Θ than a large NA objective because the Θ increases very quickly when the dipole slightly leaves the vertical position. However, the collection efficiency needs to take into consideration to obtain an adequate signal-to-noise ratio.

4.5 Conclusion

A dark-field scattering polarization analysis has been developed to measure the 3D orientation of AuBPs at the individual level. The out-of-plane component was precisely determined by taking advantage of the angular collection at the wide numerical aperture. We experimentally demonstrated that the more scattered light is collected, the more degree of polarization is decreased. In particular, the contribution of the evanescent wave is especially important in the orientation measurements. It is worth noting that the out-of-plane orientation can also be extracted from the evolution of the degree of polarization with the numerical aperture. Compared to other polarimetric methods, where the dipole orientation is determined from the degree of polarization only for one numerical aperture, our method combined with theoretical analysis strengthens our confidence in the determined orientation. The experimental technique that we have proposed here may be applied to more complex systems such as nanoparticle assembly where our method can discriminate polarization behaviors with the numerical aperture.

The investigation of the orientations of the AuBPs in this Chapter is very important to interpret the optical responses of the nanopatch in the following chapters when the AuBPs are deposited on more complex substrates. On the other hand, in further work, surface treatment by silanization is expected to be done in order to improve the deposition of the AuBPs. More details of this work presented in this chapter can be found in [72].

Chapter 5

Opening-gap nanopatch antennas

We introduce a plasmonic nanopatch antenna consisting of a gold bipyramid nanoparticle separated from a gold film by a sub-10nm TiO_2 gap. In a first step, we show (experimentally confirmed with simulations) that placing a AuBP with contact facet on a high index substrate reveals the hidden quadrupolar mode. In a second step, we demonstrate that the hybrid structure supports a rich optical response that possesses distinctive characteristics of each plasmonic individual: strong field localization inside the metal-insulator-metal gap and radiative nature induced by localized surface plasmon resonance of the particle. This only can be achieved when a crucial condition of the bipyramid's orientation is satisfied: a tip and a facet of the particle touch the surface, forming a nanogap with an opening mouth. In addition, the structure also provides the degree of freedom in the design of geometrical parameters that allow engineering the optical response. Here, we show how the modes are constructed by adjusting the gap thickness. Our investigation establishes a basis for the understanding of the coupling of the nanopatch to emitters.

Contents

5.1	Introduction to opening-gap nanopatch antennas	106
5.2	Characterization methods	113
5.3	Gold bipyramids on a high refractive index substrate	116
5.4	Gold bipyramids on the gold film	122
5.4.1	Scattering spectra	122
5.4.2	Physical formation of the modes	126
5.5	The complexity of the AuBP nanopatch antenna	129
5.6	Conclusion	131

5.1 Introduction to opening-gap nanopatch antennas

Recalling the main characteristics of the gap plasmon of planar MIM waveguides

When two insulator-metal interfaces are brought closer to each other, the SPPs on either side of the dielectric medium hybridize and split into high and low-energy modes. When insulator gap thickness reduces to below the diffraction limit $\sim \lambda/2$, due to the matching of the field symmetry, only the low-energy mode (symmetry) is excited [38]. We refer to this mode as “gap plasmon”. The detailed theoretical descriptions of the planar MIM waveguide can be found in Chapters 1 and 2. Here, we recall two main characteristics of the gap plasmon that would be very beneficial for boosting light-matter interactions:

- large in-plane wavevector k_{\parallel} for tight confinement of light

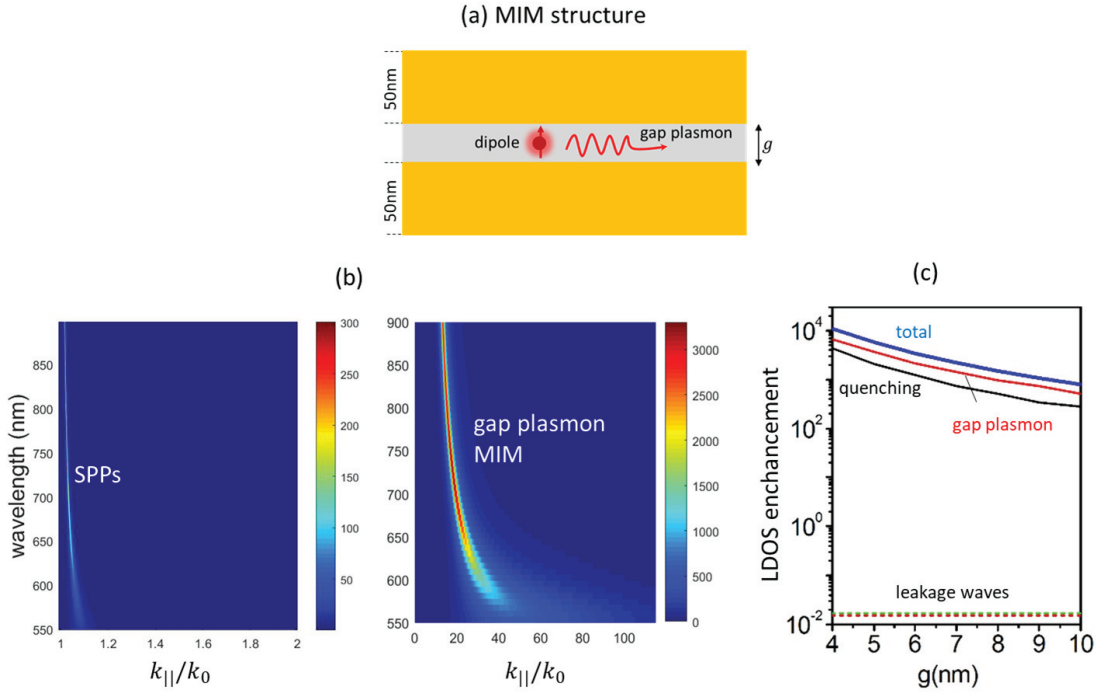


Figure 5.1: **Dispersion relation of gap plasmon and LDOS enhancement of an planar MIM structure.** (a) Geometry of the MIM device: Au/TiO₂/Au. Here the dielectric function of gold ϵ_{Au} is taken from [11], and of the gap $\epsilon_{TiO_2} = (2.4)^2$. A dipole is placed in the middle of gap as a source to excite the optical modes. (b) Calculated dispersion relation of gap plasmon mode of the MIM structure at $g = 4\text{nm}$ and compare to dispersion relation of SPPs on a single interface (c) LDOS enhancement (is proportion to the normalized dissipated power of the dipole) of total system, MIM and quenching and the leakage waves (in the air) as a function of the gap thickness g .

- huge local density of state (LDOS), which overcome the quenching (i.e. lossy surface waves that do not couple to the radiation but undergo heating of the metal).

For example, we calculate the dispersion relation of the gap plasmon and its LDOS enhancement (i.e. Purcell factor) restricted to planar Au/TiO₂/Au structure, as shown in Figure 5.1. We use the same technique as described in Chapter 2, using a point dipole buried in the middle of the gap to excite the optical modes. The dispersion is obtained by calculating the spatial spectrum of the power dissipated by the dipole at each wavelength. As can be seen in Figure 5.1b, the $k_{||}$ corresponding to the gap plasmon is approximately 1 order of magnitude higher than the free-space plane waves of photons or SPPs, provided by a TiO₂ gap thickness of 4nm. This large in-plane wavevector is associated with a small plasmon wavelength $\lambda_p = 2\pi/k_{||}$ on the order of 10nm, for the free-space wavelength of

excitation ranging from visible to near-infrared. On the other hand, the dispersion of the MIM waveguide in the very thin gap limit $g < 10\text{nm}$ also can be approximated as [52, 103]:

$$k_{\parallel} = k_0 \sqrt{\varepsilon_d + 2\xi \left(1 + \sqrt{1 + \frac{\varepsilon_d - \varepsilon_m}{\xi}}\right)} \quad (5.1)$$

where $\xi = \sqrt{\frac{k_0 g \varepsilon_m}{\varepsilon_d}}$ and $k_0 = \frac{2\pi}{\lambda}$. Here, ε_d and $\varepsilon_m(\omega)$ are the dielectric functions of the dielectric and metal, respectively. The equation 5.1 also indicates that the in-plane k_{\parallel} increases significantly as the gap thickness is reduced.

In terms of LDOS, we can equalize the LDOS enhancement of the MIM waveguide as compared to the vacuum to the normalized power dissipated by the dipole. Figure 5.1c displays the value of LDOS enhancement of the gap plasmon mode, the quenching, and the total system as a function of gap thickness between 1-10nm. We can see that all the values of LDOS rapidly enhanced $\sim 10^4$ as the gap thickness decreased. Especially, the LDOS of the gap plasmon largely surpasses the quenching despite the sub-10nm proximity to the metal of the dipole. The work of P. Lalanne et al [104] also found that for vanishing gap thickness, both the gap plasmon mode and the quenching have identical g^{-3} scaling; however, there is also a significant decrease in the group velocity of the gap plasmon thus largely enhancing its optical density. Interestingly, the quenching of the MIM planar system calculated here can be valid for associated nanopatch antennas (see configuration below) of sizes larger than a few nanometers [51, 105].

Gap plasmon antennas based on the MIM waveguide

Practically, to benefit from the full potential of the MIM waveguide, the gap thickness has to be smaller than 10nm [22, 66, 106]. Besides, the gap plasmon has a very short propagation length at this very thin gap thickness, which is around a few ten nanometers, and thus can be completely lost before reaching the end facets of the MIM waveguide-based devices. Therefore, the lateral dimension of these devices is essential close to the propagation length of the gap plasmon. Recent advances in nanofabrication allow producing sub-nm-scale plasmonic dimensions, from which gap plasmon devices can be classified into two main configurations: (i) dimers consisting of two closely-space colloidal metallic nanoparticles [107,

108, 109] or (ii) nanopatch antennas using nanoparticle-on-mirror (NPoM) geometry [22, 53, 105, 110, 111], where a metallic nanoparticle is placed on top of a flat metallic film (mirror), which is predeposited with a thin dielectric spacer to prevent conductive contact.

The attractiveness of plasmonic nanopatch antennas

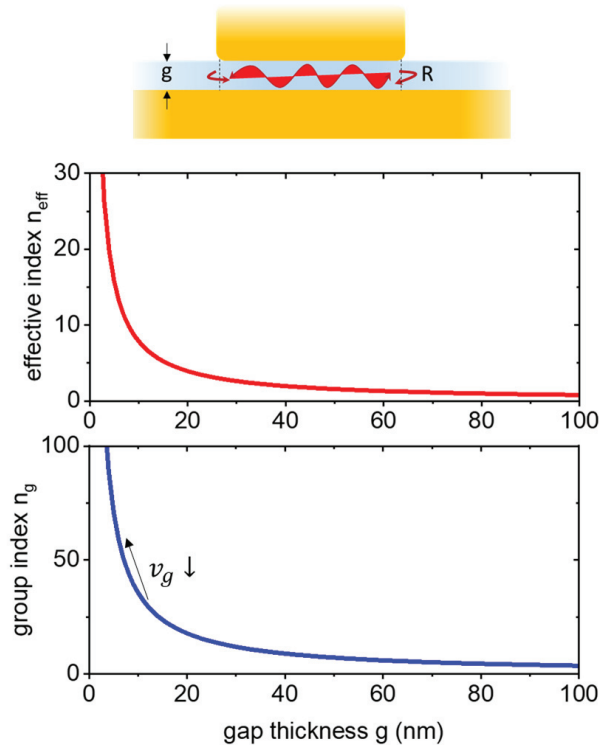


Figure 5.2: **Gap plasmon in a nanopatch antenna.** Gap plasmon in a nanopatch antenna assembles transverse stationary modes in a Fabry-Pérot cavity. The light confinement inside the gap can be evaluated through the effective index and the group index of the modes ($n_g = n_{eff} - \lambda \frac{\partial n_{eff}}{\partial \lambda}$). The indices are simulated at $\lambda = 700\text{nm}$.

- *Fabrication:* Roughly, the gap plasmon produced by a dimer or by coupling a particle to its mirror image in the metallic film is equivalent [53, 112]. However, a particular reproducible, controllable with nanometric precision, and scalable plasmon gap can be constructed for nanopatch antennas by using nanolithography [113], atomic layer deposition (ALD), or self-assembled monolayer molecules [114]. For instance, a gap size below 2nm can be routinely achieved by monolayers of MoS₂, which is identical across large areas over 100cm² [54].
- *A Fabry-Pérot liked cavity:* Due to the limited lateral dimension and reflection at the

nanoparticle edges, the MIM gap plasmon modes can resonantly bounce back and forth below the patch (defined by dielectric spacer embedded between the particle’s facet and the metallic film) and can generate stationary gap plasmon waves, as illustrated in Figure 5.2. In other words, a nanopatch antenna works as a resonator and is analog to a Fabry-Pérot cavity [38, 51].

The nanopatch antennas take full profits from the planar MIM waveguide but further boost its properties. At an optimal configuration, an LDOS enhancement is greater than 2 orders of magnitude as compared to the associated MIM planar waveguide can be achieved by the nanopatch antenna [104], from which the quenching becomes negligible. This can be achieved firstly because the mode volume is shrunk into a deep subwavelength scale $V \sim (\lambda/2n_{eff})^3$ with $n_{eff} = Re(k_{||})/k_0$ is the effective refractive index of the gap plasmon mode. The second reason is that there is an increase of the quality factor Q even at very proximity to the metal surfaces where its absorption is considerable. Intuitively, the gap plasmon mode is slowed down (i.e., its group velocity is reduced) due to the bouncing back and forth between the patch’s edges, which is very similar to the light trapping for a long time inside photonic crystal cavities [115]. It is worth mentioning that for an extremely thin gap $< 10\text{nm}$, the Fabry-Pérot cavity model has been proven that it is still valid to describe the resonance of gap plasmon mode; however, the quality factor provided by the nanopatch antennas is limited by the value in the quasi-static limit $Q_s \sim 10^2$ [51] (with $Q_s \propto \omega_0/Im(\varepsilon_m)$ [116], the imaginary part implies that the loss is purely induced by the intrinsic loss of the metals).

Opening gap nanopatch antennas

Despite holding many advantages as presented above, the conversion of gap plasmon modes in the nanopatch antennas into desired output channels such as free-space radiation or SPPs is relatively inefficient. This is because of the large mismatch between in-plane $k_{||}$ of the plasmon gap mode and k_0 in free space, the resonant hotspots in the gap typically emit into high angles for thin gap thickness, which is nearly inaccessible by using the conventional phase-matching devices such as gratings or prism couplers. This loss is usually referred to as “coupling loss”. Recent works [51, 117] have shown that engineering the facets of

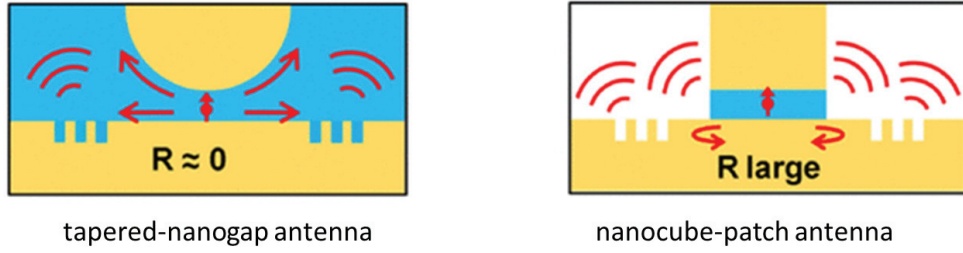


Figure 5.3: **Classification of gap plasmon antennas based on its facet reflectivity** Left: Tapered-nanogap antennas with low facet reflectivity $R \approx 0$. Right: nanocube-patch antennas with large facet reflectivity. Source: R. Faggiani *et.al.*, [104].

the nanoparticles could mitigate reflectivity at the end of the nanopatch and thus reduce the coupling loss. For example, two configurations are presented in Figure 5.3. A tapered antenna implements no reflectivity at the “mouth” of its curve edges yielding significantly large photon-radiation conversion above 70%, which is ~ 4 times higher than its counterpart, e.g. the state-of-art nanocube antennas, with a large facet reflectivity. In turn, the tapered antenna offers a smaller LDOS of gap plasmon mode (around 1 order of magnitude at the same gap thickness). Therefore, a nanopatch antenna design that provides a better balance between the large gap mode density and high photon-radiation efficiency is necessary.

In this context, we propose a new structure of gap plasmonic antenna with delicate engineering of facets, which is expected to offer a better balance between the large gap mode density and high photon-radiation efficiency. The antenna consists of a colloidal synthesized gold bipyramid nanoparticle (AuBP) placed over a gold film, separated by a well-controlled nanoscale dielectric gap (Figure 5.4). The interesting feature of this antenna design comes from the geometry of the AuBPs when they lie on the metallic surface, each plays a role as a nanopatch antenna with an “opening-mouth”. The cavity volume is determined by the space between the bipyramid and the underlying gold film. This volume consists of two parts: (i) the dielectric spacer with a fixed thickness embedded between a triangular facet of AuBP and the gold surface (flat gap) and (ii) the mixing of air/dielectric gap resulting from the inclination of the bipyramid (“opening-mouth”).

To intuitively understand the different behavior of each component gap induced by their geometry, we calculate the effective refractive index $n_{eff} = Re(k_{||})/k_0$ of the MIM mode inside each gap. While a full simulation that takes into account the geometry of the nanoparticle’s

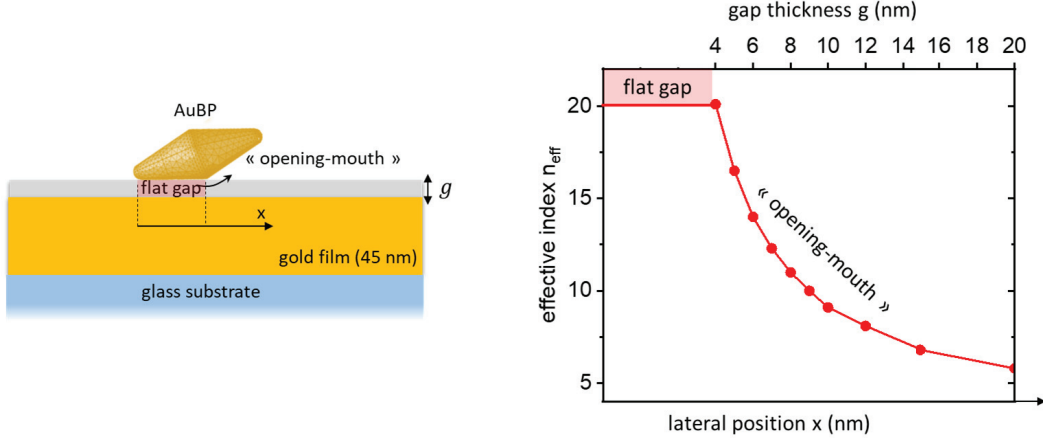


Figure 5.4: **Opening-gap nanopatch antenna of gold bipyramid.** Left: Geometry of the patch antenna with gap is made from TiO_2 . Right: effective index of gap plasmon associating to the flat gap (g is fixed at 4nm) and opening-mouth gap ($g = 4 - 20\text{nm}$).

facets is needed to find the exact value of n_{eff} , an approximation to the planar MIM structure of infinite width is possible for the extremely small gaps used here. Indeed, for a small gap situation $g/\lambda \rightarrow 0$, the effective index n_{eff} can be given from equation 5.1 with an assumption that $\xi \gg \varepsilon_m, \varepsilon_d$

$$n_{eff} = -\frac{2\varepsilon_d}{\varepsilon_m(gk_0)} \quad (5.2)$$

For vanishing gap thickness, the n_{eff} becomes independent of the width. This can be thought of as the mode confinement caused by reducing the gap thickness between two metallic surfaces is considerably stronger than those induced by dielectric walls at the end facets. For any given value of the lateral width w , we can have $w \gg \lambda/(2n_{eff})$ as the gap thickness is reduced.

Here, we deduce the n_{eff} of the gap plasmon mode of the bipyramid nanopatch antenna from the in-plane $k_{||}$, which is computed from an equivalent planar MIM structure. Figure 5.4b shows the evolution of the calculated n_{eff} with the lateral position x . The n_{eff} is sufficiently large and constant inside the flat gap region. However, along the opening-mount gap, n_{eff} is gradually reduced as the gap thickness increases, thus paving the way for the light escape to the free space. In other words, while the flat gap offers a platform for effectively supporting the MIM plasmon modes, the opening-mouth gap can play a role in efficiently

converting these modes into outgoing SPPs/photons.

5.2 Characterization methods

Experimental methods: In our experiments, the substrate is prepared by evaporating a 45nm gold film with a 5nm Cr adhesion layer onto a clean glass coverslip via electron-beam evaporation. A sub-10 nm dielectric spacer layer of TiO_2 is grown on the Au film via atomic layer deposition. The thickness of the TiO_2 spacer is well-controlled by the number of deposition cycles. Finally, a diluted solution of 30nm-width and 80nm-length gold bipyramids is dropped onto the TiO_2 surface. The concentration of the colloids in the solution and the time that the surface is exposed to the colloidal solution are controlled to ensure a low bipyramid surface coverage for single-nanoparticle measurements. It is worth noting that the AuBPs have been subtly synthesized with not sharp, but curved end edges (by controlling the growing time of the seeds [89, 90]) to mitigate the reflectivity and avoid the point effect of charge accumulation.

The optical index of gold film and TiO_2 spacer is measured by a spectroscopic ellipsometer. Below 10nm thickness, the TiO_2 film has refractive index $n_{\text{TiO}_2} = 2.4$. Above this, the deposited film's optical index might vary due to the changing in the crystal structure of TiO_2 . The thicknesses of each layer are determined optically from SPPs dispersion shifting via leakage radiation microscopy (see Chapter 3). Atomic force microscopy is also performed to measure the thickness and gives the same results as the optical measurement.

To identify the optical modes of the system, we characterize the scattering of white lamps from individual AuBPs on the substrate via dark-field spectroscopy. Figure 5.5 depicts a schematic of the experiment and the structure of the nano patch antenna with a bipyramid situated on a gold film. The experimental setup of dark-field microscopy was described in detail in Chapter 3. Briefly, an unpolarized white light beam is focused onto the sample using a 40X objective with $\text{NA} = 0.25$ so that the sample is uniformly illuminated from small angles of incidence $\theta_i = 0 - 15^\circ$. Forward scattering is then collected in transmission by an oil immersion objective ($\text{NA} = 1.49$) while the excitation beam is omitted from the detection by a beam stop ($\text{NA}_{BS} = 0.5$) installed at the back focal plane of the oil objective. With

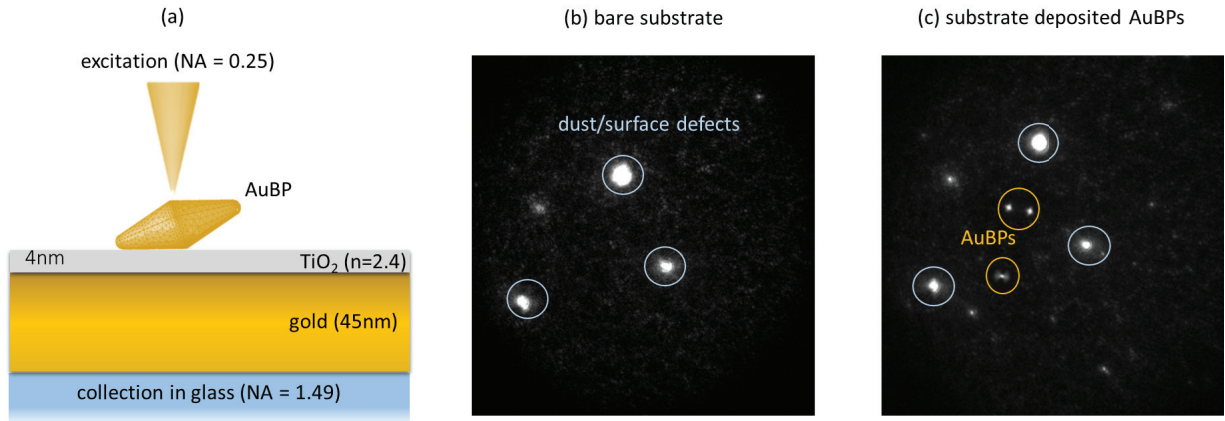


Figure 5.5: **Nanoantenna scattering.** (a) Experimental scheme. (b-c) Dark-field images of one excitation spot on the surface of TiO₂/gold film before (b) and after (c) depositing AuBPs.

this configuration, the collection angles take place between $\theta_c = 20 - 80^\circ$.

In a dark-field image, any object that scatters light appears as bright spots on a dark background. Because of the limit of diffraction, it is not straightforward to distinguish the AuBPs from other objects that might be present on the substrate such as dust or holes (observed in the AFM images). This is easier for AuBPs deposited on a glass substrate where a single particle can be well identified based on its distinctive longitudinal LSPR on the scattering spectrum. In the situation of AuBPs on the TiO₂/gold film, the interaction between the particle and the substrate can induce unpredictable scattering resonances (see later). To locate AuBPs on the dark-field images, we correlate images of the substrate before and after depositing AuBPs. Figure 5.5b shows a dark-field image of the bare TiO₂/gold substrate with some dust/holes appearing as extremely bright spots due to its big sizes. Subsequently, an image at the same excitation area but after dropping the diluted solution of AuBPs. By correlating the two images, we can identify the scattering from AuBPs that are marked as gold circles in Figure 5.5c. The dilution can be done in ethanol that rapidly evaporates (~ 15 minutes, room temperature), and thus allows a fast acquisition time of two correlated images without changing the excitation spot's position on the sample stage.

Method of calculation: COMSOL simulation has been performed to calculate the optical cross-section spectra, associated charge distributions, and near-field distribution of the

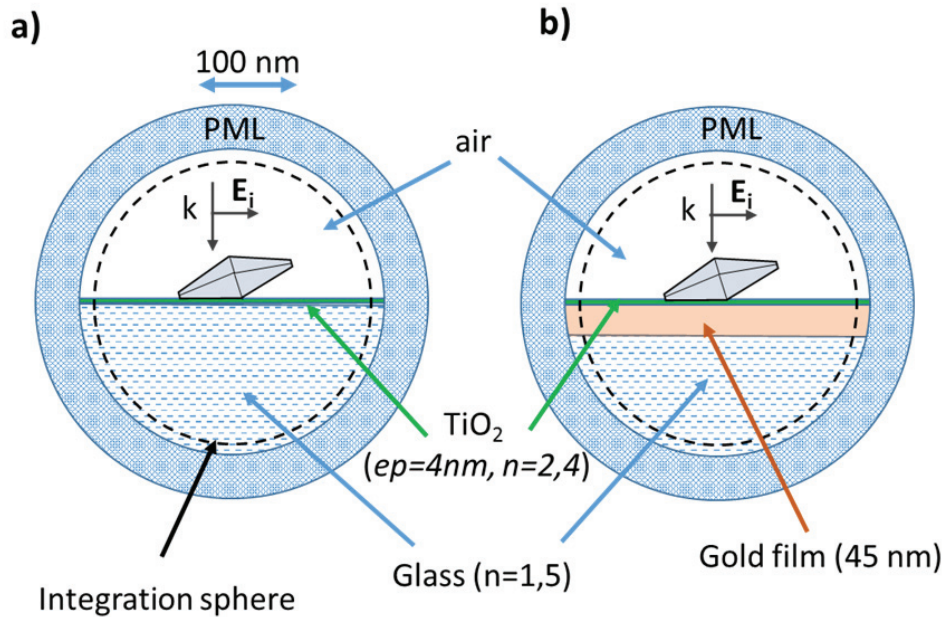


Figure 5.6: **Configurations of the COMSOL simulation for calculating scattering cross-section.** The AuBP is deposited on (a) 4nm- TiO_2 /glass substrate and (b) 4nm- TiO_2 /45nm-gold/glass substrate. The excitation of a plane wave in the normal direction and polarized along the long axis of the AuBP takes place in air. The integration sphere defines the surface for calculating the scattered power in the near-field.

nanopatch. The geometrical dimensions and features of the bipyramids (i.e., the truncated tips and a pentagonal base) are given by the TEM measurement (see Chapter 3). Two configurations are simulated: the AuBP is either placed on a TiO_2 film (Figure 5.6a) or a TiO_2 film over a gold film (Figure 5.6b), both supported by the glass substrate. Here, the dielectric function of gold $\epsilon_m(\omega)$ is taken from the Johnson and Christy's table [11]; and for the spacer, we use a refractive index $n_{TiO_2} = 2.4$, which is obtained from the ellipsometry measurement. The background fields in each media are those resulting from the excitation by an incoming plane wave normal to the substrates, in the absence of the AuBP. The incoming electric field is linearly polarized along the long axis of the particle. The scattered power (or scattering cross-section) is calculated in the near field by integrating the corresponding Poynting vector over a sphere enclosing the AuBP (see Figure 5.6), which accounts for contributions in air and glass semi-infinite media as well as in the supporting films. The COMSOL simulations in this Thesis are done by Michel Pellarin.

5.3 Gold bipyramids on a high refractive index substrate

The nanopatch substrate consists of multilayers that are both absorbing (gold) and dielectric (TiO_2 and glass) materials. Since the TiO_2 spacer has a high refractive index of 2.4, it might have certain impacts on the optical response of the deposited AuBP. To support the interpretation of scattering from AuBPs on nanopatch structure later, we first perform the dark-field scattering measurement of AuBP on a 4nm- TiO_2 /glass substrate.

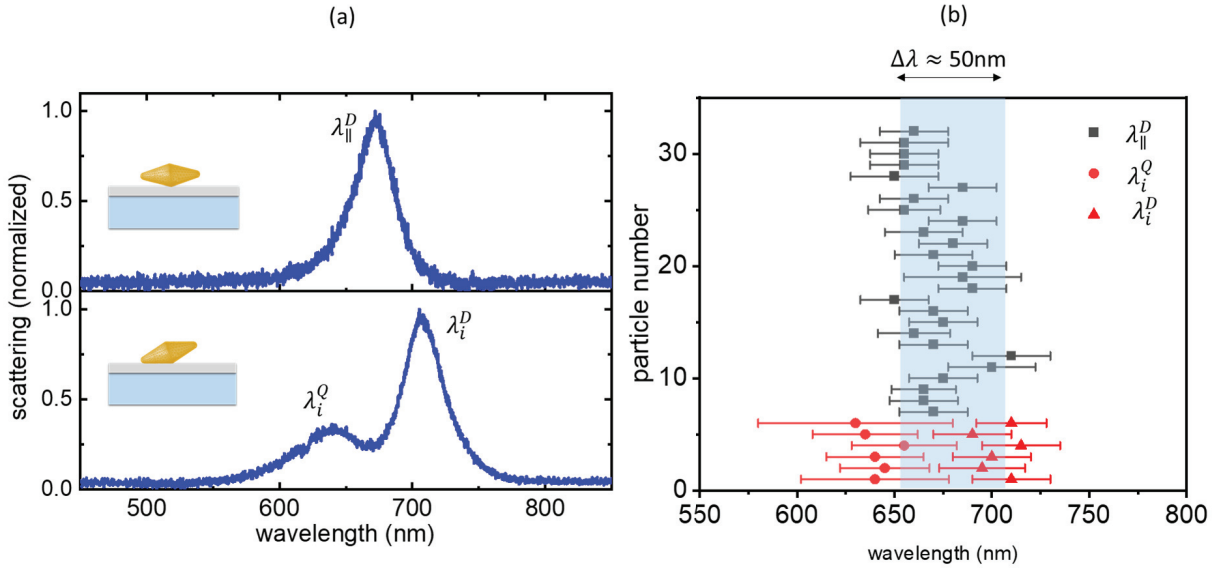


Figure 5.7: **Scattering of AuBPs on 4nm- TiO_2 /glass substrate.** Left: Two selected spectra represent two kinds of spectra measured. Right: Resonance wavelength and spectral width of many particles

We observed two kinds of scattering spectra as shown in Figure 5.7. The first one exhibits single-mode resonance at around $\lambda_{\parallel}^D = 680$ nm, which is associated with the longitudinal LSPR of AuBPs. In the second, the longitudinal mode is red-shifted by ~ 30 nm (λ_i^D) and interestingly, a small additional mode arises in the shorter wavelength at $\lambda_i^Q = 640$ nm. We emphasize that these spectral features are reproducibly observed across many AuBPs. We present their resonance wavelengths and associated spectra widths in Figure 5.7b. The single-mode particles (black dots), all show a narrow FWHM ~ 50 nm that is nearly equal to that of AuBPs on the bulk glass substrate, suggesting the presence of the very thin TiO_2

layer merely leads to an additional mode broadening. In terms of the center position of resonance, a dispersion of $\Delta\lambda \approx 50\text{nm}$ is observed for different single-mode AuBPs.

Orientation effects on the optical response: Qualitative description

As we will show in the simulation below, the appearance of two sets of scattering modes is induced by the orientation of the AuBPs on the substrates. Due to the elongated morphology, the plasmon resonance of AuBPs is mostly sensitive to the local properties of the external medium near its “hot-spot” tips, where the field is strongest enhanced (around 2 orders of magnitudes [68, 5]). Therefore, for a given distance of the particle from the surface, the interaction strength of AuBPs and underneath substrate is expected to strongly depend on the tip-substrate separation, which is governed by the orientation of the AuBPs. Our previous measurement indicated that the inclination of AuBPs on the flat substrate ranges between $0 - 30^\circ$ (see Chapter 3) corresponding to the tip-substrate distances of $0 - 15\text{nm}$. Therefore, there are situations in which the AuBPs incline with a tip touching the substrate, the particle-substrate interaction is significant yielding to the red-shifted of the longitudinal plasmon resonance and the birth of a new optical mode. In contrast, there are bipyramids that lie flat along the surface so that the presence of the substrate weakly impacts their scattering.

Simulation observation

To examine the orientation effects on the optical responses of the particles, we calculate the scattering cross-section spectra in two situations: (i) AuBP lies horizontally to the substrate and (ii) tilting AuBP by 20° to lie one tip against the surface and the other raised in the air (see Figure 5.8). The simulation of surface charge distribution has been also performed to understand the origin of the modes.

As expected, the two orientations induce different optical responses as observed in the experiment. The horizontal bipyramid exhibits single resonance with center wavelength and the spectra width is almost identical to AuBPs deposited on the glass substrate without the presence of the TiO_2 film (Figure 5.8 above). The inset of simulated charge distribution also confirms its longitudinal dipolar nature. Since the tips are separated far from the substrate, the localized charges around the tip mostly feel the homogeneous medium of air resulting in

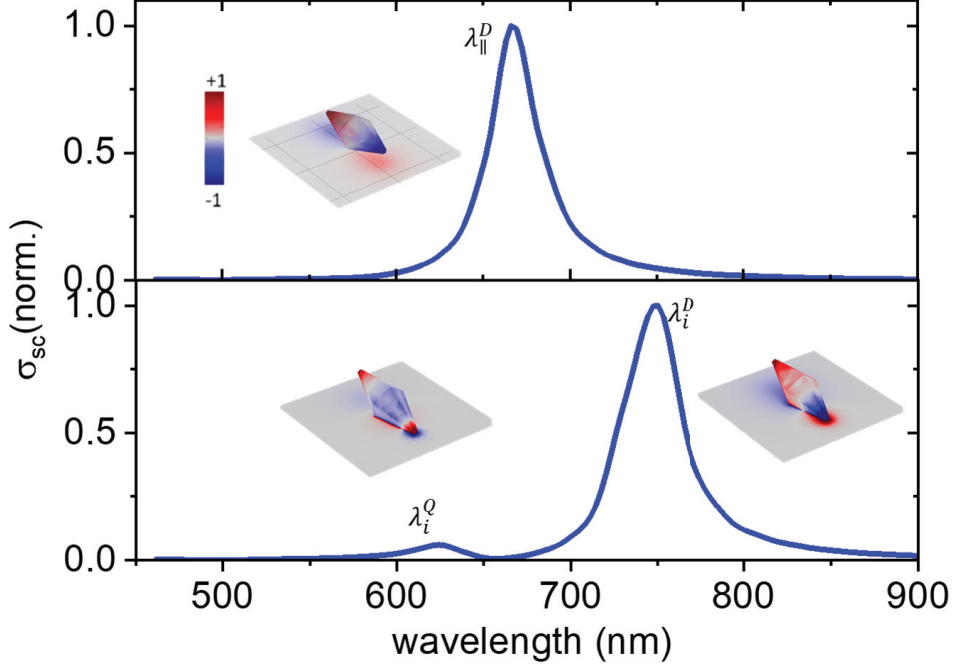


Figure 5.8: **Calculation of scattering cross-section of the AuBPs on 4nm-TiO₂/glass substrate.** Two orientations of the AuBPs are simulated: horizontal to the substrate or tilted with a tip touching the surface.

negligible modification of the longitudinal plasmon mode in the far-field scattering. On the other hand, when one tip of the inclined AuBP touches the surface, it strongly senses the inhomogeneous of the local optical index induced by the underneath layered substrate. As the result, the dipolar longitudinal plasmon is propelled to the higher wavelengths (λ_i^D) and gives rise to the new mode at the lower wavelength (λ_i^Q). The separation of these two modes is around 100nm, which is nearly equal to the value observed in the experiment.

We note that this double-resonance response does not occur for intermediate orientations of AuBPs (i.e. tip is separated from the surface), suggesting the effect of lateral surface contact. Tilting AuBPs by a maximum inclined angle not only minimizes the tip-substrate distance but also allows a facet of the particle contacting to the surface and thus results in stronger interaction. On the other hand, the intermediate orientations are responsible for the dispersion of scattering resonance as observed in Figure 5.7b. However, the resonance wavelength is only dispersed in the range of the spectra width ($\Delta\lambda < 2FWHM$). This means that as long as the tips are separated from the surface, the orientation only plays a

minor role in the optical response of the AuBPs, its effect cannot compete with broadening induced by the intrinsic losses of the metallic particle.

The mode λ_i^Q has an even symmetry in the charge distribution, which resembles a longitudinal quadrupole. One possible explanation for the birth of this mode λ_i^Q is the result of its coupling to the dipolar mode. The work of P. Nordanler et al [92] about the nanocubes showed that the “dark quadrupolar mode” can reveal itself in the scattering spectra through coupling to the “bright dipolar mode”. This interaction is mediated when a facet of the nanocube contacts the substrate. This interaction is especially pronounced for a large dielectric constant substrate and a small particle-substrate separation. In the case of bipyramid, because of the more complicated geometry, further calculation and study are needed to fully understand. Nevertheless, all the features are in good agreement between the experiment and simulation.

Estimation of the penetration depth of the field around the AuBP’s tip.

Above we have seen the important role of the orientation effect on the interaction of the AuBPs and the substrate. Now at an optimal tilting configuration that completely omits the spacing between the tip and the surface, we want to estimate the thicknesses of the TiO_2 spacer at which the “hot spot” of AuBPs still “feels” the glass substrate underneath it. This can be done by tracing the resonance shift of the dipolar longitudinal mode when the TiO_2 thickness increases gradually. Roughly, the change of TiO_2 film thickness induces the change of the effective index of the layered substrate ($n_{\text{glass}} < n_{\text{eff}} < n_{\text{TiO}_2}$), and thus yields the shift of the localized plasmon resonance.

Figure 5.9 shows the calculation of the scattering spectra of an AuBP inclined on the TiO_2 film/ glass substrate, considering the TiO_2 thickness as an adjustable parameter $t = 0-20\text{nm}$. The resonance wavelength of the associated dipolar mode is also reported in the Figure 5.9 as a function of t . There is no surprise that the plasmon mode is red-shifted when the TiO_2 film thickness increases, by more than 100nm. At $t = 0$ (i.e., without TiO_2 film), the plasmon resonance is identical to that of AuBP on the bulk glass substrate. When the TiO_2 film thickness increases, λ_i^D is rapidly red-shifted for small thicknesses; then becomes saturated and asymptote to the resonance of the AuBP on the bulk TiO_2 substrate when $t > 10\text{nm}$. Especially, this evolution follows very well a fitted exponential function

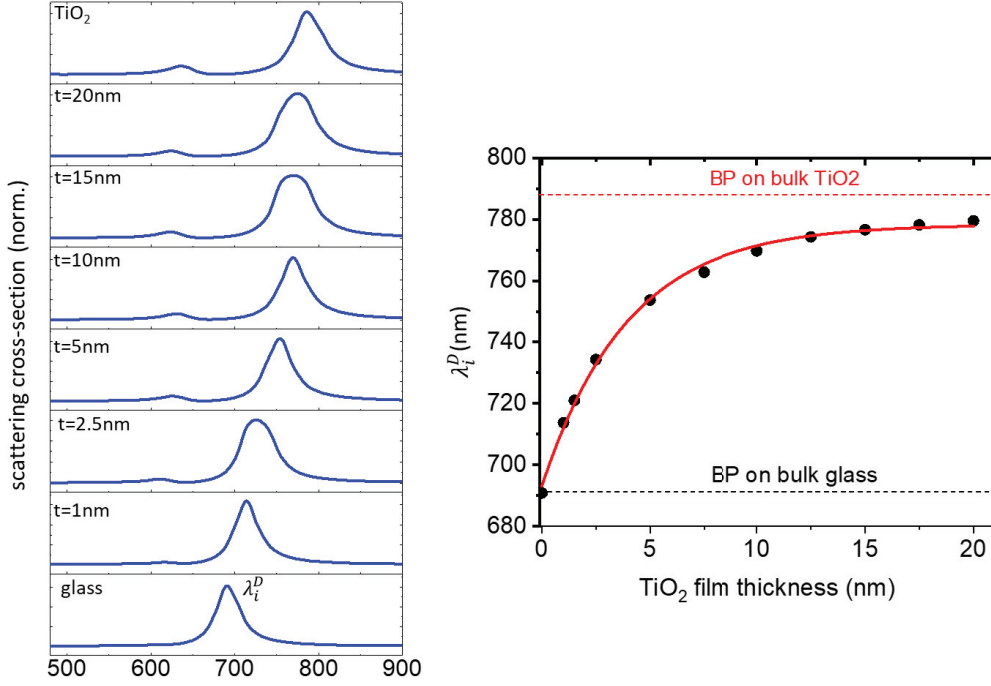


Figure 5.9: **Calculation of scattering cross-section spectra of AuBPs on TiO₂/glass substrate with varying TiO₂ film thickness.** The longitudinal dipolar plasmon resonance λ_i^D is plotted as a function of the TiO₂ film thickness t (black dots) and fitted with an exponential function (red line).

$$\frac{\Delta\lambda_i^D}{\Delta\lambda_0} \propto e^{-t/\tau} \quad (5.3)$$

where $\Delta\lambda_i^D = \lambda_{TiO_2} - \lambda_i^D$ and $\Delta\lambda_0 = \lambda_{TiO_2} - \lambda_{glass}$, with $\lambda_{TiO_2} = 770\text{nm}$ and $\lambda_{glass} = 690\text{nm}$ are the longitudinal dipolar plasmon resonance wavelength of the AuBP on the bulk TiO₂ and glass substrate, respectively. The exponential decay of the resonance shift here resembles the "universal" scaling behavior of the interparticle plasmon coupling, which can be explained by the dipole-dipole coupling model [118]. In this work, the authors show that the exponential decay can be approximated nearly the scaling of the near field of the plasmon particle or the coupling strength as D^{-3} , with D is the interparticle distance.

We assign τ to the critical thickness of TiO₂ film (i.e., decay length) that for $t < \tau$, the localized plasmon field of AuBPs can significantly penetrate the glass substrate and feel its impact. Here, the fit gives $\tau = 5\text{nm}$, which means that if we want the AuBP to interact effectively with the underneath substrate, the thickness of TiO₂ should be smaller than 5nm.

Therefore, in the following measurement of AuBPs on the gold film configuration, we choose TiO_2 spacer thickness below 5nm.

5.4 Gold bipyramids on the gold film

5.4.1 Scattering spectra

Experimental results. Figure 5.10 presents the scattering spectra of AuBPs deposited on the 4nm-TiO₂/45nm-gold/ glass substrate. From the dark-field measurements, we also recorded two categories of spectra: single mode and multimode.

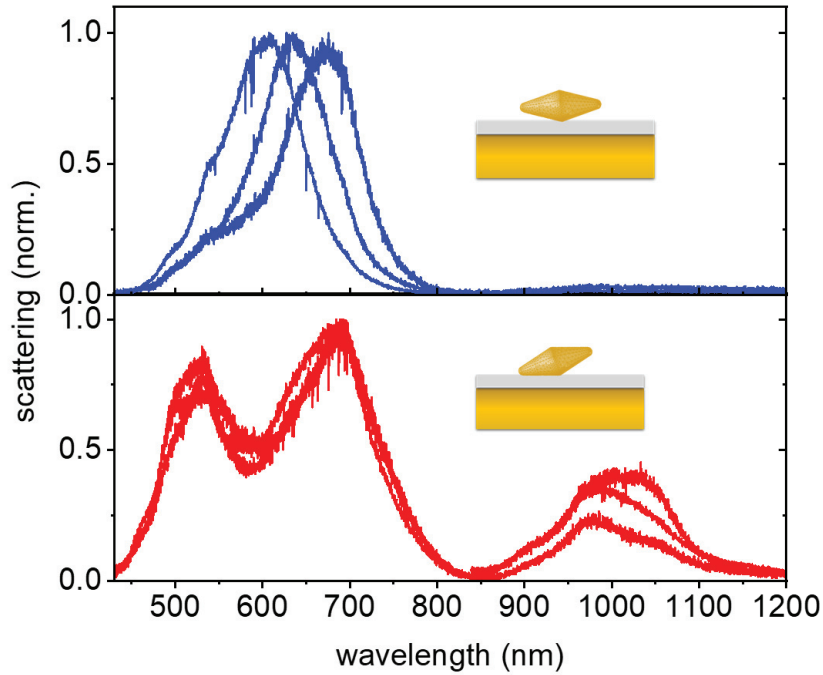


Figure 5.10: **Scattering spectra of the AuBPs on gold film measured by the dark-field microscope.** The measured spectra are classified in two kinds: single-peak spectra and multiple-peak spectra corresponding to the orientations of the AuBP (insets).

For single-mode spectra, the resonance wavelength is not far from the associated position of horizontal AuBPs placed on the TiO₂ film/ glass substrate at ~ 680 nm. Based on the previous discussion, we correlate these single-mode spectra to longitudinal dipolar plasmon resonance of the AuBPs oriented *without* tip-touching the surface (inset), in which the localized plasmon is weakly affected by the underneath substrate. However, the absorption of the gold film induces a large dispersion of the resonance wavelength from 600nm to 700nm accompanied by a broadening of ~ 100 nm, which is 2 times larger than the spectra width of

AuBPs on the bare glass substrate. Besides, in some scattering spectra, there is a shoulder arising at the blue side of the main dipolar resonance.

For the multimode spectra, many modes are excited that expand the spectrum from the visible to the near-infrared regime. The center wavelength positions of the three main peaks in Figure 5.10 (below) take place at approximately 530nm, 700nm, and 1000nm, respectively. In which, the two first peaks share a dip at around 600nm. We note that visible resonance was measured by the 1st grating of the spectrometer (Andor, Kimera 193i model), whereas the 1000nm-resonance was recorded by the 2nd grating in order to obtain better detection efficiency.

Simulation results. We simulated the scattering spectra of AuBPs on 4nm-TiO₂/45nm-gold/ glass substrate by the COMSOL calculation, particularly focused on the two orientation configurations: horizontal (Figure 5.11) and maximum incline (Figure 5.12).

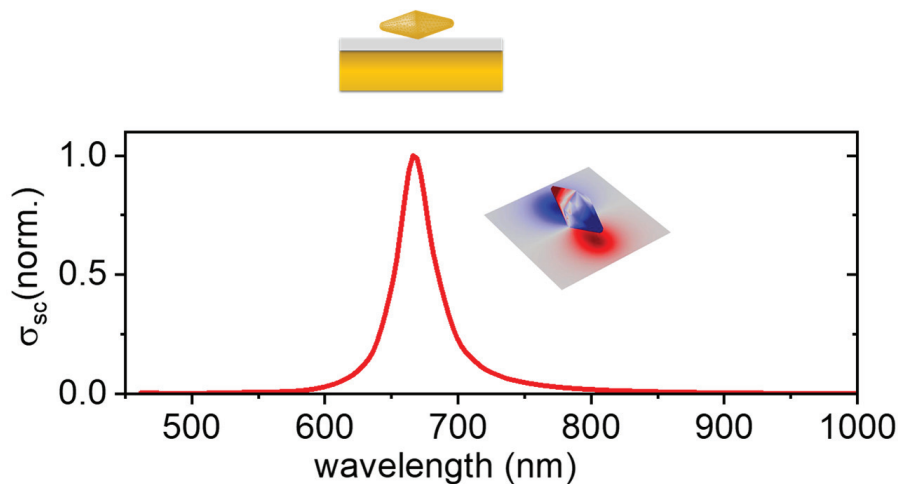


Figure 5.11: Calculation of scattering cross-section spectrum and associated charge distribution of the AuBP lying parallel to the gold film

As expected, the optical response of the flat AuBP (Figure 5.11) is nearly unaffected by the presence of the absorbing substrate of gold: only dipolar longitudinal plasmon resonance is exhibited with negligible spectral shift and broadening, as compared to the previous situation without gold film. In contrast, tilting the AuBPs yields a distinctive optical response with a rich structure of modes. We can see a series of peaks that appear in the simulated scattering

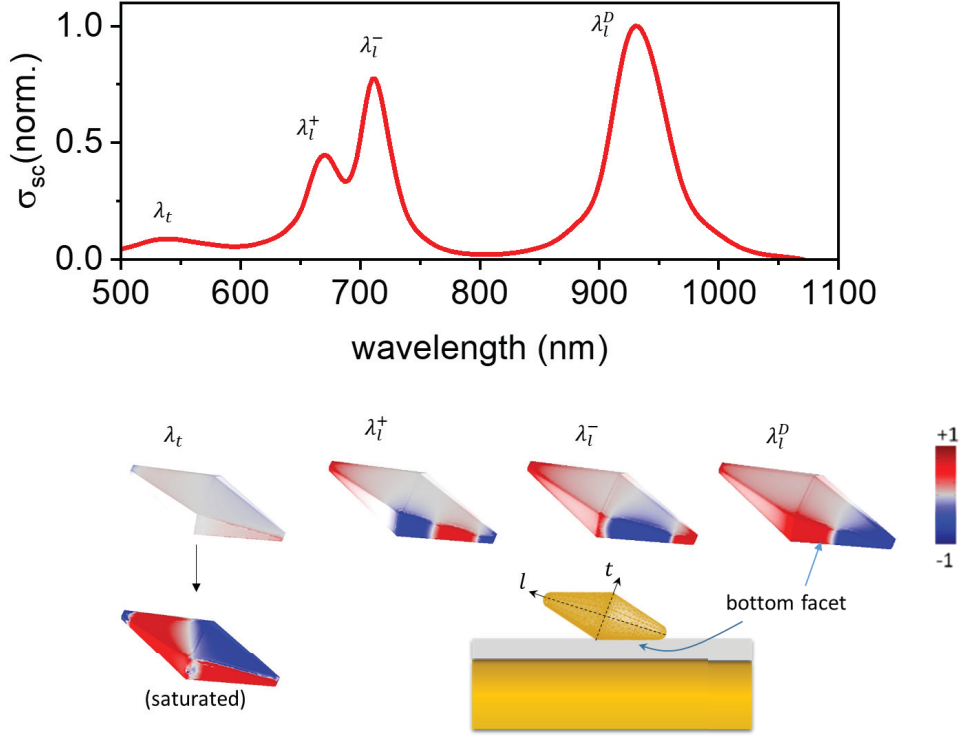


Figure 5.12: **Calculation of scattering cross-section spectrum and associated charge distributions of the inclined bipyramid on gold film.** The particle is rotated to display the charge distribution in the bottom facet that contact with the gold film. The charge distribution of the weak resonance λ_t is also displayed in saturation. The longitudinal and the transverse axis of the AuBP are denoted as l and t

spectrum in Figure 5.12, labeled as $\lambda_t = 530\text{nm}$, $\lambda_l^+ = 670\text{nm}$, $\lambda_l^- = 720\text{nm}$, and $\lambda_l^D = 930\text{nm}$. In which, the l resonances dominate the scattering spectrum while the t resonance only exhibits a weak contribution. Besides, the two resonances λ_l^+ and λ_l^- share a dip at around 700nm . In the following, we strict our discussion on the configuration of the AuBP tilted on the surface.

Identification of the modes from the charge distributions

To support the understanding of the nature of the modes, we first simulate the charge distribution of the modes, as presented in Figure 5.12 (below). Here, there is symmetry breaking in the charge distributions induced by the substrate. As we can see in all the presented modes that the charges on the AuBP are mostly modified in the region that contacts the substrate (flat gap) while elsewhere it remains nearly unchanged (opening mouth). We classifies the modes into two categorises: t and l modes, since their charges mainly variate in

the transverse or longitudinal axis of the system, respectively.

- *The t mode:* The weak and resonance below 600nm is a broad distribution of hybridized modes. Here, we only display the charge distribution of the center position at $\lambda_t = 530\text{nm}$. In fact, the nearby wavelengths (still inside this resonance) are varied in the charge distribution, which is not shown here for clarity. The mode decomposition of this low-wavelength resonance can be found in [119], where the authors also show this broad resonance as a spectral overlapping of many higher-order quasi-normal modes. Although the charge configuration is complex due to the interaction with the substrate, it can be considered close to the transverse mode of the system as observed in the saturated image (Figure 5.12 below). Because of the very weak far-field optical response, in the following, we only focus on the three dominant radiative modes of the longitudinal l category.
- *The l modes:* The mode λ_l^D shows its longitudinal dipolar character of the AuBP as the opposite charges are distributed on the two sides of the particle. On the other hand, for the modes λ_l^+ and λ_l^- , it is not straightforward to fully interpret the nature of these modes owning their complicated charge configuration. However, we still point out some main features that can be observed here. For example, both displays an intense charge distribution with many nodes on the facet of the AuBP that contact to the underlying gold film. Besides, unlike the mode λ_l^D which has a nodal line at the middle of the facet, the modes λ_l^+ and λ_l^- have maximum charge accumulation in the middle and two edges of the bottom facet.

Correlation of the experiment and simulation spectra

Qualitatively, the simulation covers all the resonance that appears in the measured spectra, except for the resonance at $\lambda_l^+ = 670\text{nm}$ which we believe is spectrally overlapped by resonance λ_t . However, we insist that the scattered power, as it is calculated here, accounts for contributions in air and glass semi-infinite media as well as in the supporting films (which is defined by the integration sphere in Figure 5.6). It cannot be directly compared to the power scattered at very large distances (far field) in the collection angle defined by the immersion oil objective used in experiments (glass/oil media). Actually, the simulated power

in Figure 5.12 (integrated in the near-field) is close to the sum of the powers scattered at large distances in the air and in the glass media (over a solid angle of 2π sr). However, the corresponding spectra would be shown to be different, not in the location but rather in the intensity of resonances.

Moreover, the scattered light collected experimentally depends on: (i) the far-field scattering diagram in the forward direction and (ii) the numerical aperture of the collection objective. Corresponding far-field spectra can be determined but they were not calculated during this thesis. As a consequence, it must be bear in mind that a comparison between experiment and near-field calculations will be relevant only in discussing the positions of the plasmon resonances that are independent of such considerations.

5.4.2 Physical formation of the modes

In order to further understand the nature and the formation of the plasmon modes of the AuBP nanopatch, we investigate the spectral evolution of the modes with the dielectric gap thickness. Figure 5.13 shows the calculation of scattering cross-section spectra, considering the gap thickness as a varying parameter. The gap thicknesses are set smaller than $\tau = 6nm$, i.e., the thickness of TiO_2 film at which, the bipyramid still interacts effectively with the underlying film (as shown in Figure 5.9). When the g decreases, the mode λ_l^D is seen to rapidly redshift. This shift is mostly induced by the mirror effect, i.e., the interaction between the longitudinal dipolar mode of the AuBP and its charge image in the underlying gold mirror, which resembles a dimer configuration [112, 120, 107].

The most remarkable aspect of the dispersion curves in Figure 5.13 is that the two modes λ_l^+ and λ_l^- display the distinctive feature of the mode hybridization with an anti-crossing evolution. The green and red lines are plotted to guideline the interaction between fundamental modes, which we denote as λ_l^Q and λ_l^G . At $g = \tau = 6nm$, only mode λ_l^Q displays a strong scattering resonance at around 680nm. We assign the mode λ_l^Q to the longitudinal quadrupolar mode of the AuBP which is similar to the one that has been observed in the case of the AuBP placed on the TiO_2 film/ glass substrate (see Figure 5.8). On the other hand, the mode λ_l^G just weakly appears as a shoulder of the λ_l^Q on the blue side at the beginning. When the gap thickness is reduced, the resonance of λ_l^G becomes prominent, which correlates

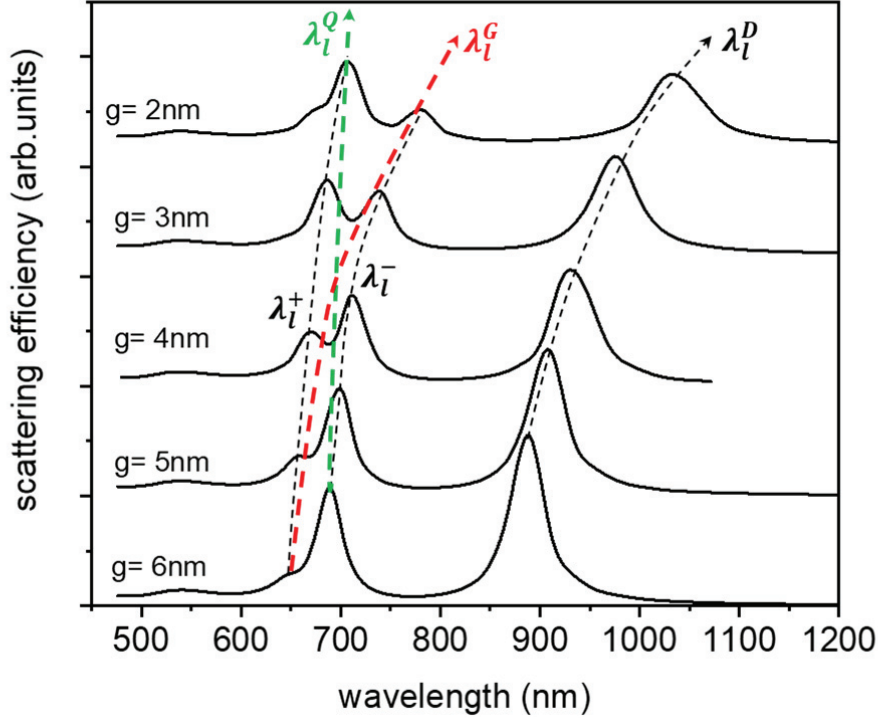


Figure 5.13: **Spectral evolution of the modes with the gap thickness.** Scattering spectra of the AuBP on gold film calculated for different gap thickness g . The evolution of the l resonances is guided by the black line. The interaction between the two fundamental mode λ_l^Q and λ_l^G is also illustrated in red and green lines.

with the characteristic of the MIM gap plasmon mode. Variation of the gap thickness allows these two fundamental modes to approach spectrally, they interact and open a wavelength gap, forming the hybrid modes. As shown in Figure 5.13, the strongest interaction can be observed at around $g = 3-4$ nm. This is consistent with the results of the charge distribution of the hybrid λ_l^+ and λ_l^- modes found previously at $g = 4$ nm, where we can see at the facet that forms the MIM waveguide with the gold film, they share the same symmetry and the charges oscillate in the opposite phase (see Figure 5.12).

To further understand the symmetry rules that are responsible for the mode hybridization, we simulate the near-field distribution of the l modes. Figure 5.14 displays the simulation of the normalized total electric-field distribution $|E|^2/|E_0|^2$ (in the yz plane normal to the substrate) and its scattering field components along the z -axis $Re(E_z)$ and y -axis $Re(E_y)$,

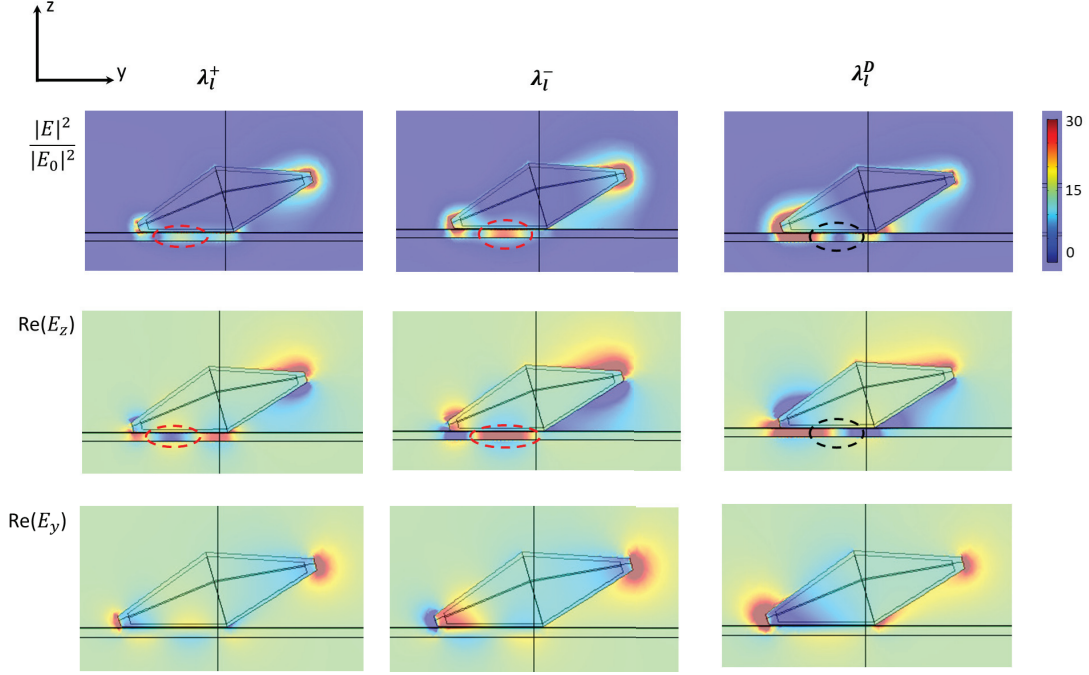


Figure 5.14: **Calculation of near-field distribution of the AuBP on the gold film.** Normalized total field distribution $|E|^2/|E_0|^2$ and the component field $Re(E_z(y, z))$ and $Re(E_y(y, z))$ in the Oyz plane. The red and black rings highlights the field distribution in the middle of the gap.

focusing on the three main resonances λ_l^+ , λ_l^- , and λ_l^D . Generally, we see that these modes exhibit strong field localization at the tip-ends and within the flat gap; the maximum near-field intensity enhancement is found around $|E|^2/|E_0|^2 = 30$. On the other hand, the field enhancement in the space of the opening-mouth gap is negligible as compared to that in the flat gap due to the less confinement. In addition, it appears in all three modes that the resonant electric fields in the flat gap are mostly polarized along the transverse direction to the metal's surface. As can be seen in the simulation in Figure 5.14, the transverse field component $Re(E_z)$ is the predominant field in the gap, while the longitudinal field component $Re(E_y)$ is negligible. This confirms the MIM gap plasmon characteristic of the modes of the system [38, 121].

The field distribution of the whole system is complex, but if we paid attention only to the gap region at this stage, we once again can see the hybrid modes λ_l^+ and λ_l^- possess similar near-field distributions that are concentric at the center of the flat gap (red rings). As opposed, the mode λ_l^D , which does not show the anti-crossing feature with the other

mode, is maximized at both ends and null in the middle (black rings).

Although the modes λ_l^+ and λ_l^- are at the mixed state, here we can still see the signatures of their origins. The formation of the field distribution inside the gap of the mode λ_l^+ can be interpreted as the finite MIM gap plasmon liked Fabry-Pérot resonance induced by the interaction between the flat metal surface at the bottom facet of the AuBP and the gold film. Due to the finite dimension of the MIM waveguide defined by the lateral facet of the AuBP, the transverse gap plasmon is bounced back and forth inside the gap due to the reflection at the gap terminal and displays stationary nodes [38, 111, 88, 121]. As shown in the field distribution of this mode, the electric field is localized in the core and largest at both ends, which resembles the character of the standing wave. On the other hand, the field inside the gap of the mode λ_l^- is formed by the interaction of the particle with its mirror image in the gold film, similar to the situation in a plasmonic nanoparticle dimer [103, 112, 107]. As shown by the charge distribution (Figure 5.12), the mode λ_l^- originates from the quadrupole, which is also concordant with Figure 5.13. Indeed, in this Figure we see that at $g=4\text{nm}$, the modes are not completely hybridized so that the quadrupolar mode λ_l^Q is still dominant in the mode λ_l^- .

5.5 The complexity of the AuBP nanopatch antenna

In the previous discussion, we presented the most remarkable features of the AuBP nanopatch. However, due to the geometry of the bipyramid, the structure is in fact really complicated in terms of the plasmonic effects that contribute to the formation of the modes and subsequent difficulties in the interpretation of the results.

A complex plasmon structure

Here, we see the structure in three aspects, respectively are:

- *An elongated plasmonic nanoparticle* that strongly supports the localized plasmon resonance along its longitudinal axis rather than the transverse one. In addition, the tip effect of the AuBP is also significant resulting in the strong field localization in the near-field around the tip ends.

- *A MIM waveguide with finite lateral dimension:* Tilting AuBP introduces a facet of the particle in contact with the surface. The dielectric space embedded between the particle's facet and the underlying gold film (i.e., a nanopatch) can now be seen as a MIM waveguide with a finite lateral dimension, which resembles a Fabry-Pérot cavity. As the result, the stationary wave of the transverse gap plasmon can be observed within the gap region.
- *A dimer induced by the mirror effect:* When the metallic nanoparticle is brought close to the gold film, the charge distribution on the particle induces image charges in the underlying conducting layer. This configuration can be thought of as a nanoparticle interacting with its mirror image that is equivalent to plasmonic nanoparticle dimers. As the result, the dipolar mode can be repelled to higher wavelengths and gives birth to new resonances of the higher-order modes in the lower region.

Because many effects involve the formation of the mode, it is not straightforward to identify the nature of the mode clearly. Usually, the nanopatch of more symmetric nanoparticles such as spheres and cubes [122, 110, 103, 53], where the modes of the structure can be clearly classified into two families: antenna mode and gap plasmon cavity mode, based on their most significant features, either strongly radiate or tightly confined field. However, in the case of the AuBP, both the gap plasmon, and especially the tip effect exhibit in all the modes, which are not predominantly by the other.

In terms of the hybridization of the modes λ_t^+ and λ_t^- , it is also perturbed by the effects mediated by the gold film. Roughly, for a perfect coupling system at the strongest interaction, the splitting of the hybrid modes possesses a mirror symmetry in terms of phase, spectral position, and intensity [123]. In addition, the spectral separation of the modes in the anti-crossing branches should be in the opposite direction, which is red-shifted for bonding mode and blue-shifted for anti-bonding one [123, 124]. However, the anti-crossing of the hybrid modes, as observed in Figure 5.13, presents an imbalance of intensities of the two resonances at the strongest hybridization $g = 3\text{-}4\text{nm}$. Moreover, the spectral evolutions of their fundamental modes are both pulled towards the red as the gap thickness decreases (green and red lines in Figure 5.13). Here, the very weak shift of the mode λ_t^Q is caused by the

cancelation of the red shift due to the mirror effect and the blue shift induced by the mode hybridization.

Geometry imposes the selection rule on the excitation

Because of the elongated shape and the tilting AuBP with one facet contacting with the surface, the illumination is necessary to be in the normal direction, as we have done above, in order to optimize the power introduced to the structure. This makes it difficult to interpret the formation of the gap mode. Usually, the gap plasmon mode of the more symmetric nanoparticle-on-mirror configuration (e.g., spheres or cubes) can be directly excited by the plane wave in the high-angle illumination that induces more electric field components polarized perpendicular to the metal surface [110, 125]. On the other hand, in the case of the AuBP nanopatch, the excitation of the gap plasmon mode is not directly from the plane wave illumination but rather from multiple processes. First involves the longitudinal localized plasmon of the AuBP is excited by the plane wave and then localized the field around its lower tip will be responsible for excitation of the gap mode. This can be seen in the near-field distribution in Figure 5.14, the near field around the lower tip that touches the surface is more distributed inside the gap as the nodes in the gap increase.

5.6 Conclusion

In conclusion, we have studied the optical response of the AuBP on the high-index substrate and on the gold film. We first highlighted the important role of the orientation of the particle on the surface in terms of increasing the interaction strength of the particle and the substrate. Bringing an inclined AuBP in proximity to the gold film yields a rich optical response, where the modes have hybrid behavior of the localized surface plasmon of elongated particle, in an isolated structure and a linked-dimer, and gap plasmon in the finite MIM waveguide. Each possesses distinctive features such as strong dipolar and multipolar far-field radiation or strong field confinement. In addition, these resonances are tunable by varying the geometrical parameter of the system, which makes the structure can be very beneficial for sensing, photochemistry, and optoelectronics. However, there are still remaining questions,

for instance: a mechanism of the high index dielectric substrate induced the higher order mode of the AuBP, a rigorous calculation of the reflectivity at the patch terminals, from this the role of the opening-mouth gap in terms of enhancing radiation conversion can be evaluated quantitatively.

Chapter 6

Optically launching of Surface Plasmon Polaritons by Bipyr amid Nanopatch Antennas

Surface plasmon polaritons (SPPs) offer great potential for various present-day photonic applications, thanks to their ability to concentrate light in space and time. SPPs can be excited optically by a diffraction-limited beam [85, 34] or electrically using inelastic tunneling as a light source [126, 127, 128]. By any means of generating SPPs, the nanopatch antennas based on a metal-insulator-metal (MIM) structure have been shown their comprehensive capability to mediate SPP emission efficiently. Due to the ability to squeeze and tailor the light at the nanoscale, the nanopatch antennas provide degrees of freedom in the design of the structure that would allow us to properly engineer the properties of SPP emission, including the emission spectrum, polarization, and emission efficiency [78].

In this Chapter, we employ the light scattering from the bipyr amid nanopatch antennas to excite SPPs propagating along a dielectric/gold interface. We firstly demonstrate the SPP emission launched by the antenna in the visible regime, which is possibly extended to the near-infrared wavelengths thanks to the rich optical-mode structure of the antennas. We also report the angular emission pattern of SPPs induced by the scattered light. Finally, we measure the SPP emission efficiency of the antenna and compare it with SiO₂ nanobeads. The physical mechanisms involved in generating SPPs also will be discussed.

Contents

6.1 SPP emission spectrum	134
6.2 Spatial and angular emission of SPPs	136
6.3 SPP emission efficiency	139
6.4 Role of nanopatch antenna in SPP emission	144
6.5 Conclusion	148

6.1 SPP emission spectrum

To fully profit from the rich optical response of bipyramid nanopatch antennas, we only pay attention to tip-touching-surface AuBPs (inclined AuBPs) deposited on 4nm-TiO₂/45nm-Au/glass substrate. We use the white lamp focused by 0.25-NA objective to excite the antenna in the air and measure the forward scattering on the glass side by the 1.49-NA objective in the dark-field configuration (see Chapter 3). Roughly, the collection consists of both the leakage in the substrate through the thin gold film of excited SPPs and the residual scattering, which does not excite SPPs. To accurately identify the SPP emission spectrum, it is necessary to disperse the scattered light spectrally and spatially. We first measure the scattering spectrum of an antenna, as shown in Figure 6.1a. As clarified in the previous chapter, the inclined AuBPs can produce a multiple-resonance spectrum ranging from 500 – 1200nm. Because of the higher noise for $\lambda > 1000\text{nm}$ arising from the low detection efficiency of the spectrometer, here we concentrate on the resonances in the visible regime.

For the spatial distribution, we record a Fourier-plane image corresponding to the visible spectrum of the single antenna, as shown in Figure 6.1b. The leakage of SPPs appears in

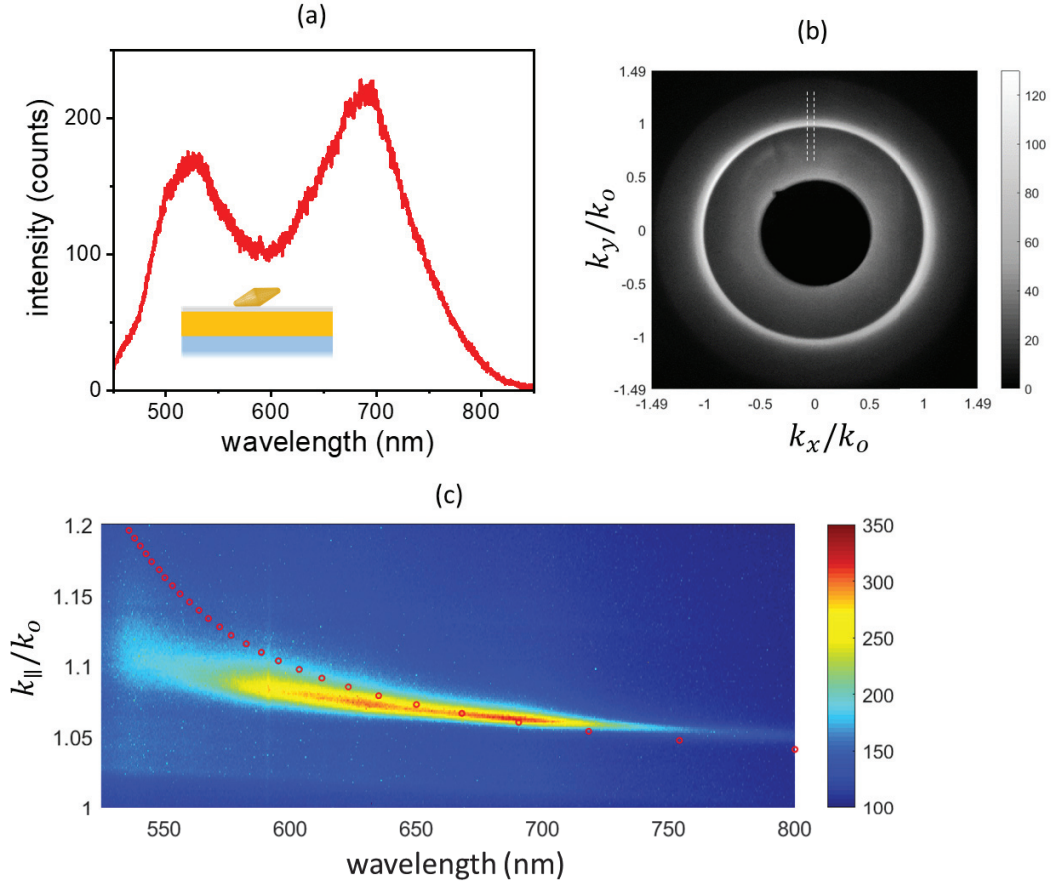


Figure 6.1: **SPP emission spectrum.** (a) Dark-field scattering spectrum of inclined AuBP on 4nm-TiO₂/45nm-Au/glass substrate (inset). Here, only the visible regime is displayed. (b) Fourier-plane image of scattering in (a). (c) Dispersion relation of selected direction on the Fourier-plane (white lines in (b)). Dotted line is the calculated dispersion relation. In-plane wavevector: $k_{||} = \sqrt{k_x^2 + k_y^2}$

the Fourier-plane as a bright ring of radius just above $k_{||} = k_0$ (where $k_0 = 2\pi/\lambda_0$ is the light wavevector in vacuum). The SPP ring is composed of surface plasmon propagating at different wavelengths associated with the scattered light of the antenna. To see the part of the scattering coupling to SPPs, we measure the dispersion relation between the in-plane wavevector ($k_{||}$) and the wavelengths by making an image of one selected direction in the Fourier-plane (white bars) on the vertical entrance slit of the spectrometer. Figure 6.1c displays the collected image, from which the SPP emission appears as a bright trace above the light line of the vacuum ($k_{||} = k_0$). The SPP dispersion closely follows the dispersion curve (dotted line) calculated for SPPs propagating on the similar multilayer substrate, except for

the regime below 600nm. Qualitatively, two main factors drive SPP emission here: resonant scattering of the antenna and the intrinsic loss owing to the absorption of gold. Below $\lambda = 600\text{nm}$, the influence of the interband transition of gold is dominant, resulting in the negligible appearance of the SPP emission. As far from this regime, the scattering resonance weakly suffers from this loss and generates SPPs as the bright trace on the dispersion image. Besides, the most intense region in the SPP dispersion is at around $\lambda = 700\text{nm}$, which is associated with the second resonance on the scattering spectrum, suggesting the SPP emission by this mode is driven mainly by the scattering resonance.

6.2 Spatial and angular emission of SPPs

We now present the spatial and angular emission of the surface plasmon excited by the scattered light from the antenna, using a SuperK supercontinuum laser for excitation. The supercontinuum laser can provide a beam-quality laser with a white-lamp spectra range of 400-980nm. Technically, the super-wide continuous spectrum is produced by sending intense light pulses through a nonlinear medium. A slit is used to select the wavelength, making a laser beam with the smallest spectra width of 10nm. For example, Figure 6.2 shows a real-space image in the dark field and its corresponding Fourier-plane images of an antenna excited by a $650\text{nm} \pm 5\text{nm}$ laser beam.

In the real-space image, we see an intensity maximum at the center enclosed by concentric interference rings propagating away from the antenna. These rings are interpreted as the interference of leakage radiation of SPPs propagating in opposite directions. In addition, there are other rings with longer periodicity resulting from the diffraction-limited image of residual scattering collected by the finite numerical aperture of the objective [129]. To access the SPPs propagation, we plot the intensity along with a cross-section through the center of the real-space image as a function of the distance to the antenna on the x-axis, as shown in Figure 6.2b. Note that we used a linear polarizer oriented along the x-axis (white arrow) to select surface plasmon propagation in this direction. An exponential decay profile is observed with a propagation length estimated to be $1.5 \pm 0.03\mu\text{m}$, which is shorter by $\sim 3\mu\text{m}$ than what we predicted theoretically for the SPPs launching on the similar thin TiO_2 film over

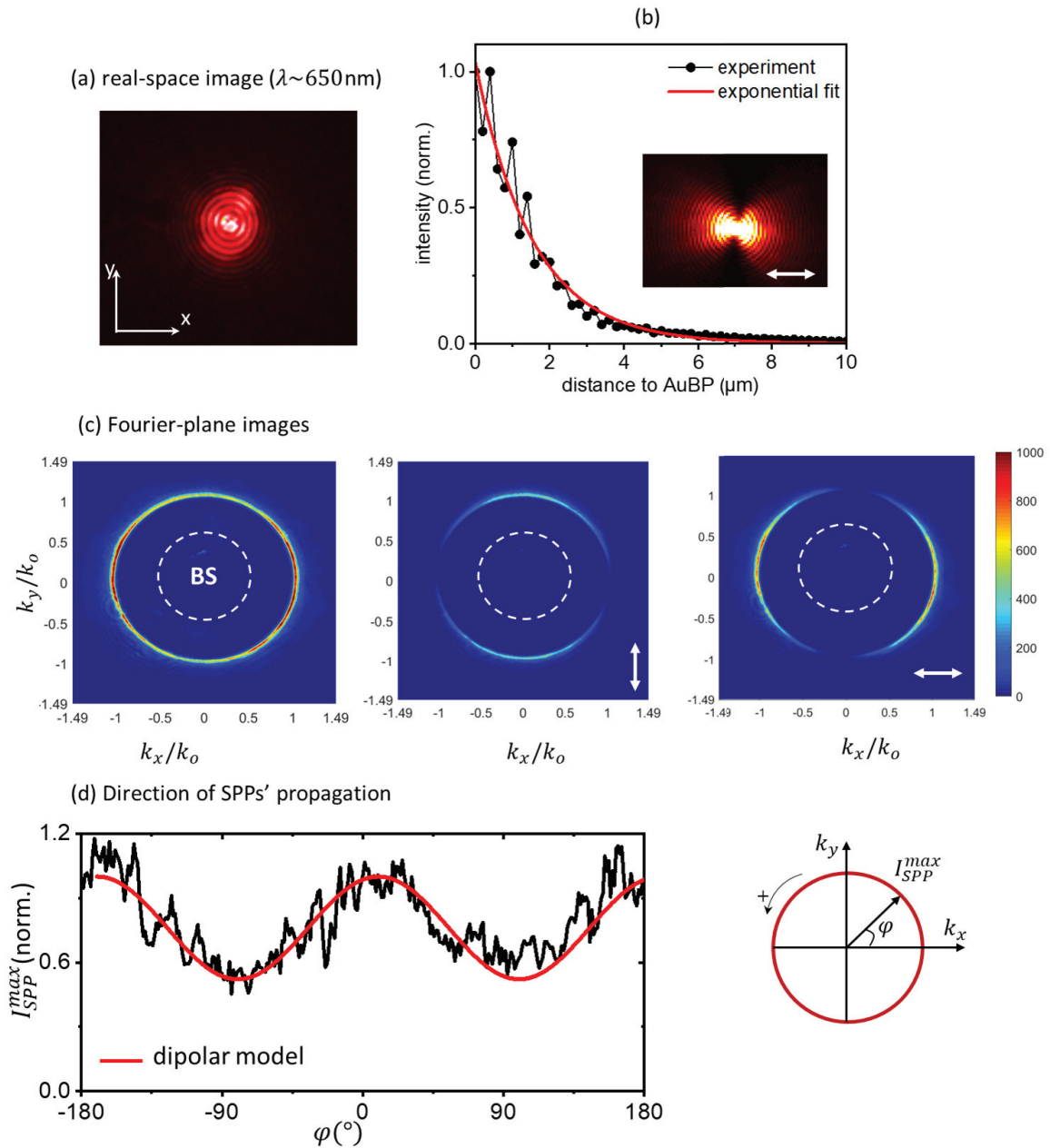


Figure 6.2: **Spatial and angular emission of SPPs.** (a) Real-space image of the antenna measured by the dark-field imaging. (b) Cross-section profile along the x-axis of polarized real-space image (inset). The black dots are the experimental data, the red line is exponential decay fit. (c) Fourier-plane images of (a), from left to right: unpolarize, linear polarize along y-axis, linear polarizer along x-axis. BS: Beam Stop. (d) Intensity of SPPs extracted from the image (c) (no polarize) as a function of the angle φ . The measured data is fitted to dipolar model (i.e., considering the AuBP as a dipole placed near the substrate.)

the gold film. We attribute this difference to the film's surface roughness, which is highly dependent on the deposition procedure [130]. In our experiment, the surface roughness is $\sim 30\%$ of the TiO_2 film thickness deposited by the ALD.

The angular radiation pattern of the leakage SPPs can be observed in the Fourier-plane image with the overwhelming excitation omitted by the beam stop (BS). As shown in Figure 6.2c, SPPs emerge as a circular pattern with a bright and narrow ring whose radius corresponds to the wavevector of $1.07k_0$, a signature of SPPs propagating along an air/4nm- TiO_2 /gold interface.

To analyze the spatial polarization distribution of the scattering, we place a linear polarizer along the x-axis and y-axis behind the objective's back focal plane. Figure 6.2c shows the Fourier-plane images for two orientations of the polarizer. We can see that the field along the polarizer orientation is transmitted, whereas the field along the orthogonal direction is filtered out. In other words, the photons in the ring are almost polarized radially with respect to the origin formed by the position of the antenna (p polarization), which shows the characteristic of the leakage radiation of SPPs.

In terms of the directionality, we can see a non-uniform intensity distribution in the circular ring of the Fourier-plane image. In Figure 6.2d we plot the maximum intensities of the SPPs I_{SPP}^{max} (extracted from the bright ring in Figure 6.2c) as a function of the polar coordinate φ corresponding to the direction of SPP's propagation. The AuBP is modelled as a linear dipole, which is placed near the substrate with its 3D orientations (Θ, Φ) as an adjustable parameter. We see that the measured $I_{SPP}^{max}(\varphi)$ follows very well the cosine square function of the dipolar simulation. The best fit is given at an out-of-plane orientation $\Theta \approx 70^\circ$, corresponding to the AuBP is tilted by around 20° on the surface (the dipolar axis is along the longitudinal axis of the AuBP). Interestingly, this orientation is in a good agreement with the values estimated from the geometrical dimensions of the AuBP $\sim 75 \pm 5^\circ$ (see Figure 4.7c), suggesting that the directivity of launching SPPs is mostly controlled by the dipolar character of the AuBP. Besides, we also observe that the SPPs mainly propagate in the direction along the longitudinal axis of the bipyramid (i.e., $I_{SPP}^{max}(\phi)$ peaks at $\Phi \sim 0; 180^\circ$). Thanks to the SuperK supercontinuum laser, we also can measure the angular emission of SPPs of other resonance; however, it is complicated to go into detail of interpretation.

6.3 SPP emission efficiency

An important figure of merit of a source for launching surface plasmon is the SPP emission efficiency, which depends on both the system that is used to excite SPPs (e.g., prism, grating, local scatters) and the collection efficiency of the experiment. In the case of the bipyramid nanopatch antenna, the structure plays a role in harvesting the power from the light source and delivering it to the surface plasmon. This involves multiple processes that will be discussed later. Here, we first present how we measure the SPP emission efficiency using leakage radiation microscopy.

Briefly, the excited SPPs and the transmission of the excitation can be extracted spatially in the Fourier-plane image of the leakage radiation microscope. This method has been employed in previous studies to characterize the SPP coupling efficiency of the local sub-wavelength scatterers. For instance, A. Baudrion et.al., [32] have used a single hole of variable size $\sim 100\text{-}500\text{nm}$ milled in a gold film to generate SPPs. The SPP emission efficiency is defined as a ratio of the total leakage power of the SPPs and the incident power of the laser, taking into account only the part that arrive on the hole area. However, some ambiguities, e.g., the transmission of the SPPs through the gold film or the total power that the hole received from the excitation beam, have remained. Similar work has been studied by T. Ebbesen et.al., [31], in which the SPPs are generated by a sub-wavelength slit. The work was more rigorous in the quantification of the leakage SPPs on the Fourier plane by introducing the leakage transmission factor for the SPPs. In our work, we combine the advantages of both presented work to measure SPP emission efficiency of the AuBP nanopatch antenna.

Following the previous works [32, 131, 84], we also define the antenna efficiency to generate SPPs as the ratio of the excited SPP power P_{SPP} to the incident power P_0 :

$$E_{SPP} = \frac{P_{SPP}}{P_0} \quad (6.1)$$

Here, $P_0 = P_{beam} \frac{A_{BP}}{A_{beam}}$ is the partial power of the laser beam P_{beam} , taking into account only the part that impinges onto the surface over the geometrical cross-section area of the bipyramid (see Figure 6.3). Here, the size of laser beam A_{beam} is measured directly in the

image for each wavelength (e.g. $\lambda = 650\text{nm}$, diameter $\sim 3.3\mu\text{m}$) that is also approximately to the Airy function with diameter of $d \approx 1.22 \frac{\lambda}{NA}$. The $A_{BP} = L/2 \cdot W/2$ is the geometrical cross-section area of the AuBP, with $L = 70\text{nm}$ and $W = 25\text{ nm}$ are average sizes of AuBPs obtained for TEM measurement (see Chapter 4).

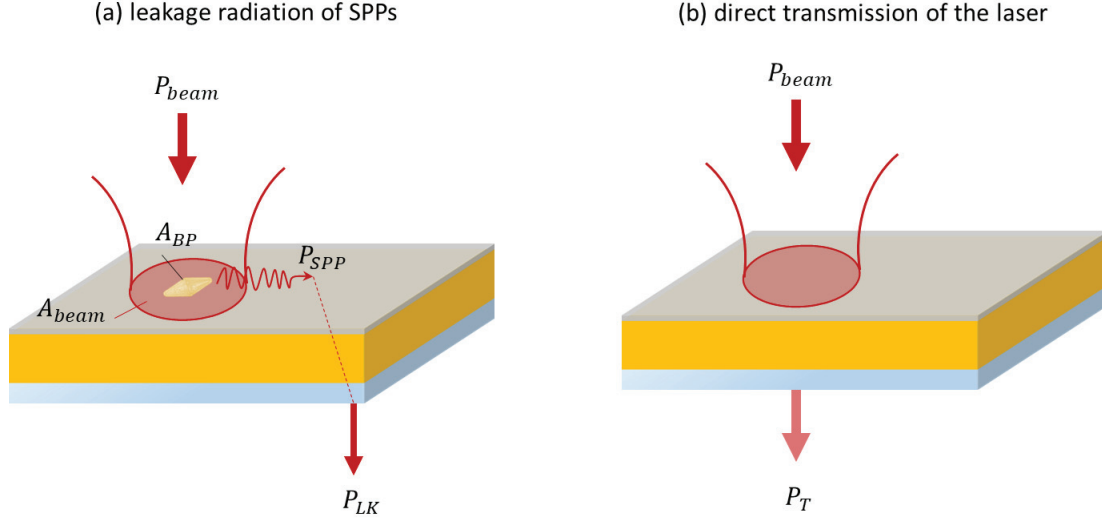


Figure 6.3: **Measuring the SPP emission efficiency by leakage radiation microscope.** Schematic illustration of a focused laser beam excite the nanopatch to generate the SPPs. The red circle beam represents the beam spot ($A_{beam} \sim \lambda^2$), A_{BP} is the geometrical area of the AuBP. The experiment allows to measure (a) the leakage power of the SPPs P_{SPP} and (b) the transmitted power of laser P_T .

Powers measured from leakage radiation experiments

Since the gold slab has a finite thickness, the surface plasmon propagating away from the antenna in the air is a leaky wave that radiates energy into the higher-index side of the glass substrate. Suppose we neglect the scattering loss into the air due to the surface roughness. In that case, the total excited SPP power P_{SPP} can be deduced from the leakage surface plasmon P_{LK} (i.e., the quantity that we can measure) taking into account the leakage transmission factor τ_{LK} [31, 35] and is given by:

$$P_{SPP} = \frac{P_{LK}}{\tau_{LK}} \quad (6.2)$$

The leakage transmission of the surface plasmon through a finite gold layer is calculated as $\tau_{LK} = e^{-2|k_z|d_{Au}}$ with $d_{Au} = 45\text{nm}$ as the thickness of the gold slab and $k_z =$

$\lambda(\text{nm})$	ε_{Au}	T	k_{spp}/k_0	$\Delta k_{spp}/k_0$	τ_{LK}	$\frac{A_{beam}}{A_{AuBP}}$
600	-9.38+1.39i	14%	1.1	0.10	6.5%	100
650	-12.90+1.04i	9.7%	1.072	0.03	5.5%	120
700	16.54+1.00i	7.0%	1.056	0.02	4.9%	140
750	-20.36+1.17i	5.3%	1.044	0.02	4.5%	160

Table 6.1: **Parameters need for calculation of SPP coupling efficiency.** Values of transmission are calculated the multilayer substrate of air ($\varepsilon_{air}=1$)/4nm-TiO₂ ($\varepsilon_{TiO_2}=2.4$)/45nm-Au (ε_{Au})/glass ($\varepsilon_{glass}=1.5$).

$\sqrt{k_{spp}^2 - \varepsilon_{Au}(2\pi/\lambda_0)^2}$ is the wavevector of the SPPs in the normal direction to the surface. The SPP wavevector k_{spp} for each wavelength is deduced from the angular distribution of SPP emission in the Fourier-plane image (see below). The dielectric function ε_{Au} of gold is taken from the data obtained by Johnson and Christy [11].

Similarly, the incident power P_0 is measured from the transmitted power P_T of the laser through the substrate, illuminating at the position without the presence of antenna as $P_0 = \frac{P_T}{T} \cdot \frac{A_{beam}}{A_{BP}}$. Here, T is the direct transmission of the laser at the normal incident through the multilayer substrate (see Figure 6.3b), which is calculated from the matrix transfer formalism [48].

Finally, we can display the SPP coupling efficiency of the antenna as a function of the parameters that we can measured from the experiment as

$$E_{SPP} = \frac{P_{LK}}{P_T} \cdot \frac{T}{\tau_{LK}} \cdot \frac{A_{beam}}{A_{BP}} \quad (6.3)$$

In which, the leakage and transmitted powers P_{LK} and P_T are extracted from Fourier-plane images, while the other parameters are measured at four different wavelengths and displayed in Table 6.1.

The parameters needed for calculation of SPP coupling efficiency at four different wavelengths are displayed in Table 6.1.

Measuring P_{LK} and P_T

To remove the artifact of the attenuation due to the optical elements, both transmitted powers are measured by integrating all the corresponding signals from the images recorded at the same laser input power related to the surface area of the particle (P_0). When the antenna

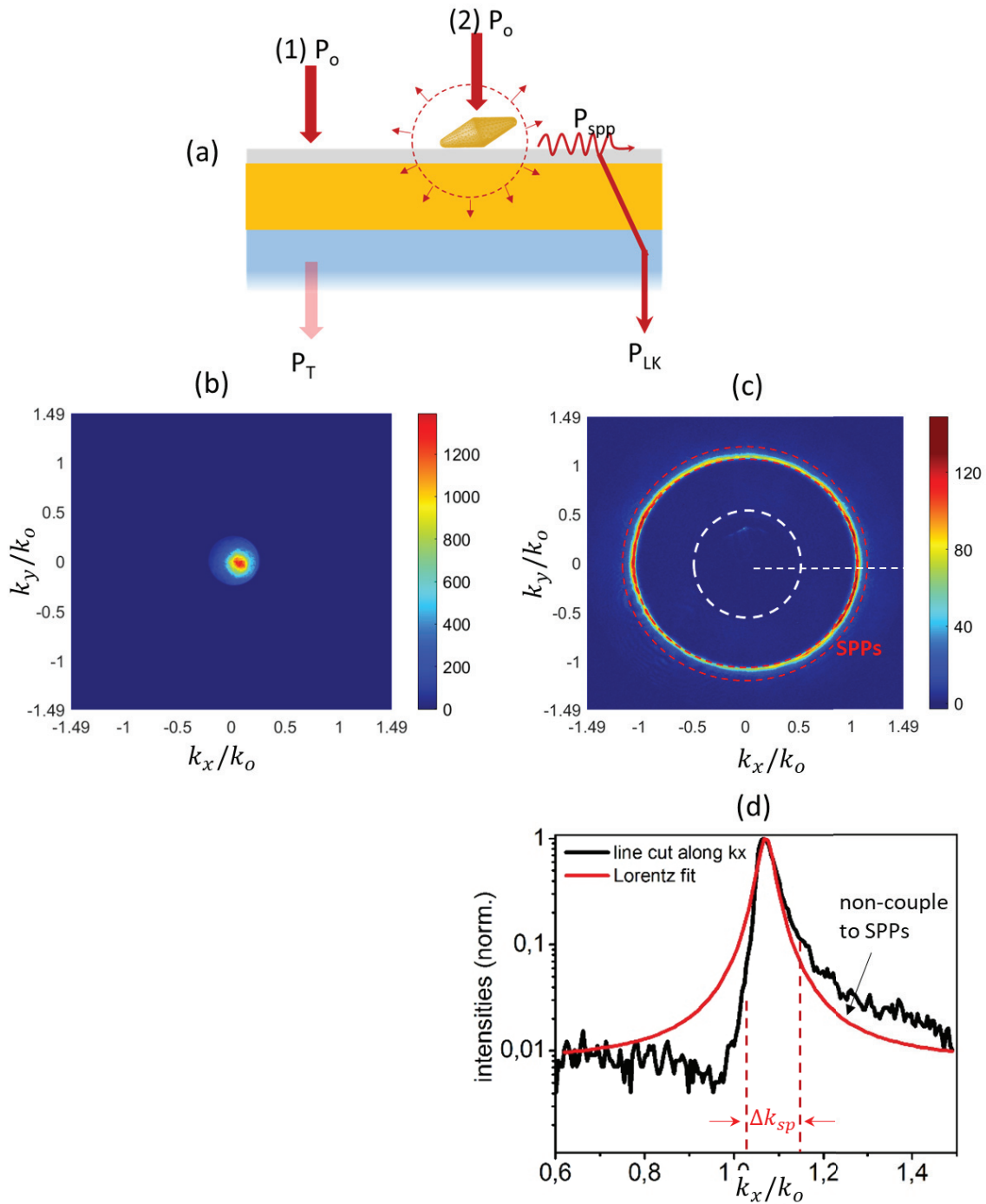


Figure 6.4: **Measuring SPP emission efficiency.**(a) Schematic of the measurement. P_0 : in-input power of laser over the geometrical cross-section area of bipyramid. P_{SPP} : power excited SPPs. P_T : transmitted power of P_0 through substrate in the absence of the antenna. P_{LK} : leakage power of SPPs. (b) Fourier-plane image of laser's transmission (1). (c) Fourier-plane image of antenna's scattering (2). White ring is the region of the beam stop. Red rings enclosed the region of SPPs. (d) Intensity profile of a line cut on the scattering pattern (white line) as a function of k_x/k_0 . Black line is the experimental curve, red line is the Lorentzian fit.

is excited, the leakage SPPs can be extracted from the dark-field scattering pattern in the Fourier-plane image (see **(1)** in Figure 6.4a). On the other hand, the laser's transmission is also measured on the Fourier plane. Still, the excitation is in the absence of the bipyramids, taking only the transmission due to the multilayer substrate (see **(2)** in Figure 6.4a). In Figure 6.4b, the laser transmission is observed as a disk with a radius $\sim 0.25 k_0$ associated with the numerical aperture of the excitation objective. The power P_T can be determined by integrating all the signals from this Fourier-plane image.

Figure 6.4c shows the scattering pattern of the antenna in the Fourier-plane image, which can be interpreted as a superposition of the leakage SPPs on the scattered light background of the antenna (i.e., residual scattering that does not excite SPPs). To quantify the leakage SPPs, we integrate the Fourier plane between $(k_{spp} - \Delta k_{spp})$ and $(k_{spp} + \Delta k_{spp})$, which is enclosed by red rings in Figure 6.4c. The SPP wavevector k_{spp} and the width Δk_{spp} are given from the Lorentzian fit of an intensity profile of a radial cross-cut along the k_x -axis as shown in Figure 6.4d. The contribution of surface plasmon is defined approximately by an area under the Lorentzian curve, whereas the area that does not fit within the Lorentzian function is attributed to the residual scattering. Here, the leakage SPPs account for around 60% of the total detected emission (all the signals in Figure 6.4c) and 10% of the transmission of the laser ($P_{spp}/P_T = 10\%$). Taking into account the transmission factors (T and τ_{LK}) at $\lambda = 650\text{nm}$, we obtain an SPP coupling efficiency $E_{SPP} = 20$. We repeat the measurement of the SPP coupling efficiency at three other wavelengths (600nm, 700nm, and 750nm) displayed in Figure 6.5 (focusing on the second resonance at around 700nm).

In Figure 6.5, we correlate the measured SPP emission efficiency to the scattering spectrum, focusing on the second resonance at around 700nm. We see that the efficiency is also resonantly enhanced following the plasmon resonance of the considered mode. The efficiency at center resonance wavelength (700nm) is larger by ~ 4 times as compared to those at off-resonances. However, the measured values of E_{SPP} here all far more exceeds unity, implying that more light than is incident upon the geometrical cross-section of the bipyramid is converted into SPPs. This will be discussed in more detail in the following section.

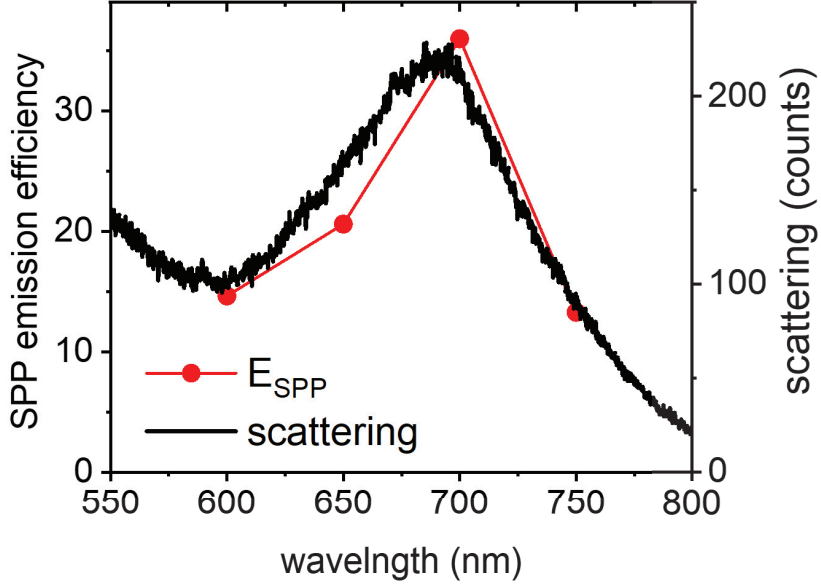


Figure 6.5: **The SPP emission efficiency of the AuBP nanopatch measured.** The efficiency is measured at four wavelengths and correlated to the scattering spectrum.

6.4 Role of nanopatch antenna in SPP emission

An optical antenna, as the name implied its analogy to the microwave and radio wave antennas, is an optical element that converts localized energy into propagating radiation, and vice versa. Discussing the SPP generation, the nanopatch antenna plays both roles as a receiver (i.e., a resonator that harvests the light from the free space and confines in its body) and a transducer (i.e., a strong scatterer) [1]. Based on this concept, we define the SPP emission efficiency of the nanopatch antenna as

$$E_{SPP} = \frac{P_{SPP}}{P_0} = \eta_{ext} \cdot \beta_{SPP} \quad (6.4)$$

which is composed of the extinction efficiency (η_{ext}), which defines the total power of the excitation that is delivered by the antenna, and the SPP conversion efficiency (β_{SPP}) that determines the proportion of the receiving power indeed excites SPPs. Figure 6.6 illustrates these two steps and details will be discussed in the following.

Total power delivered by the antenna

As the total power that the antenna carried away from the excitation light is either

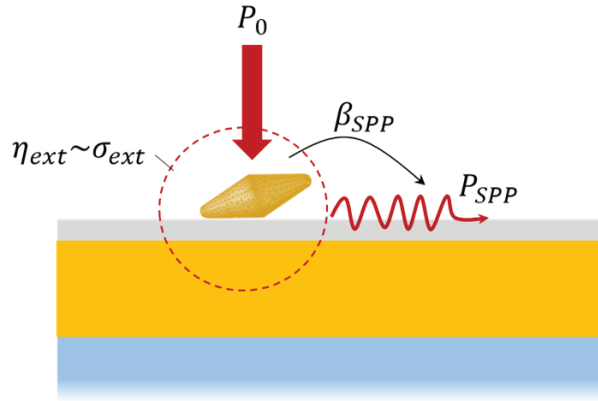


Figure 6.6: **The SPP generation by the AuBP nanopatch antenna.** The total power that antenna received from the excitation is defined by the extinction efficiency η_{ext} , which is later converted into SPPs, given by the conversion efficiency β_{SPP} .

scattered or absorbed and dissipated, we attribute the “lost” power to the extinction cross-section. We thus define the extinction efficiency as the fraction of the power that is received in the cases of with (P_{total}) and without antenna (P_0):

$$\eta_{SPP} = \frac{P_{total}}{P_0} = \frac{\sigma_{ext}}{A_{BP}} \quad (6.5)$$

where σ_{ext} is the extinction cross-section of the antenna and A_{BP} is the geometrical cross-section area of the bipyramid. We have known that at the resonance condition of the plasmonic structure, the σ_{ext} is resonantly enhanced, and thus the total power that the antenna receives P_{total} can be far more exceed the power incident the AuBP area P_0 . This explains why the measured SPP emission efficiency in Figure 6.5 can be larger than 1. The over-unity efficiency was also predicted for SPPs launching by scattering from a rectangular metallic hole etched in a metal substrate [131]. The author showed that an SPPs generation efficiency of 5 can be achieved at an optimal hole depth.

To support the above statements, we seek a comparison to SPPs launched by a dielectric nanobead of SiO_2 (diameter $\sim 120\text{nm}$, $\epsilon_{\text{SiO}_2} = 2.25$). In a homogeneous medium, the elastic scattering is fully responsible for the optical response of the “lossless” SiO_2 bead to the visible illumination [55]. For the particle near the gold film, it is affected by the field components reflected from the surface resulting in an additional absorption cross-section in the extinction cross-section. When the nanobead is illuminated, its near-field scattering can excite SPPs

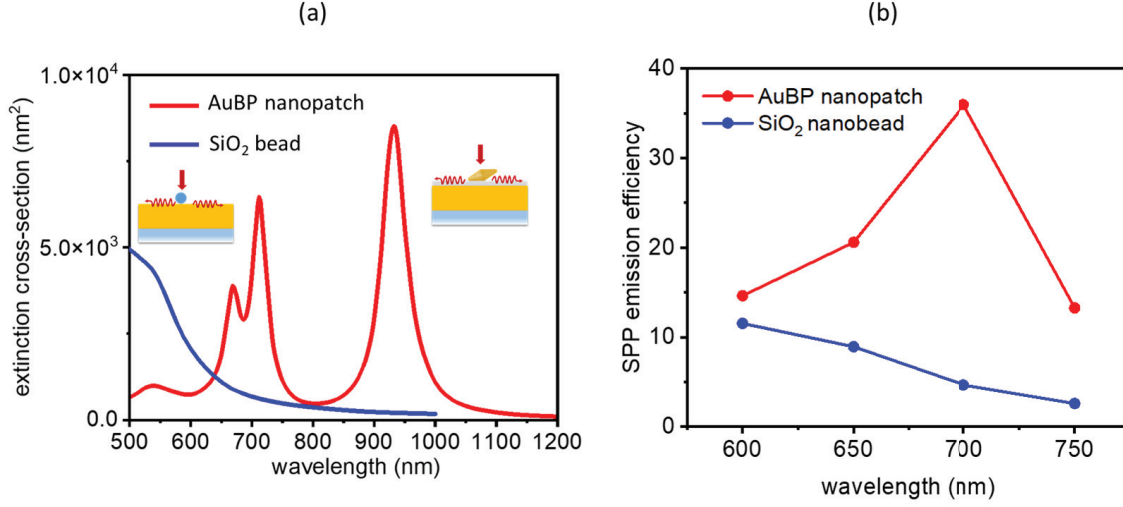


Figure 6.7: **Enhancing SPP emission efficiency due to extinction efficiency.** (a) Extinction cross-sections are calculated for a SiO₂ nanobead on 45nm-gold/glass substrate as compared to the AuBP nanopatch. (b) Associated SPP emission efficiency is measured at the same experimental conditions.

on the gold film.

Figure 6.7 shows the calculation of the extinction cross-section of the SiO₂ bead deposited on 45nm-gold film/glass substrate in response to the plane wave excitation. The presence of the gold film near the bead yields to the rising of the extinction cross-section below 600nm, which is mainly contributed by the absorption cross-section (not shown here for clarity). We can see that at the resonance wavelengths above 600nm, the extinction cross-section of the nanopatch is significantly larger than that of the SiO₂ bead by around 1 order of magnitude. This means that at the resonance, the total power delivered by the nanopatch is ~ 10 times larger than the power harvested by the nanobead (Figure 6.7a). Taking into account the geometrical cross-sectional areas, we can deduce the fraction of the extinction efficiency of the two structures is $\eta_{ext}^{BP}/\eta_{ext}^{SiO_2} \approx 60$, indicating the important role of plasmon modes supported by the antenna in the SPP emission in term of harvesting light and also SPP generation.

Subsequently, we measure the SPP emission efficiency of the bead, as shown in Figure b, keeping the same experimental conditions as for the nanopatch. We can see that all the measured efficiency of the patch is larger than those measured for the bead, which is the most significant at the resonance $\lambda = 700nm$: $E_{SPP}^{BP}/E_{SPP}^{SiO_2} \approx 7$. As mentioned above, to arrive at

the final value of the SPP emission efficiency, both extinction efficiency η_{ext} and conversion efficiency β_{SPP} are necessarily quantified. Unfortunately, it still requires further work for us to determine the conversion efficiency of the system (details below). However, by connecting both figures we can see the important contribution of the nanopatch antenna as a resonator in converting light into SPP emission.

Conversion of the total power delivered by the antenna into SPPs

The next step is to ensure that a significant part of the total power received by the antenna indeed excites SPPs, which can be defined by the SPP conversion efficiency as

$$\beta_{SPP} = \frac{P_{SPP}}{P_{total}} \quad (6.6)$$

Roughly, this conversion efficiency closely depends on the nature of the optical modes that are excited, including the modal local density of state (LDOS) and the modal absorption. The total power P_{total} of the nanopatch can be funneled into the optical modes (e.g., $\lambda_l^{(1,2,Q)}$) or dissipated in the losses of the metal, Chapter 5). Therefore, the mode of large LDOS has more advantages in receiving the total power. As shown at the beginning of Chapter 5, the gap plasmon mode can provide a significant LDOS tight field confinement inside MIM nanogap, which largely overcomes the quenching even for very thin gap thickness when the structure is excited by an emitter (see Figure 5.1). However, the strong confinement of the gap plasmon comes with the price of low modal conversion to the free-space radiation owing its large modal absorption. The resonant hotspots in the gap are typically reflected back inside the gap or emitted into high angles because of their large in-plane $k_{||}$.

It is worth insisting that this modal absorption is different from the losses of the metal mentioned above, which are higher-order modes outside the spectra ranges of interest or heating the metal. If the structure is excited by an emitter, the modal absorption can be thought of as a nonradiative channel, while the losses are the quenching of the emitter. However, unlike quenching which is intrinsically determined by the proximity to the metal, the absorption depends on the nanoantenna design [122, 110, 105]. For example, a low absorption is favored by the antenna with curve edges (e.g., sphere or tie-bow) that implement

small reflectivity at the facet edges [104, 1]. Another strategy is to optimize the geometrical parameters of the nanopatch antenna in order to couple the tightly confined gap plasmon mode to the antenna mode of strong radiating [105, 132]. The resulting hybrid modes will possess both the large LDOS and the high modal SPP conversion efficiency.

In the case of the AuBP nanopatch antenna, the structure can be a promising class of nanogap antenna with the facet edge's reflectivity gradually decreasing in the opening mouth. From this, an efficient SPP emission can be achieved through balancing between the large LDOS and the low modal absorption. However, in order to address the SPP conversion efficiency β_{SPP} of the nanopatch and also of the modes, further works, using for example a rigorous modal formalism [110, 119], are required to separate the contribution of each mode. In turn, it is useful to show a simple and intuitive picture, as presented here, to understand the role of the nanopatch antenna in the SPP emission process. Although without accessing to the conversion efficiency β_{SPP} of the nanopatch, based on the resonant evolution of the SPP emission efficiency E_{SPP} (Figure 6.5), which strictly follows the scattering resonance, we can anticipate that the β_{SPP} might be independent of the wavelengths in this resonance.

6.5 Conclusion

In summary, we have shown that the SPP emission in the AuBP nanopatch antenna can be generated in a wide range of spectra with achievable directionality. Here, the nanopatch antenna plays both roles as a receiver that harvests the light in the far field into its plasmonic modes, and a scatter that can excite SPPs. We have demonstrated that the SPP emission efficiency can be resonantly enhanced by the nanopatch by around 1 order of magnitude as compared to the dielectric local scatters. This enhancement is contributed by both extinction efficiency η_{ext} and the conversion efficiency β_{SPP} . Here, the extinction efficiency is estimated through the calculation of the extinction cross-section. However, the SPP conversion efficiency β_{SPP} of the total system and the specific mode still remains unknown. In the perspective, an emitter or a dipole can be placed inside the structure as a probe to extract β_{SPP} efficiency.

Conclusion and Perspectives

In this Thesis, we have investigated analytically the dipole coupling in the weak regime to different planar plasmonic structures, from a single interface, and a three-layer device to multilayer structures. By using dipole as a probe, figures of merit of the plasmonic structure have been identified, including spatial distribution and profile of the modes, propagation length of the delocalized surface plasmon, and coupling efficiency to the modes. This provided part of the necessary groundwork for understanding the plasmonic properties in more complicated structures. In addition, the configuration studied here may be interesting for multimode integrated devices such as single photons on a chip, quantum entanglement, or optical communications.

The main task of this Thesis was to investigate the optical properties of the gold bipyramid nanopatch antennas in a nanoparticle-on-mirror configuration. We have demonstrated that the orientation of the AuBPs on the substrate plays a crucial role in yielding the interactions of the particle and the underneath gold film. Only when the AuBP is tilted with one facet contacting the surface, the nanopatch can be formed, from which a rich optical mode structure is produced. We identified experimentally and theoretically the set of plasmonic modes supported by the structure, which possesses both radiating characteristics and strong field confinement. Especially, we have shown there is a hybridization between the modes that share similar symmetry of the charges (and field) distribution inside the finite MIM gap. We assign this as the interaction between the quadrupolar mode and the gap plasmon liked Fabry-Pérot cavity mode. Moreover, the complexity of the structure induced by the geometry of the AuBP, as compared to the other nanopatch antennas of more symmetric geometry, has been discussed thoroughly. In the last chapter, we have employed the nanopatch as a source for launching surface plasmon on the gold film surrounding the structure, which has proven

to control the properties of SPPs emission, including the emission spectrum, polarization, and emission efficiency. The understanding of the properties of such a complex structure that has been explored in this Thesis set the important groundwork for coupling the AuBP nanopatch antenna to the other systems (i.e., emitters or other metallic nanoparticles) in further work.

Perspectives

Stabilization of the AuBP by silanization

In this Thesis, the substrate's surface is cleaned basically by a nitrogen pump and the AuBPs are deposited randomly on the surface without surface treatment or control. In the following work, we want to improve the quality of the surface of the substrate and make the particles more stable on the substrate. This can be done by silanization -a technique for immobilizing nanoparticles on a substrate, which has been used previously to graft the AuBPs on the glass substrate [68]. In addition to attaching the objects to the surface, the silanes also stabilize the morphology of anisotropic gold nanoparticles. Fortunately, the silanization process tends to make the AuBPs oriented in a good direction (i.e., one facet of the particle contacts the underlying surface). An overview of the silanization protocol can be seen in Figure C1.

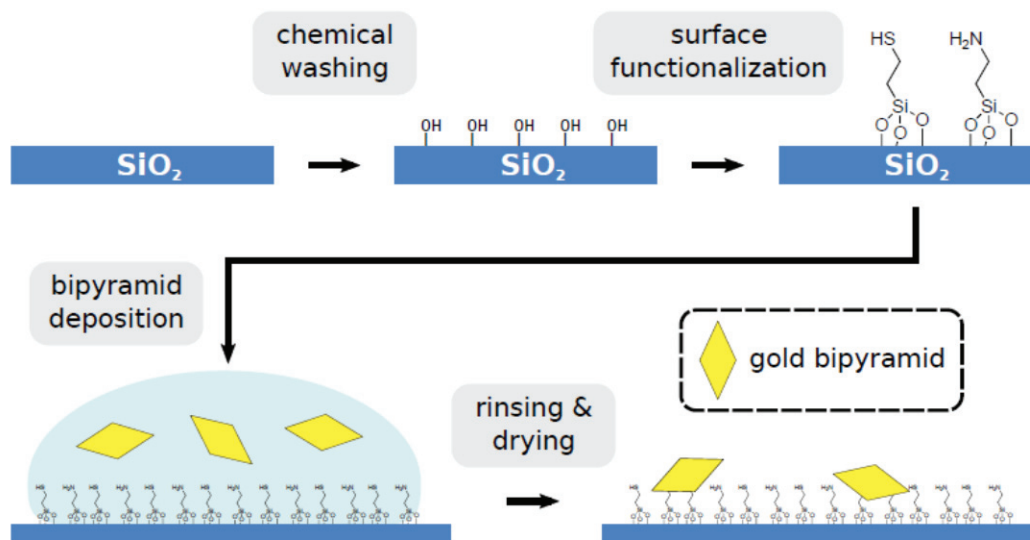


Figure C1: Schematic illustrates the silanization protocol to graft bipyramid on the substrate. Source [5]

Correlation between the orientation and the spectral shift

As shown in Chapters 3 and 4, the orientation of the AuBP on the substrate, especially high index substrate, can induce the spectral shift of the longitudinal dipolar localized surface plasmon resonances. In further work, we want to make a correlation between these two parameters and compare the results to the orientations measured by the polarization analysis. This can be particularly useful for biosensing applications.

Coupling to emitters

Owning the hybrid plasmon properties, both radiative nature and tightly field confinement, coupling to emitters is the most potential application of the nanopatch antennas. In our work, we expect to couple the AuBP nanopatch to fluorescent molecules or quantum dots. As we can see in the near field distribution of the plasmon modes, we have many positions to place a single emitter in close proximity to the structure, where the choice depends on the properties that we want to enhance. For example, a large spontaneous decay rate enhancement can be achieved when the emitter is buried in the gap or placed near the lower tip. In addition, the directionality and the emission spectra of the emitters are also possibly controlled by coupling to the plasmonic modes of the structure.

Energy transfer over the surface

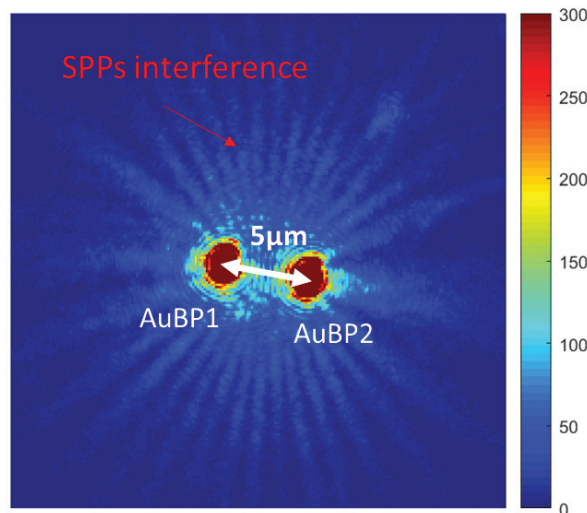


Figure C2: Interference of SPPs generated by two AuBPs deposited in the proximity on the 4nm-TiO₂/gold film.

Another exciting perspective is to employ the ability of SPP generation of the AuBP

nanopatch to induce the interaction between the particles on the surface. Figure C2 shows an image of the interference of SPPs produced by two bipyramid particles on the nanopatch substrate. Here, although the two bipyramid nanoparticle are separated at a micrometer distance, they still can “talk” to each other thanks to the coherent and long propagation of the SPPs.

Bibliography

- [1] Lukas Novotny and Niek Van Hulst. Antennas for light. *Nature photonics*, 5(2):83–90, 2011.
- [2] Thang B Hoang, Gleb M Akselrod, Christos Argyropoulos, Jiani Huang, David R Smith, and Maiken H Mikkelsen. Ultrafast spontaneous emission source using plasmonic nanoantennas. *Nature communications*, 6(1):1–7, 2015.
- [3] K Lance Kelly, Eduardo Coronado, Lin Lin Zhao, and George C Schatz. The optical properties of metal nanoparticles: the influence of size, shape, and dielectric environment, 2003.
- [4] P Nordlander and F Le. Plasmonic structure and electromagnetic field enhancements in the metallic nanoparticle-film system. *Applied Physics B*, 84(1):35–41, 2006.
- [5] Jan-Michael Rye. *Spatial Modulation Spectroscopy Of Single Nano-Objects In A Liquid Environment For Biosensing Applications*. PhD thesis, Université de Lyon, 2017.
- [6] Neil W Ashcroft and N David Mermin. *Solid state physics*. Cengage Learning, 2022.
- [7] Stefan A Maier et al. *Plasmonics: fundamentals and applications*, volume 1. Springer, 2007.
- [8] Mark Fox. Optical properties of solids, 2002.
- [9] Klaus D Sattler. *Handbook of nanophysics: nanoelectronics and nanophotonics*. CRC press, 2010.
- [10] Paul McEuen and C Kittel. Introduction to solid state physics. 2005.
- [11] P Johnson. B and christy rw 1972. *Phys. Rev. B*, 19:4370.
- [12] Pablo Albella, M Ameen Poyli, Mikolaj K Schmidt, Stefan A Maier, Fernando Moreno, Juan José Sáenz, and Javier Aizpurua. Low-loss electric and magnetic field-enhanced spectroscopy with subwavelength silicon dimers. *The Journal of Physical Chemistry C*, 117(26):13573–13584, 2013.
- [13] Qianfan Xu, Vilson R. Almeida, Roberto R. Panepucci, and Michal Lipson. Experimental demonstration of guiding and confining light in nanometer-size low-refractive-index material. *Opt. Lett.*, 29(14):1626–1628, Jul 2004.

-
- [14] Jacob T. Robinson, Christina Manolatou, Long Chen, and Michal Lipson. Ultrasmall mode volumes in dielectric optical microcavities. *Phys. Rev. Lett.*, 95:143901, Sep 2005.
- [15] Jacob B Khurgin. How to deal with the loss in plasmonics and metamaterials. *Nature nanotechnology*, 10(1):2–6, 2015.
- [16] JMea Gerard, D Barrier, JY Marzin, R Kuszelewicz, L Manin, E Costard, V Thierry-Mieg, and T Rivera. Quantum boxes as active probes for photonic microstructures: The pillar microcavity case. *Applied Physics Letters*, 69(4):449–451, 1996.
- [17] Matthew Pelton, Charles Santori, Jelena Vucković, Bingyang Zhang, Glenn S Solomon, Jocelyn Plant, and Yoshihisa Yamamoto. Efficient source of single photons: a single quantum dot in a micropost microcavity. *Physical review letters*, 89(23):233602, 2002.
- [18] DK Armani, TJ Kippenberg, SM Spillane, and KJ Vahala. Ultra-high-q toroid microcavity on a chip. *Nature*, 421(6926):925–928, 2003.
- [19] DW Vernooy, Vladimir S Ilchenko, H Mabuchi, EW Streed, and HJ Kimble. High-q measurements of fused-silica microspheres in the near infrared. *Optics letters*, 23(4):247–249, 1998.
- [20] Misha Boroditsky, Rutger Vrijen, Roberto Coccioli, Raj Bhat, and Eli Yablonovitch. Spontaneous emission extraction and purcell enhancement from thin-film 2-d photonic crystals. *Journal of Lightwave technology*, 17(11):2096, 1999.
- [21] TH Taminiau, FD Stefani, Franciscus B Segerink, and NF Van Hulst. Optical antennas direct single-molecule emission. *Nature photonics*, 2(4):234–237, 2008.
- [22] Rohit Chikkaraddy, Bart De Nijs, Felix Benz, Steven J Barrow, Oren A Scherman, Edina Rosta, Angela Demetriadou, Peter Fox, Ortwin Hess, and Jeremy J Baumberg. Single-molecule strong coupling at room temperature in plasmonic nanocavities. *Nature*, 535(7610):127–130, 2016.
- [23] Jeanne Heintz, Nemanja Markesevic, Elise Y Gayet, Nicolas Bonod, and Sébastien Bidault. Few-molecule strong coupling with dimers of plasmonic nanoparticles assembled on dna. *ACS nano*, 15(9):14732–14743, 2021.
- [24] Kerry J Vahala. Optical microcavities. *nature*, 424(6950):839–846, 2003.
- [25] Julian Gargiulo, Rodrigo Berté, Yi Li, Stefan A Maier, and Emiliano Cortés. From optical to chemical hot spots in plasmonics. *Accounts of chemical research*, 52(9):2525–2535, 2019.
- [26] Sabrina Simoncelli, Yi Li, Emiliano Cortés, and Stefan A Maier. Nanoscale control of molecular self-assembly induced by plasmonic hot-electron dynamics. *ACS nano*, 12(3):2184–2192, 2018.
- [27] Robert Williams Wood. Xlii. on a remarkable case of uneven distribution of light in a diffraction grating spectrum. *The London, Edinburgh, and Dublin Philosophical Magazine and Journal of Science*, 4(21):396–402, 1902.

- [28] Erwin Kretschmann and Heinz Raether. Radiative decay of non radiative surface plasmons excited by light. *Zeitschrift für Naturforschung A*, 23(12):2135–2136, 1968.
- [29] Andreas Otto. Excitation of nonradiative surface plasma waves in silver by the method of frustrated total reflection. *Zeitschrift für Physik A Hadrons and nuclei*, 216(4):398–410, 1968.
- [30] Eloise Devaux, Thomas W Ebbesen, Jean-Claude Weeber, and Alain Dereux. Launching and decoupling surface plasmons via micro-gratings. *Applied physics letters*, 83(24):4936–4938, 2003.
- [31] Jean-Yves Laluet, Aurélien Drezet, C Genet, and TW Ebbesen. Generation of surface plasmons at single subwavelength slits: from slit to ridge plasmon. *New Journal of Physics*, 10(10):105014, 2008.
- [32] Anne-Laure Baudrion, Fernando de Leon-Perez, Oussama Mahboub, Andreas Hohenau, Harald Ditlbacher, Francisco J Garcia-Vidal, José Dintinger, Thomas W Ebbesen, Luis Martin-Moreno, and Joachim R Krenn. Coupling efficiency of light to surface plasmon polariton for single subwavelength holes in a gold film. *Optics express*, 16(5):3420–3429, 2008.
- [33] William L Barnes, Alain Dereux, and Thomas W Ebbesen. Surface plasmon subwavelength optics. *nature*, 424(6950):824–830, 2003.
- [34] Dmitri K Gramotnev and Sergey I Bozhevolnyi. Plasmonics beyond the diffraction limit. *Nature photonics*, 4(2):83–91, 2010.
- [35] Stefan A Maier, Mark L Brongersma, Pieter G Kik, Sheffer Meltzer, Ari AG Requicha, and Harry A Atwater. Plasmonics—a route to nanoscale optical devices. *Advanced materials*, 13(19):1501–1505, 2001.
- [36] Pierre Berini. Figures of merit for surface plasmon waveguides. *Optics Express*, 14(26):13030–13042, 2006.
- [37] Kevin Chevrier, Jean-Michel Benoit, Clementine Symonds, Julien Papparone, Julien Laverdant, and Joel Bellessa. Organic exciton in strong coupling with long-range surface plasmons and waveguided modes. *Acs Photonics*, 5(1):80–84, 2018.
- [38] Hideki T Miyazaki and Yoichi Kurokawa. Squeezing visible light waves into a 3-nm-thick and 55-nm-long plasmon cavity. *Physical review letters*, 96(9):097401, 2006.
- [39] Lukas Novotny and Bert Hecht. *Principles of nano-optics*. Cambridge university press, 2012.
- [40] Wolfram Hergert and Thomas Wriedt. Mie theory 1908-2008. *Present developments and Interdisciplinary aspects of light scattering, Universität Bremen, Bremen-presentation*, 2008.
- [41] Craig F Bohren and Donald R Huffman. *Absorption and scattering of light by small particles*. John Wiley & Sons, 2008.

-
- [42] Anonymous. Proceedings of the american physical society. *Phys. Rev.*, 69:674–674, Jun 1946.
- [43] Eugen Merzbacher. *Quantum mechanics*. Jones & Bartlett Publishers, 1961.
- [44] Jun John Sakurai and Eugene D Commins. Modern quantum mechanics, revised edition, 1995.
- [45] Walter Lukosz and RE Kunz. Light emission by magnetic and electric dipoles close to a plane interface. i. total radiated power. *JOSA*, 67(12):1607–1615, 1977.
- [46] W Lukosz and RE Kunz. Light emission by magnetic and electric dipoles close to a plane dielectric interface. ii. radiation patterns of perpendicular oriented dipoles. *JOSA*, 67(12):1615–1619, 1977.
- [47] W Lukosz. Light emission by magnetic and electric dipoles close to a plane dielectric interface. iii. radiation patterns of dipoles with arbitrary orientation. *JOSA*, 69(11):1495–1503, 1979.
- [48] Kevin Chevrier. *Cohérence dans les systèmes métal/organique en couplage fort: états étendus et métasurfaces*. PhD thesis, Université de Lyon, 2019.
- [49] Cam Nhung Vu and Julien Laverdant. Coupling a single dipole to a long-range surface plasmon device. *Optics Letters*, 45(18):5193–5196, 2020.
- [50] Yoichi Kurokawa and Hideki T Miyazaki. Metal-insulator-metal plasmon nanocavities: Analysis of optical properties. *Physical Review B*, 75(3):035411, 2007.
- [51] Jianji Yang, Christophe Sauvan, Anthony Jouanin, Stéphane Collin, J-L Pelouard, and Philippe Lalanne. Ultrasmall metal-insulator-metal nanoresonators: impact of slow-wave effects on the quality factor. *Optics Express*, 20(15):16880–16891, 2012.
- [52] Sergey I Bozhevolnyi and Thomas Søndergaard. General properties of slow-plasmon resonant nanostructures: nano-antennas and resonators. *Optics express*, 15(17):10869–10877, 2007.
- [53] Daniel O Sigle, Jan Mertens, Lars O Herrmann, Richard W Bowman, Sandrine Ithurria, Benoit Dubertret, Yumeng Shi, Hui Ying Yang, Christos Tserkezis, Javier Aizpurua, et al. Monitoring morphological changes in 2d monolayer semiconductors using atom-thick plasmonic nanocavities. *ACS nano*, 9(1):825–830, 2015.
- [54] Jialong Peng, Hyeon-Ho Jeong, Michael Smith, Rohit Chikkaraddy, Qianqi Lin, Hsin-Ling Liang, Michael FL De Volder, Silvia Vignolini, Sohini Kar-Narayan, and Jeremy J Baumberg. Fullyprinted flexible plasmonic metafilms with directional color dynamics. *Advanced Science*, 8(2):2002419, 2021.
- [55] Eduardo JC Dias and F Javier García de Abajo. Complete coupling of focused light to surface polaritons. *Optica*, 8(4):520–531, 2021.

- [56] Rohit Chikkaraddy and Jeremy J Baumberg. Accessing plasmonic hotspots using nanoparticle-on-foil constructs. *ACS photonics*, 8(9):2811–2817, 2021.
- [57] Hui Fan, Robert Charbonneau, and Pierre Berini. Long-range surface plasmon triple-output mach-zehnder interferometers. *Optics express*, 22(4):4006–4020, 2014.
- [58] CA Marocico and Jasper Knoester. Effect of surface-plasmon polaritons on spontaneous emission and intermolecular energy-transfer rates in multilayered geometries. *Physical review A*, 84(5):053824, 2011.
- [59] C Huang, Alexandre Bouhelier, G Colas des Francs, Aurélien Bruyant, A Guenot, Eric Finot, J-C Weeber, and Alain Dereux. Gain, detuning, and radiation patterns of nanoparticle optical antennas. *Physical Review B*, 78(15):155407, 2008.
- [60] Pierre Berini. Long-range surface plasmon polaritons. *Advances in optics and photonics*, 1(3):484–588, 2009.
- [61] Aurélien Drezet, Andreas Hohenau, Daniel Koller, Andrey Stepanov, H Ditlbacher, Bernhard Steinberger, Franz Rembert Aussenegg, Alfred Leitner, and Joachim Rudolf Krenn. Leakage radiation microscopy of surface plasmon polaritons. *Materials science and engineering: B*, 149(3):220–229, 2008.
- [62] Rémi Carminati, Alexandre Cazé, Da Cao, F Peragut, V Krachmalnicoff, Romain Pierrat, and Yannick De Wilde. Electromagnetic density of states in complex plasmonic systems. *Surface Science Reports*, 70(1):1–41, 2015.
- [63] Francisco J Garcia-Vidal, Cristiano Ciuti, and Thomas W Ebbesen. Manipulating matter by strong coupling to vacuum fields. *Science*, 373(6551):eabd0336, 2021.
- [64] Päivi Törmä and William L Barnes. Strong coupling between surface plasmon polaritons and emitters: a review. *Reports on Progress in Physics*, 78(1):013901, 2014.
- [65] Cam Nhung Vu, Corentin Prados, and Julien Laverdant. Surface plasmon hybridized dressed states. *Optics Letters*, 47(6):1435–1438, 2022.
- [66] Gleb M Akselrod, Christos Argyropoulos, Thang B Hoang, Cristian Ciraci, Chao Fang, Jiani Huang, David R Smith, and Maiken H Mikkelsen. Probing the mechanisms of large purcell enhancement in plasmonic nanoantennas. *Nature Photonics*, 8(11):835–840, 2014.
- [67] Pascal Anger, Palash Bharadwaj, and Lukas Novotny. Enhancement and quenching of single-molecule fluorescence. *Physical review letters*, 96(11):113002, 2006.
- [68] Jan-Michael Rye, Christophe Bonnet, Frédéric Lerouge, Michel Pellarin, Jean Lermé, Stéphane Parola, and Emmanuel Cottancin. Single gold bipyramids on a silanized substrate as robust plasmonic sensors for liquid environments. *Nanoscale*, 10(34):16094–16101, 2018.

-
- [69] T Klar, M Perner, S Grosse, G Von Plessen, W Spirkl, and J Feldmann. Surface-plasmon resonances in single metallic nanoparticles. *Physical Review Letters*, 80(19):4249, 1998.
- [70] J Prikulis, H Xu, L Gunnarsson, M Käll, and Håkan Olin. Phase-sensitive near-field imaging of metal nanoparticles. *Journal of applied physics*, 92(10):6211–6214, 2002.
- [71] Hitoshi Kuwata, Hiroharu Tamaru, Kunio Esumi, and Kenjiro Miyano. Resonant light scattering from metal nanoparticles: Practical analysis beyond rayleigh approximation. *Applied physics letters*, 83(22):4625–4627, 2003.
- [72] Nhung C Vu, Zakarya Ouzit, Clotilde Lethiec, Agnès Maitre, Laurent Coolen, Frédéric Lerouge, and Julien Laverdant. Single gold bipyramid nanoparticle orientation measured by plasmon-resonant scattering polarimetry. *The Journal of Physical Chemistry Letters*, 12(2):752–757, 2021.
- [73] C Sönnichsen, S Geier, NE Hecker, G Von Plessen, J Feldmann, H Ditlbacher, B Lamprecht, JR Krenn, FR Aussenegg, V ZH Chan, et al. Spectroscopy of single metallic nanoparticles using total internal reflection microscopy. *Applied Physics Letters*, 77(19):2949–2951, 2000.
- [74] David Boyer, Philippe Tamarat, Abdelhamid Maali, Brahim Lounis, and Michel Orrit. Photothermal imaging of nanometer-sized metal particles among scatterers. *Science*, 297(5584):1160–1163, 2002.
- [75] Wei-Shun Chang, Ji Won Ha, Liane S Slaughter, and Stephan Link. Plasmonic nanorod absorbers as orientation sensors. *Proceedings of the National Academy of Sciences*, 107(7):2781–2786, 2010.
- [76] Fu Feng, Loan Thu NGuyen, Michel Nasilowski, Brice Nadal, Benoît Dubertret, Agnès Maître, and Laurent Coolen. Probing the fluorescence dipoles of single cubic cdse/cds nanoplatelets with vertical or horizontal orientations. *ACS photonics*, 5(5):1994–1999, 2018.
- [77] M Andreas Lieb, James M Zavislan, and Lukas Novotny. Single-molecule orientations determined by direct emission pattern imaging. *JOSA B*, 21(6):1210–1215, 2004.
- [78] Alberto González Curto. *Optical antennas control light emission*. PhD thesis, Universitat Politècnica de Catalunya, 2014.
- [79] Clotilde Lethiec, Julien Laverdant, Henri Vallon, Clémentine Javaux, Benoît Dubertret, Jean-Marc Frigerio, Catherine Schwob, Laurent Coolen, and Agnès Maître. Measurement of three-dimensional dipole orientation of a single fluorescent nanoemitter by emission polarization analysis. *Physical Review X*, 4(2):021037, 2014.
- [80] Clotilde Lethiec. *Emission polarisée de nanoémetteurs: excitation de plasmons sur une surface métallique*. PhD thesis, Université Pierre et Marie Curie-Paris VI, 2014.

- [81] B Hecht, H Bielefeldt, L Novotny, Y Inouye, and DW Pohl. Local excitation, scattering, and interference of surface plasmons. *Physical review letters*, 77(9):1889, 1996.
- [82] Julien Laverdant, Samuel Aberra Guebrou, François Bessueille, Clementine Symonds, and Joel Bellessa. Leakage interferences applied to surface plasmon analysis. *JOSA A*, 31(5):1067–1073, 2014.
- [83] Céline Vion, Piernicola Spinicelli, Laurent Coolen, Catherine Schwob, Jean-Marc Frigerio, Jean-Pierre Hermier, and Agnès Maître. Controlled modification of single colloidal cdse/zns nanocrystal fluorescence through interactions with a gold surface. *Optics express*, 18(7):7440–7455, 2010.
- [84] Philippe Lalanne, Jean-Paul Hugonin, HT Liu, and Bing Wang. A microscopic view of the electromagnetic properties of sub- λ metallic surfaces. *Surface Science Reports*, 64(10):453–469, 2009.
- [85] Alexandre Bouhelier and GP Wiederrecht. Surface plasmon rainbow jets. *Optics letters*, 30(8):884–886, 2005.
- [86] T Shegai, S Chen, VD Miljković, G Zengin, P Johansson, and M Käll. A bimetallic nanoantenna for directional colour routing nat, 2011.
- [87] Timur Shegai, Peter Johansson, Christoph Langhammer, and Mikael Kall. Directional scattering and hydrogen sensing by bimetallic pd–au nanoantennas. *Nano letters*, 12(5):2464–2469, 2012.
- [88] Ruben Esteban, TV Teperik, and Jean-Jacques Greffet. Optical patch antennas for single photon emission using surface plasmon resonances. *Physical review letters*, 104(2):026802, 2010.
- [89] Julien RG Navarro, Delphine Manchon, Frédéric Lerouge, Nicholas P Blanchard, Sophie Marotte, Yann Leverrier, Jacqueline Marvel, Frédéric Chaput, Guillaume Micouin, Ana-Maria Gabudean, et al. Synthesis of pegylated gold nanostars and bipyramids for intracellular uptake. *Nanotechnology*, 23(46):465602, 2012.
- [90] Julien RG Navarro, Delphine Manchon, Frédéric Lerouge, Emmanuel Cottancin, Jean Lermé, Christophe Bonnet, Frédéric Chaput, Alexis Mosset, Michel Pellarin, and Stephane Parola. Synthesis, electron tomography and single-particle optical response of twisted gold nano-bipyramids. *Nanotechnology*, 23(14):145707, 2012.
- [91] Huanjun Chen, Lei Shao, Tian Ming, Kat Choi Woo, Yat Cho Man, Jianfang Wang, and Hai-Qing Lin. Observation of the fano resonance in gold nanorods supported on high-dielectric-constant substrates. *Acs Nano*, 5(8):6754–6763, 2011.
- [92] Shunping Zhang, Kui Bao, Naomi J Halas, Hongxing Xu, and Peter Nordlander. Substrate-induced fano resonances of a plasmonic nanocube: a route to increased-sensitivity localized surface plasmon resonance sensors revealed. *Nano letters*, 11(4):1657–1663, 2011.

-
- [93] Xavier Brokmann, Laurent Coolen, Jean-Pierre Hermier, and Maxime Dahan. Emission properties of single cdse/zns quantum dots close to a dielectric interface. *Chemical Physics*, 318(1-2):91–98, 2005.
- [94] Masashi Ohmachi, Yasunori Komori, Atsuko H Iwane, Fumihiko Fujii, Takashi Jin, and Toshio Yanagida. Fluorescence microscopy for simultaneous observation of 3d orientation and movement and its application to quantum rod-tagged myosin v. *Proceedings of the National Academy of Sciences*, 109(14):5294–5298, 2012.
- [95] Lehui Xiao, YanXia Qiao, Yan He, and Edward S Yeung. Three dimensional orientational imaging of nanoparticles with darkfield microscopy. *Analytical chemistry*, 82(12):5268–5274, 2010.
- [96] So Young Lee, Yeji Han, Jong Wook Hong, and Ji Won Ha. Single gold bipyramids with sharp tips as sensitive single particle orientation sensors in biological studies. *Nanoscale*, 9(33):12060–12067, 2017.
- [97] Ji Won Ha, Kyle Marchuk, and Ning Fang. Focused orientation and position imaging (fopi) of single anisotropic plasmonic nanoparticles by total internal reflection scattering microscopy. *Nano letters*, 12(8):4282–4288, 2012.
- [98] Ji Won Ha, Wei Sun, Anthony S Stender, and Ning Fang. Dual-wavelength detection of rotational diffusion of single anisotropic nanocarriers on live cell membranes. *The Journal of Physical Chemistry C*, 116(4):2766–2771, 2012.
- [99] Clotilde Lethiec, Ferruccio Pisanello, Luigi Carbone, Alberto Bramati, Laurent Coolen, and Agnès Maitre. Polarimetry-based analysis of dipolar transitions of single colloidal cdse/cds dot-in-rods. *New Journal of Physics*, 16(9):093014, 2014.
- [100] Jiawen Liu, Agnès Maître, and Laurent Coolen. Tailoring experimental configurations to probe transition dipoles of fluorescent nanoemitters by polarimetry or fourier imaging with enhanced sensitivity. *The Journal of Physical Chemistry A*, 125(34):7572–7580, 2021.
- [101] Ferruccio Pisanello, Luigi Martiradonna, Godefroy Leménager, Piernicola Spinicelli, Angela Fiore, Liberato Manna, Jean-Pierre Hermier, Roberto Cingolani, Elisabeth Giacobino, Massimo De Vittorio, et al. Room temperature-dipolelike single photon source with a colloidal dot-in-rod. *Applied Physics Letters*, 96(3):033101, 2010.
- [102] Etienne Pertreux, Anna Lombardi, Ileana Florea, Miguel Spuch-Calvar, Sergio Gómez-Graña, Dris Ihiawakrim, Charles Hirlimann, Ovidiu Ersen, Jérôme Majimel, Mona Tréguer-Delapierre, et al. Surface plasmon resonance of an individual nano-object on an absorbing substrate: Quantitative effects of distance and 3d orientation. *Advanced Optical Materials*, 4(4):567–577, 2016.
- [103] C Tserkezis, Ruben Esteban, Daniel O Sigle, Jan Mertens, Lars O Herrmann, Jeremy J Baumberg, and Javier Aizpurua. Hybridization of plasmonic antenna and cavity modes: Extreme optics of nanoparticle-on-mirror nanogaps. *Physical Review A*, 92(5):053811, 2015.

- [104] Rémi Faggiani, Jianji Yang, and Philippe Lalanne. Quenching, plasmonic, and radiative decays in nanogap emitting devices. *ACS photonics*, 2(12):1739–1744, 2015.
- [105] Cheng Zhang, Jean-Paul Hugonin, Jean-Jacques Greffet, and Christophe Sauvan. Surface plasmon polaritons emission with nanopatch antennas: enhancement by means of mode hybridization. *ACS photonics*, 6(11):2788–2796, 2019.
- [106] Sebastien Bidault, Alexis Devilez, Vincent Maillard, Laurent Lermusiaux, Jean-Michel Guigner, Nicolas Bonod, and Jerome Wenger. Picosecond lifetimes with high quantum yields from single-photon-emitting colloidal nanostructures at room temperature. *ACS nano*, 10(4):4806–4815, 2016.
- [107] Salem Marhaba, Guillaume Bachelier, Christophe Bonnet, Michel Broyer, Emmanuel Cottancin, Nadia Grillet, Jean Lermé, Jean-Louis Vialle, and Michel Pellarin. Surface plasmon resonance of single gold nanodimers near the conductive contact limit. *The Journal of Physical Chemistry C*, 113(11):4349–4356, 2009.
- [108] Nadia Grillet, Delphine Manchon, Franck Bertorelle, Christophe Bonnet, Michel Broyer, Emmanuel Cottancin, Jean Lermé, Matthias Hillenkamp, and Michel Pellarin. Plasmon coupling in silver nanocube dimers: resonance splitting induced by edge rounding. *Acs Nano*, 5(12):9450–9462, 2011.
- [109] Jun Hee Yoon, Florian Selbach, Ludmilla Schumacher, Jesil Jose, and Sebastian Schlucker. Surface plasmon coupling in dimers of gold nanoparticles: Experiment and theory for ideal (spherical) and nonideal (faceted) building blocks. *Acs Photonics*, 6(3):642–648, 2019.
- [110] Rohit Chikkaraddy, Xuezhi Zheng, Felix Benz, Laura J Brooks, Bart De Nijs, Cloudy Carnegie, Marie-Elena Kleemann, Jan Mertens, Richard W Bowman, Guy AE Vandenbosch, et al. How ultranarrow gap symmetries control plasmonic nanocavity modes: from cubes to spheres in the nanoparticle-on-mirror. *Acs Photonics*, 4(3):469–475, 2017.
- [111] Ahsan Noor, Anoop R Damodaran, In-Ho Lee, Stefan A Maier, Sang-Hyun Oh, and Cristian Ciraci. Mode-matching enhancement of second-harmonic generation with plasmonic nanopatch antennas. *ACS photonics*, 7(12):3333–3340, 2020.
- [112] Jan Mertens, Anna L Eiden, Daniel O Sigle, Fumin Huang, Antonio Lombardo, Zhipei Sun, Ravi S Sundaram, Alan Colli, Christos Tserkezis, Javier Aizpurua, et al. Controlling subnanometer gaps in plasmonic dimers using graphene. *Nano letters*, 13(11):5033–5038, 2013.
- [113] Huigao Duan, Antonio I Fernández-Domínguez, Michel Bosman, Stefan A Maier, and Joel KW Yang. Nanoplasmonics: classical down to the nanometer scale. *Nano letters*, 12(3):1683–1689, 2012.
- [114] Johannes Kern, Swen Großmann, Nadezda V Tarakina, Tim Hackel, Monika Emmerling, Martin Kamp, Jer-Shing Huang, Paolo Biagioni, Jord C Prangma, and Bert Hecht. Atomic-scale confinement of resonant optical fields. *Nano letters*, 12(11):5504–5509, 2012.

-
- [115] Philippe Lalanne, Christophe Sauvan, and Jean Paul Hugonin. Photon confinement in photonic crystal nanocavities. *Laser & Photonics Reviews*, 2(6):514–526, 2008.
- [116] Feng Wang and Y Ron Shen. General properties of local plasmons in metal nanostructures. *Physical review letters*, 97(20):206806, 2006.
- [117] Markus Parzefall and Lukas Novotny. Light at the end of the tunnel. *ACS Photonics*, 5(11):4195–4202, 2018.
- [118] Prashant K Jain, Wenyu Huang, and Mostafa A El-Sayed. On the universal scaling behavior of the distance decay of plasmon coupling in metal nanoparticle pairs: a plasmon ruler equation. *Nano Letters*, 7(7):2080–2088, 2007.
- [119] Eoin Elliott, Kalun Bedingfield, Junyang Huang, Shu Hu, Bart de Nijs, Angela Demetriadou, and Jeremy J Baumberg. Fingerprinting the hidden facets of plasmonic nanocavities. *ACS photonics*, 2022.
- [120] Jack J Mock, Ryan T Hill, Aloyse Degiron, Stefan Zauscher, Ashutosh Chilkoti, and David R Smith. Distance-dependent plasmon resonant coupling between a gold nanoparticle and gold film. *Nano letters*, 8(8):2245–2252, 2008.
- [121] Fred Minkowski, Feng Wang, Ayan Chakrabarty, and Qi-Huo Wei. Resonant cavity modes of circular plasmonic patch nanoantennas. *Applied Physics Letters*, 104(2):021111, 2014.
- [122] Jeremy J Baumberg, Javier Aizpurua, Maiken H Mikkelsen, and David R Smith. Extreme nanophotonics from ultrathin metallic gaps. *Nature materials*, 18(7):668–678, 2019.
- [123] Anthony Mark Fox, Mark Fox, et al. *Quantum optics: an introduction*, volume 15. Oxford university press, 2006.
- [124] Matthew Pelton, S David Storm, and Haixu Leng. Strong coupling of emitters to single plasmonic nanoparticles: exciton-induced transparency and rabi splitting. *Nanoscale*, 11(31):14540–14552, 2019.
- [125] J Britt Lassiter, Felicia McGuire, Jack J Mock, Cristian Ciraci, Ryan T Hill, Benjamin J Wiley, Ashutosh Chilkoti, and David R Smith. Plasmonic waveguide modes of film-coupled metallic nanocubes. *Nano letters*, 13(12):5866–5872, 2013.
- [126] Cheng Zhang, Jean-Paul Hugonin, Anne-Lise Coutrot, Christophe Sauvan, François Marquier, and Jean-Jacques Greffet. Antenna surface plasmon emission by inelastic tunneling. *Nature communications*, 10(1):1–7, 2019.
- [127] Pengyu Fan, Carlo Colombo, Kevin CY Huang, Peter Krogstrup, Jesper Nygard, Anna Fontcuberta i Morral, and Mark L Brongersma. An electrically-driven gas nanowire surface plasmon source. *Nano letters*, 12(9):4943–4947, 2012.
- [128] Palash Bharadwaj, Alexandre Bouhelier, and Lukas Novotny. Electrical excitation of surface plasmons. *Physical review letters*, 106(22):226802, 2011.

- [129] A Hohenau, JR Krenn, Aurélien Drezet, O Mollet, S Huant, C Genet, B Stein, and TW Ebbesen. Surface plasmon leakage radiation microscopy at the diffraction limit. *Optics express*, 19(25):25749–25762, 2011.
- [130] Kevin M McPeak, Sriharsha V Jayanti, Stephan JP Kress, Stefan Meyer, Stelio Iotti, Aurelio Rossinelli, and David J Norris. Plasmonic films can easily be better: rules and recipes. *ACS photonics*, 2(3):326–333, 2015.
- [131] Jianji Yang, Jean-Paul Hugonin, and Philippe Lalanne. Near-to-far field transformations for radiative and guided waves. *ACS photonics*, 3(3):395–402, 2016.
- [132] Cheng Zhang, Jean-Paul Hugonin, Anne-Lise Coutrot, Benjamin Vest, and Jean-Jacques Greffet. Electrical generation of visible surface plasmon polaritons by a nanopillars antenna array. *APL Photonics*, 6(5):056102, 2021.